Evidence for non-collinear magnetic structure at low temperature in M-type hexaferrite

Ohoud Nasser Alsaqer

Doctor of Philosophy

University of York

Physics

June 2022

Abstract

The field of magnetoelectric (ME) multiferroics is driven by the promise of controlling magnetism using applied electric fields, offering the possibility of a new generation of ultra-low power devices. Among the few room temperature single-phase ME multiferroics reported, M-type hexaferrite shows potential for device applications as they exhibit a low field ME effect at room temperature. The observed magnetoelectric properties in Co-Ti doped strontium M-type hexaferrrite are associated with the presence of the non-collinear magnetic structure that induces an electric polarisation through the inverse Dzyaloshinskii-Moriya interaction. Many studies reported the presence of the non-collinear magnetic structure with different elements and substitution rates. Hence, the non-collinear magnetic structure is the key to understanding the magnteoelectric properties in M-type doped hexaferrrites.

The work presented in this thesis had two main objectives. The first was to investigate the role of variation (Co-Ti) substitution of $SrCo_xTi_xFe_{12-x}O_{19}$ polycrystalline hexaferrite, where x=0, 0.7, 1.1, 1.5 and 2, on magnetic properties and their temperature dependence. The second was to characterise the structural and magnetic properties of $SrCo_2Ti_2Fe_8O_{19}$ single crystal, where the substitution induced magnetic anisotropy changes from uniaxial to planar anisotropy. In addition, to investigate the role of the strain of $SrCo_2Ti_2Fe_8O_{19}$ epitaxial thin films on magnetic properties.

A spontaneous transition from a collinear ferrimagnetic structure to a non-collinear magnetic structure has been detected in temperature dependent magnetisation measurements. This transition temperature, T_p is sensitive to the substitution rate as well as the measuring field. XMCD analysis reveals that the spin orientation of the magnetic ions (Fe, Co) at specific site symmetries vary with the thickness of the thin film.

Dedication

I dedicate this thesis to my family and all people I love

Declaration

I hereby declare that this thesis is a presentation of original work and I am the sole author, and to the best of my knowledge this work has not previously been presented for any other degree or qualification. All sources are acknowledged as references. The experimental and simulation work outlined in this thesis was carried out by the author, except where explicitly stated, under the supervision of Dr S. Cavill.

Signed

Ohoud N. Alsaqer

Acknowledgements

In my deepest sense of gratitude, I would like to thank the Saudi Arabia Education Ministry and University of Hafr Albatin for the funding and giving me the opportunity to carry out this research at the University of York. I would like to express my sincere gratitude to my supervisor Dr. Stuart Cavill for continual guidance and support. His knowledge and expertise were important for this research. Special thanks must go for Mr. Jason Flatt for his incredible help with pressing, cutting and polishing the single crystals. One of his contributions was to help in the preparation of the single crystals ready for analysis. Many thanks go to Dr. James Beevers for PLD, XRD and VSM training, Dr. Jon Barnard for carrying out SEM measurements, Irene Azaceta for AFM training at York JEOL nanocentre and Prof. Vlado Lazarov, Fayzah Talibi and Connor Murrill for performing TEM and SEM measurements. Also, I would also like to thank the mechanical workshop and the technicians of the department of Physics University of York for their help and support.

I would like to thank Dr. Josie Auckett for training and helping with single crystals growth in the department of Chemistry at Durham University. Also many thanks go to Prof. Peter Hatton and Dr. Murray Wilson for training and helping with Laue camera and X-ray generator in the department of Physics at Durham University.

I would like to thank many Diamond light source members, Prof. Sarnjeet Dhesi and the I06-beamline team for helping with soft X-ray spectroscopy. As well as, Prof. Chiu Tang and the I11-beamline team for helping with high resolution powder diffraction. Many thanks also go to Dr. Raymond Fan at Diamond light source and Dr. Gavin Stenning at ISIS Neutron and Muon source for performing SQUID-VSM measurements.

Last but not least, I would like to thank all the people who contributed in some way to this project. Finally, I would like to thank the most precious people in my life "my parents" for their support.

Contents

List of Figures

List of Tables

Chapter 1

Introduction

1.1 Motivation

Magnetoelectric (ME) multiferroic materials exhibit simultaneously both ferroelectric and ferromagnetic orders as well as coupling between these orders. These materials continue to attract considerable attention because of the magnetoelectric effect, which is the ability to control magnetisation by an applied electric field or vice versa, which could reduce power consumption by eliminating the utilisation of electric currents in such electromagnets or spin-torque effects that involves a significant power dissipation due to the Joule heating effect. As such it is expected that ME properties are advantageous for a next generation of data storage, magneto electric sensors and microwave devices [1]. The first prediction of ME effect was in 1888 by Wilhelm Röntgen, who noted that a moving dielectric material when placed in an electric field would become magnetised. Tens years later, the reverse ME effect, induced polarisation when a moving dielectric material through a magnetic field, was observed. In 1894, Curie discussed the possibility of intrinsic ME effect in low symmetry crystals but the theoretical and experimental investigations were not carried out until the 1950's [2]. The first observation of ME effect was in antiferromagnetic Cr_2O_3 by D. N. Astrov in the early 1960's [3]. Later, the linear ME effect was observed in many compounds such as Ti_2O_3, $PbFe_{0.5}Nb_{0.5}O_3$ and $LiCoPO_4$ [4][5][6].

Among the few room temperature single-phase ME multiferroics reported, hexaferrites show potential for device applications as they exhibit a low field ME effect at room temperature [7]. The most common hexaferrite, the M-type, is arranged in different repeating sequences of basic building blocks of R$(SrFe_6O_{11})^{2-}$ and S$(Fe_6O_8)^{2+}$ layers. In this unique structure, Fe ions reside into five different sites: 2a, $4f_2$ and 12k (octahedrally coordinated), $4f_1$ (tetrahedrally coordinated) and 2b (bi-pyramidally coordinated). However, (Co-Ti) substitutions for Fe ions dramatically alter the magnetic properties, in which Ti substitution at the 12k sites decreases the exchange coupling between spins in the R and S blocks, whilst the Ti and Co substitutions change the magnetic anisotropy from uniaxial (along c-axis) to planar (a-b plane) [8]. For x>0.8, Co ions enter the 5-fold trigonal bi-pyramidal (2b) site leading to a formation of cone magnetisation as a result of non-collinear structure [8]. A number of groups have shown that the 5-fold trigonal bi-pyramidal site provides an unusual additional mechanism for electric polarisation based on the displacement of magnetic transition metal ions. For Co entering this site, an off-centre displacement of the cation may induce a larger local electric dipole compered

to Fe [9][10]. The result is to stabilise a longitudinal conical magnetic structure [8], which is of high interest in the field of magnetoelectrics.

The room temperature ME effect in $SrTi_2Co_2Fe_8O_{19}$ hexaferrite was first reported in bulk [11] and, thereafter, in thick polycrystalline films [12]. The ME coupling, α, of (2.4×10^{-10}) s m^{-1} was measured at room temperature with the application of a small electric field or voltage less than 2 V [13], which could be promising for practical applications. Several mechanisms have been proposed in recent years to explain the presence of ferroelectricity in hexaferrites. The dominant mechanism is inverse Dzyaloshinskii-Moriya (IDM), magnetically induced ferroelectricity in which the interaction between neighboring spins gives rise to a non-collinear "spins spiral" structure that may induce a local polarisation [14][15][16][17]. Hence, the non-collinear spin structure plays a key role in understanding the magnetoelectric properties in hexaferrite systems.

The aims of this research were to study temperature dependence of magnetisation of $SrCo_xTi_xFe_{12-x}O_{19}$ polycrystalline M-type hexaferrite, with a variation in the amount of substitution, x, to gain an insight into the role of substitution of M-type hexaferrite on magnetic structure and how this leads to a non-collinear magnetic structure, that may induce an electric polarisation, ME effect. To grow $SrCo_2Ti_2Fe_8O_{19}$ single crystal, and characterise its magnetic properties and temperature dependence of magnetisation, where the substitution induced magnetic anisotropy changes from uniaxial to planar anisotropy. In addition, to investigate the role of strain on magnetic properties in $SrCo_2Ti_2Fe_8O_{19}$ epitaxial thin films.

1.2 Thesis outline

This thesis consists of seven main chapters. Following the introduction in chapter 1, chapter 2 provides background information regarding crystal structure and the properties of M-type hexaferrite. In addition, a brief introduction of the basics of magnetism, ferroelectricity and magnetoelectric effect in M-type hexaferrite. Chapter 3 provides details on all relevant synthesis methods and analytical techniques performed throughout the work of this thesis. Chapter 4 presents the results of the characterisation of the structural and magnetic properties of $SrCo_xTi_xFe_{12-x}O_{19}$ polycrystalline samples with x= 0, 0.7, 1.1, 1.5 and 2, using X-ray diffraction (XRD), Scanning Electron Microscope (SEM), and Vibrating-Sample Magnetometer (VSM)-Superconducting Quantum Interference Device (SQUID), in order to investigate the role of Co-Ti substitution in structural and the magnetic properties as the rate of substitution alters. Chapter 5 is concerned with the growth of $SrCo_2Ti_2Fe_8O_{19}$ and $SrFe_{12}O_{19}$ single crystals, followed by the structural characterisation, XRD and the magnetic properties of the crystals using VSM-SQUID. Special attention has been paid to the magnetic anisotropy analysis which provides an signature of conical magnetic structure. Chapter 6 provides a discussion of the structural and magnetic properties of $SrCo_2Ti_2Fe_8O_{19}$ thin films grown using the Pulse Laser Deposition (PLD) system. The structure of the films were characterised using XRD, Atomic Force Microscopy (AFM) and the magnetic properties were measured using VSM and X-ray Magnetic Circular Dichroism (XMCD). Finally, the conclusions drawn from the previous chapters are summarised and further plans for future works are given in chapter 7.

Chapter 2

Scientific Background

This chapter presents an introduction of hexaferrites, with a special focus on structure and magnetic properties of M-type hexaferrite. In addition, a brief review of the basics of magnetism, ferroelectricity and magnetoelectric effect in M-type hexaferrite is given.

2.1 Hexaferrites

Hexaferrites are transition metal oxides with hexagonal structure. The first hexaferrite materials were discovered in 1950's at Philips Physics laboratory, Netherlands. These materials attracted great attention from scientists and engineers due to their good magnetic properties, high electric resistance, corrosion resistance and low cost raw materials [18][8][19]. Commercially and technologically, hexaferrites have been widely used as permanent magnets, in magnetic stripe cards, loudspeakers and magnetic cores. Generally, hexaferrites are formed of combined oxides and have the basic form $(AO - Fe_2O_3 - MeO)$ where A is a large divalent cation, usually an alkaline earth metal such as Br and Sr, and Me is a transition metal such as Fe, Mn or Co. The structure of hexaferrites can be described as stacked sequences of the three basic blocks S($Me_2Fe_4O_8$), R(AFe_6O_{11}) and T($A_2Fe_8O_{14}$), see figure (2.1). The S block consists of two layers of four oxygen atoms with three transition metal atoms between each layer, in the form of four octahedral sites and two tetrahedral sites. The R block contains three layers of four oxygen atoms. One of the oxygen atoms in the centre layer is replaced with the A cation causing perturbation in the

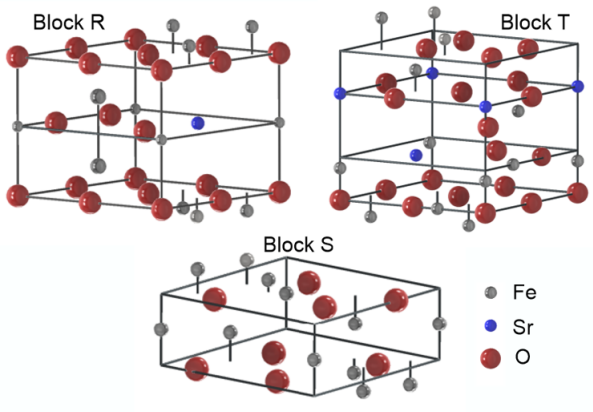

Figure 2.1: Perspective view of S, R and T blocks.

lattice due to size differences, leaving five octahedral sites and one trigonal bipyramidal site. The T block consists of four layers of oxygen atoms with the exception of the oxygen atom in the centre layers which is replaced with A in each layer leaving four octahedral sites and two tetrahedral sites. With a different arrangement of these building blocks, hexaferrites can be classified into six main types: M, W, X, Y, Z and U [20][19]. The molecular formula, unit cell, space group and building blocks of hexaferrites are listed in table (2.1).

Table 2.1: Types of hexaferrites including the molecular formula, unit cell, building blocks and space group.

Name	Molecular formula	Unit cell	Hexaferrite blocks	Space group
M	$AFe_{12}O_{19}$	2M	SRS^*R^*	$P6_3/mmc$
W	$AMe_2Fe_{16}O_{27}$	2W	$SSRS^*S^*R^*$	$P6_3/mmc$
X	$A_2Me_2Fe_{28}O_{46}$	3X	$3(SRS^*S^*R^*)$	$R\bar{3}m$
Y	$A_2Me_2Fe_{12}O_{22}$	3Y	$3(ST)$	$R\bar{3}m$
Z	$A_3Me_2Fe_{24}O_{41}$	2Z	$STSRS^*T^*S^*R^*$	$P6_3/mmc$
U	$A_4Me_2Fe_{36}O_{60}$	U	$SRS^*R^*S^*T$	$R\bar{3}m$

* = rotational symmetry of 180° around the c-axis

The main focus in this thesis will be on M-type hexaferrite. Therefore only the crystal and magnetic structure of M-type are mentioned here, see figure (2.2). M-type hexaferrite has the formula $AFe_{12}O_{19}$ where A is Ba or Sr or Pb (BaM or SrM or PbM). They possess hexagonal structure and belong to ($P6_3/mmc$) space group

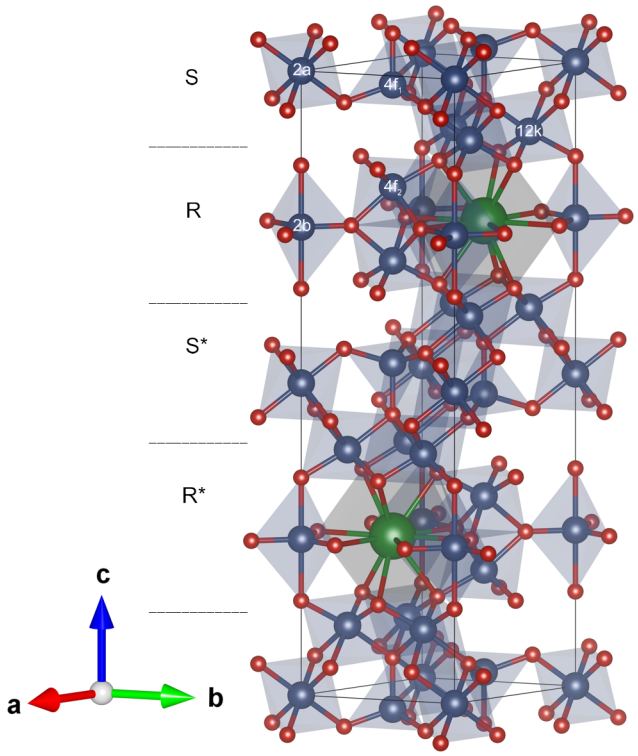

Figure 2.2: M-type hexaferrite structure. The green balls represent A^{2+} cation, the blue balls represent Fe^{3+} ions and the red balls are oxygen. S, R, S^* and R^* are sequences of the basic blocks.

number (194). The lattice parameters for BrM ferrite are a=5.8876 Å and c=23.188 Å whereas for SrM ferrite are a= 5.8844 Å and c= 23.063 Å [8]. The theoretical density for BrM and SrM are (5.28) $g.cm^{-3}$ and (5.11) $g.cm^{-3}$, respectively [8]. The crystal structure is made of two molecular formula units with SRS*R*, where the asterisk indicates a rotational symmetry of 180° around the c-axis. The molecular weight for BrM and SrM are (1111.46) g/mol and (1061.741) g/mol, respectively [8]. In this structure, as shown in figure (2.2), there are three different environments for the transitional metal ions, octahedral (O_h) where the transitional metal ions are surrounded by six oxygen ions ; tetrahedral (T_d) where the transitional metal ions are surrounded by four oxygen ions and trigonal bi-pyramidal (T_{trig}) where the transitional metal ions are surrounded by five oxygen ions. The transitional metal Fe^{3+} ions can reside in five different Wyckoff sites: $2a(O_h)$, $4f_1(T_d)$, $4f_2(O_h)$, $2b(T_{trig})$ and $12k(O_h)$. The (2a) site where one Fe atom is octahedrally coordinated with spin up and the ($4f_1$) site where two Fe ions tetrahedrally coordinated with spin down are located in the S block. The ($4f_2$) sites, where two Fe ions octahedrally coordinated with spin down, and (2b) bi-pyramidal site with spin up, are located in the R block. The (12k) site is located between S and R blocks where six Fe ions are octahedrally coordinated with spin up, see table (2.2) [21][19]. Since, the magnetic moment of a Fe^{3+} ion is 5 μ_B at 0 K, the total magnetic moment per molecule can be expressed as:

$$M(0) = 6\ spins(\uparrow)(12k) - 2\ spins(\downarrow)(4f_2) - 2\ spins(\downarrow)(4f_1) \\ +1\ spin(\uparrow)(2b) + 1\ spin(\uparrow)(2a) = 4\ \mu_B \tag{2.1}$$

Hence, the theoretical saturation magnetisation per formal unit at 0 K is 4×5=20 μ_B. In case of doped M-type hexaferrite, the value will be different depending on the cation substitutions and their occupancy [19].

Table 2.2: Coordination and spin orientation of sublattices in M-type hexaferrite

Cation	Wyckoff position	Blocks	Coordination	Spin orientation	Number of Fe^{3+} ion
Fe1	2a	S	Octahedral	Up	1
Fe2	2b	R	Bi-pyramidal	Up	1
Fe3	$4f_1$	S	Tetrahedral	Down	2
Fe4	12k	R-S	Octahedral	Up	6
Fe5	$4f_2$	R	Octahedral	Down	2

Hexaferrites have been synthesised for more than 60 years in various forms; polycrystalline, nanoparticles, single crystals, thin films and fibres. Depending on the preparation method, the shape, particle size, impurity, agglomeration and homogeneity are varied and as a result, the electric and magnetic properties show a wide degree of variation. Polycrystalline hexaferrites are usually obtained by solid state reaction method which involves mixing and milling raw materials then sintering them at high temperature. The resultant may contain impurities and have limited homogeneity. Another method used to synthesise hexaferrites is co-precipitation. In short, the process starts by dissolving the starting materials in a suitable solution and then adding a precipitating agent to obtain co-precipitated solid powders. Although this method involves mixing, drying and sintering, its main advantage is its lower sintering temperature, around $\sim 700 - 900$ ℃ much lower than that required

for solid state method, which is around $\sim 1000-1400$ ℃ [8]. More details and other synthesising methods can be found in ref [21][19].

2.2 Magnetism

2.2.1 Magnetic interactions and ordering

In absence of a magnetic field, the interaction between magnetic moments in transition metals may give rise to long range magnetic ordering. Consider a system of two atoms i and j, having spin angular momentum (S_i, S_j) and zero orbital angular momentum (L=0), so J=S. S_i interacts with neighbouring spin, S_j, tending to align in the same orientation in order to minimise the total energy of the system. This is known as exchange interaction. Exchange interaction is a quantum effect resulting from competition between kinetic energy and Coulomb repulsion with respect to Pauli exclusion principle, which forbids two electrons to enter the same quantum state. The exchange energy can be described by the Heisenberg model, with a Hamiltonian given by [22]:

$$\hat{H} = -\sum_{ij} J_{ij} S_i . S_j \tag{2.2}$$

where J_{ij} is the exchange constant between the i^{th} andj^{th} spins. Applying a magnetic field to the system, the moments tend to align with the direction of the applied field, the appropriate Hamiltonian for the system will be:

$$\hat{H} = -\sum_{ij} J_{ij} S_i . S_j + g\mu_B \sum_{j} S_j . B \tag{2.3}$$

where the additional term is the Zeeman energy: g is g-factor ≈ 2, μ_b is Bohr magneton and B is the applied field.

For a very weak or zero exchange interaction, such as in the paramagnetic state, the interaction between spins is negligible without an applied magnetic field, and can be treated independently or as randomly oriented. Therefore, the total of magnetisation is zero, in a zero applied field. In cases of non negligible exchange interaction, depending on the alignment of a spin with respect to adjacent spins, magnetic order structure can be collinear and/or non-collinear. A collinear magnetic order is where spins are coupled parallel or antiparallel to their nearest neighbours, i.e. the angles between the nearest neighbour and the next nearest neighbour spins are 0 or π. A collinear system can be classified into ferromagnetic, antiferromagnetic, ferrimagnetic and superparamagnetic states, see figure (2.3). In ferromagnetism, the spins are aligned parallel to each other, and therefore, have a large spontaneous magnetisation. The exchange constant is positive, $J > 0$. A few elements are ferromagnetic at room temperature, such as Fe, Ni and Co. In antiferromagnetism, spins are aligned antiparallel, so that the spins cancel out and the exchange constant is negative, $J < 0$, hence the total magnetisation is zero, at 0 K. Above 0 K, due to thermal effects and spin canting, antiferromagnetic have a small positive susceptibility at all temperatures, such as in Fe_2O_3 at 250 K and MnO below 116 K [22][23]. Ferrimagnetism is a special case of antiferromagnetism, in which the spins are aligned antiparallel, but with a different moment magnitude on differing sublattices, thus, having a net of magnetisation unlike antiferromagnetism. The exchange

constant is generally negative, $J < 0$ for $NiFe_2O_4$. $SrFe_{12}O_{19}$ is ferrimagnetic at room temperature [24].

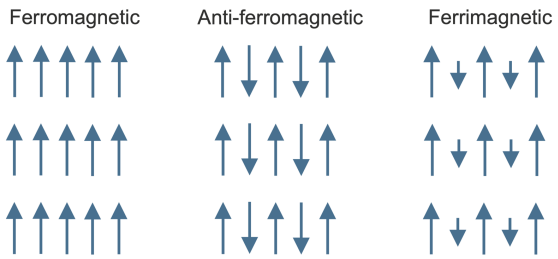

Figure 2.3: Representation of collinear alignment of spin magnetic moment in ferromagnetic, anti-ferromagnetic and ferrimagnetic order.

Superparamagnetism is a special case in magnetic nanomaterials. It appears in extremely small ferromagnetic or ferrimagnetic nano particles [25]. Being small in size, each particle acts as a single domain that requires a small activation energy to flip its magnetisation compared to thermal energy, hence, the single domains fluctuate continuously under the influence of temperature. The Superparamagnetic behaviour is described by a relaxation time τ, which defines as the time required to achieve zero magnetisation after removing an external magnetic field, this can be expressed as:

$$\tau = \tau_0 \, exp\left(\frac{KV}{k_B T}\right) \tag{2.4}$$

where τ_0 is typically 10^{-9} s, K is the anisotropy constant and V is the volume of the particle, T is the temperature and k_B is the Boltzmann's constant. Therefore, the relaxation time increases with a decrease in temperature. It should be noted that measuring time, t, is an important parameter, if $\tau > t$ the system would appear static [22].

Direct exchange interaction occurs between neighbouring spins in transition metals (TM), whereas, indirect exchange interaction occurs in system where the TM ions are separated by a non magnetic ion. If two magnetic (TM) ions are separated by a non-magnetic (O^{2-}) ion, in which each of TM has an unpaired electron in the 3d orbital that interacts with the 2p electrons in the oxygen ion, superexchange can occur, see figure (2.4).

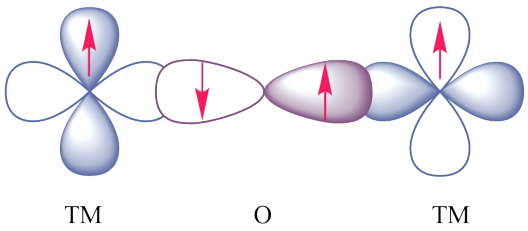

Figure 2.4: Schematic diagram of the superexchange interactions between unpaired 3d electrons in two transition metals (TM) and the p-orbital of an oxygen ion (O).

The strength of the superexchange depends on the degree of overlap between p and d-orbitals as well as the angle in TM-O-TM. According to Goodenough-

Kanamori-Anderson (GKA) rules, if the superexchange interaction of two half-filled d-orbitals makes an angle of 180°, then the interaction is strong and anti-ferromagnetic, whereas if the angle is 90°, the interaction will be weak and ferro-magnetic. In cases where the superexchange interaction is between half-filled and empty or filled orbitals, then interaction is weak and ferromagnetic [26][22][24].

2.2.2 Spin Orbit Coupling (SOC)

The spin orbit coupling in an atom arises from interaction between its spin motion and its orbital motion. It can be seen as a magnetic field generated by the electron's orbital motion interacting with the spin leading to a split in the electron's atomic energy levels and can be described as:

$$\hat{H}_{SO} = \lambda L.S \tag{2.5}$$

where λ is spin orbit coefficient and L and S are orbital and spin angular momentum, respectively [22][27].

2.2.3 Dzyaloshinskii–Moriya interaction (DM)

Dzyaloshinskii–Moriya interaction (DM) is similar to superexchange, but the interaction occurs between magnetic ions via spin orbit coupling, not a non magnetic ion. This is an anisotropic exchange interaction that results from the contributions of exchange interactions and spin orbit interactions. The interactions occur between the excited state of one ion and the ground state of the other ion introducing a non collinear spin ordering or/and a weak ferromagnetism in antiferromagnet, see figure (2.5). Spin S_i interacts with S_j leading to an additional term in the Hamiltonian that can be written as:

$$\hat{H}_{DM} = D_{ij}(S_i \times S_j) \tag{2.6}$$

where D_{ij} is a constant vector, known as the DM coefficient. The value of D_{ij} and its direction depends on the symmetry of the system. D_{ij} no longer exist when the inversion symmetry is located at the centre between i and j locations, i.e. at r_{ij}. If a mirror plane exists perpendicular to i and j locations through r_{ij}, D_{ij} is parallel to the mirror plane or perpendicular to ij. When there is mirror plane including i and j, D_{ij} is perpendicular to the mirror plane. The DM interaction favours canted (slightly rotated) spins which are a key component for magnteoelectic property [22].

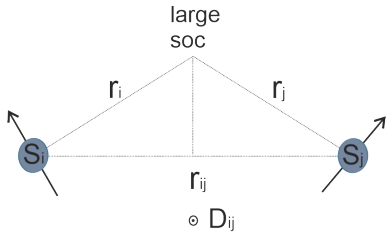

Figure 2.5: Scheme of the Dzyaloshinskii-Moriya interaction between two magnetic ions. r_{ij} is at the middle and equal to $\frac{r_i+r_j}{2}$.

In a non-collinear system, the spins of the nearest neighbour with exchange, J_1 and the next nearest neighbour with exchange, J_2 are neither parallel or antiparallel

such as for Cr_2O_3 and $TbMnO_3$ [28]. The competing interaction between neighbour spins lead to angles θ that are not equal to 0 or π which gives rise to spin spiral and conical structures [22]. The energy of the system can be written:

$$\hat{H} = -\sum_{ij}(J_1 S_i.S_j + J_2 S_i.S_{j+1}) = -2NS^2(J_1 \cos\theta + J_2 \cos 2\theta) \tag{2.7}$$

where N is the number of atoms in each plane and S is the spin. At the equilibrium, the energy is minimised by taking $\frac{\partial \hat{H}}{\partial \theta} = 0$ [22],

$$(J_1 + 4J_2 \cos\theta)\sin\theta = 0 \tag{2.8}$$

The solutions for equation (2.8) are:

$$\sin\theta = 0, \quad where \quad \theta = 0, \pi \tag{2.9}$$

or

$$cos\theta = -\frac{J_1}{4J_2} \tag{2.10}$$

The solution in equation (2.10) represents a helical order with the conditions $|J_1| < 4|J_2|$. i.e. the second nearest-neighbor interaction must be strong [22][29]. Depending on the value of the exchange interaction, the angle between spins and angle between spins and the magnetic modulation wavevector (Q), a non collinear system can be classified into proper-screw, cycloidal, longitudinal conical and transverse conical structures. In a proper-screw structure, the spin spiral rotation axis $(S_i \times S_j)$ is parallel to modulation wavevector, Q. In a cycloidal structure, the spin spiral rotation axis $(S_i \times S_j)$ is perpendicular to modulation wavevector, Q, as shown in figure (2.6). By applying a weak magnetic field perpendicular to Q, to longitudinal conical type, transverse conical structure may be induced [28].

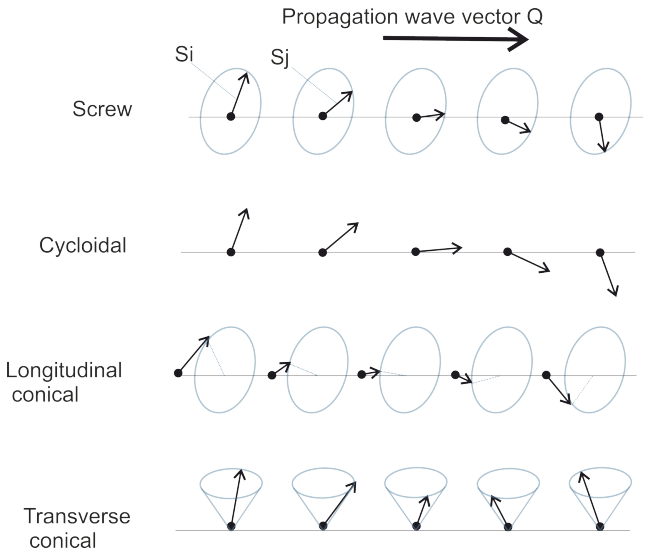

Figure 2.6: Scheme of non-collinear magnetic structures (Screw, Cycloidal, Longitudinal conical and transverse conical) on a one dimensional array of magnetic moment S.

2.2.4 Local environment

In a magnetic material, the local environment is crucial in which the interaction between the magnetic ion and the surrounding ions may cause a perturbation on energy levels and affect the magnetic properties. In this thesis, we will concentrate on crystal field as this has an important effect in M-type hexaferrite.

2.2.5 Magnetic anisotropy

Magnetic anisotropy is defined as the dependency of the magnetic properties for a system on a preferred direction. It affects the shape of the hysteresis loop and controls the coercivity and remanent magnetisation. One type of magnetic anisotropy is magnetocrystalline anisotropy, (MCA), which is defined as the energy required to change the magnetisation in a crystal from its easy to hard axis. For example, the magnetic properties for a hexagonal single crystal may differ when measuring along its easy and hard axes. By applying a field on [0001], the direction of the easy axis (c-axis), the crystal reaches saturation magnetisation at a lower field than other directions. MCA is an intrinsic property of a magnetic material dependent on the crystal lattice structure and independent on grain size and shape.

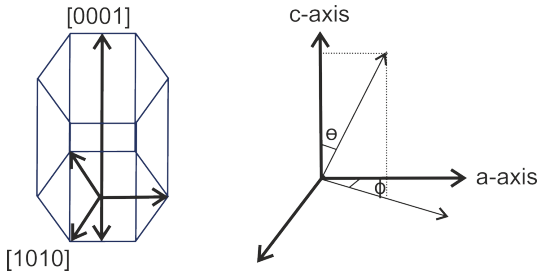

Figure 2.7: Direction of magnetisation in a hexagonal system relative to the c-axis defining the angles θ and ϕ.

The origin of MCA arises from spin orbit interaction and its strength depends on the symmetry of the crystal, spin orbit interaction and the partial quenching of the angular momentum through crystal field interactions, see section (2.2.6). MCA leads to an additional energy term in the magnetic free energy [27]. For a hexagonal system the anisotropy energy can be described by:

$$E_a = K_0 + K_1 \sin^2\theta + K_2 \sin^4\theta + K_3 \sin^4\theta \cos 4\phi \tag{2.11}$$

where K_1, K_2 and K_3 are anisotropy constants, θ is the angle between magnetisation and the c-axis and ϕ is the angle between the projection of magnetisation vector in the basal plane of the crystal and one of the a-axis, see figure (2.7). If K_1 is positive and $K_2 + K_1 > 0$, the c-axis is the easy axis, whereas, for $K_2 < -K_1$, the direction of easy magnetisation lies in the basal plane. In case K_1 is negative and $2K_2 > -K_1$, the basal plane is the direction of easy magnetisation, whereas, for $2K_2 < -K_1$, the direction of easy magnetisation forms a cone with an angle, θ with respect to the c-axis. It is worth noting that, the anisotropy constants are temperature dependent; K_1 reduces as the temperature increases [22][27].

Another type of magnetic anisotropy is the shape anisotropy, which originates from the dipole-dipole interactions and is related to the geometrical shape of the magnetised sample. If a sample is not spherical, it will be easier to magnetised it along a long axis. The field required to magnetise the sample must overcome the demagnetising field (H_d), which is created by the magnetisation of the sample. Due to the finite size of the sample, each end of the sample acts as a pole, generating an internal magnetic field, H_d, in a direction opposite to the magnetisation in the material, see figure (2.8). H_d is proportional to the magnetisation and strongly dependent on the shape of the sample and the direction with respect to applied field. Assuming the demagnetising field is uniform inside the sample, H_d is defined by [27]:

$$H_d = -NM \tag{2.12}$$

where N is the demagnetisation factor, which is calculated only from the shape of the sample [30][29].

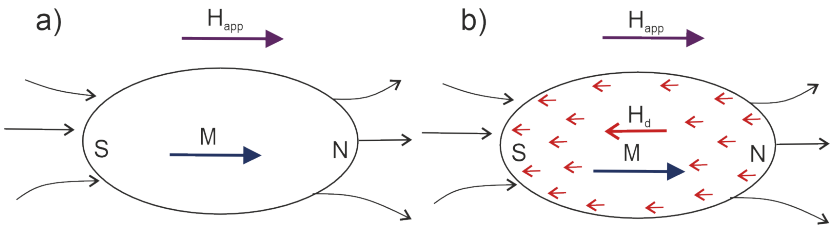

Figure 2.8: Demagnetising field inside a finite size of magnetic material placed in an external applied field, H_{app}. (a) magnetisation is produced outside the sample, in the direction of the applied field. Simultaneously, (b) a demagnetised field, H_d developed inside the sample, in the opposite direction of the applied field due to the presence of a magnetic charge or poles at the surface.

2.2.6 Crystal field effect (CT)

The crystal field effect is an electric field that arises from surrounding anion distribution in the crystal. The interaction between the d-electrons of the cation and the p-electrons of ligands induce a non-spherical electrostatic potential, leading to the splitting of atomic energy levels. The size of the splitting effect depends on the local environment and the oxidation state of the cation, a higher oxidation state leads to a larger splitting and the symmetry of the local environment [22]. In M-type hexaferrite structure, three different environments for Fe^{3+} ions are present. They are octahedral; tetrahedral and bi-pyramidal, see figure (2.9).

In octahedral geometry, where the Fe^{3+} ion is surrounded by six O^{2-} ligands, the 5d-orbitals are split into two sets of energy levels; three-fold t_{2g} levels (these are the d_{xy}, d_{xz} and d_{yz}) and two-fold e_g levels (these are d_z^2 and $d_{x^2-y^2}$), with an energy difference, $\Delta_{Oct} = 10D_q$ (which is the crystal filed splitting parameter). The t_{2g} levels are shifted by $-4Dq$ and e_g levels are shifted by 6Dq, where 10Dq is defined as the separation between t_{2g} and e_g levels. The t_{2g} levels have lower energy than the e_g levels due to the smaller overlap with p-orbitals, i.e. it requires less energy to have an electron in one of the t_{2g} orbitals than to put an electron in one of the e_g levels orbitals.

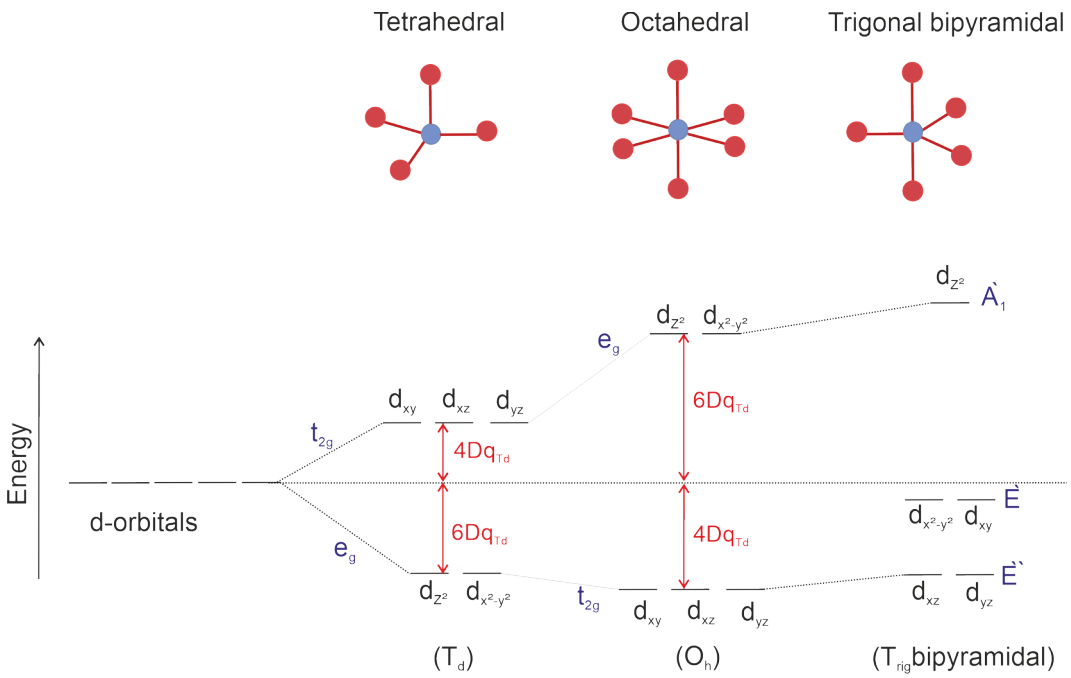

Figure 2.9: Scheme of the crystal field in octahedral, tetrahedral and trigonal bi-pyramidal environments.

In tetrahedral geometry, where the Fe^{3+} ion is surrounded by four O^{2-} ligands, the two-fold e_g levels are lower in energy by -6Dq and the three-fold t_{2g} levels are shifted by 4Dq. The splitting in energy levels for T_d environment is given in equation (2.13), this is lower than in the octahedral case due to the fact that the ligands are not directly orientated towards the d-orbitals unlike those in the octahedral environment:

$$Dq_{Td} = -\frac{4}{9} Dq_{Oh} \tag{2.13}$$

The bi-pyramidal geometry is a special case of distorted octahedron. The Fe^{3+} ion is surrounded by five O^{2-} ligands and the 5d-orbitals are split into two-fold E'' (d_{yz} and d_{xz}); two-fold E' ($d_{x^2-y^2}$ and d_{xy}) and one-fold A_1' (d_z^2). E'' is the lowest energy level and A_1' is the highest energy level. The splitting in energy levels for T_{rig} environment is described by D_τ and D_σ crystal field parameters as [31]:

$$D_\tau = \frac{e}{168}\left(\frac{16q}{R_c^5} - \frac{9q}{R_a^5}\right)\bar{r}^4 \tag{2.14}$$

and

$$D_\sigma = \frac{e}{14}\left(\frac{4q}{R_c^3} - \frac{3q}{R_a^3}\right)\bar{r}^2 \tag{2.15}$$

where q is the ligands charge, R_c and R_a are the distance to the two ligands along the c-axis and to the three ligands along the a-axis, respectively. $\bar{r}^n$ is the mean n power radius of the d-electrons of the centre ion, n=2, 4 [22].

Generally, for 3d ions, the crystal field interaction is stronger compared with spin orbit interaction, therefore, the hund's third rule, which is "spin-orbit interaction is the next most significant energy term after Coulombic effects", does not apply

(exception for d^5 and d^{10} where L=0). This explains the discrepancy between the values of the expected magnetic ground state, given by $\mu_{eff} = g_J\sqrt{J(J+1)}$ and experimental values, suggesting that these systems favour a ground state where the orbital angular momentum L=0. Hence, total angular momentum is equal to the spin angular momentum J=S and g_J=2, known as orbital quenching, for more details see [22]. However, in a real crystal structure, the orbital angular momentum may not be entirely quenched due to a small spin-orbit interaction that acts as perturbation leading to new exited states. This results in a g-factor, which slightly differs from the spin only value of 2, as a result of the spin contribution having a slightly larger value, due to the orbital angular momentum contribution, which may lead to a preferred magnetisation direction (anisotropy)[22][32][33][34].

2.2.7 Magnetic properties of M-type hexaferrite

$SrFe_{12}O_{19}$ and $BaFe_{12}O_{19}$ M-type hexaferrite are intrinsically ferrimagnetic up to $T_c \simeq 733$ K. They have a high coercivity range from (20-40) kOe and a large uniaxial crystal anisotropy along the c-axis range from (3.3-3.5) $10^5 Jm^{-3}$. The magnetic ordering in M-type hexaferrite can be described by superexchange interactions, in which the interaction between magnetic ions occurs via ligands, see superexhange interaction (2.2). Replacing Ba with Sr ion, which has a smaller ionic radius, creates a slight perturbation in the lattice, the superexchange bond angle in Fe-O-Fe sites (2a and 2b sites) near the A^{2+} ion changes from 116° (with Ba) to 123° (with Sr). This introduces local strain located in the R block as well as a slight increase in the magnetic properties of SrM, such as the Curie temperature, which are $T_c \simeq 723$ K and 733 K for $BaFe_{12}O_{19}$ and $SrFe_{12}O_{19}$ respectively, and the saturation magnetisation, which are 72 emu/g and (92-74) emu/g for $BaFe_{12}O_{19}$ and $SrFe_{12}O_{19}$ respectively [8][19].

Moreover, substitution of Fe^{3+} magnetic ions for other magnetic or/and non magnetic ions dramatically alters the magnetic properties. The most interesting substitution is the $(Co^{2+} - Ti^{4+})$ pair. The substitution of Ti^{4+} ions weakens the exchange coupling between R and S blocks whereas the substitution of Co^{2+} changes the magnetocrystalline anisotropy from uniaxial (along c-axis) to planar (a-b plane) [8]. Zhang et al.(2012) studied the effect of a variation in the substitution value in $BaCo_xTi_xFe_{12-2x}O_{19}$ with x=0.9 to 1.4. In their work, the samples were prepared using the solid state reaction method. The results show that the saturation magnetisation decreased from 60.2 emu/g to 36.5 emu/g, the coercivity also decreased from 137.8 Oe to 24.8 Oe, for substitution with x=0.9 and 1.4, respectively. They attribute the reduction in magnetic properties with an increase in the substitution value down to the fact that replacing Fe^{3+} ions, which have a magnetic moment of 5 μ_B, with Ti^{4+} non-magnetic ion and Co^{2+} ion, which have a smaller magnetic moment of 3 μ_B, will reduce the total magnetic moments as well as change the magnetocrystalline from uniaxial (along the hexagonal c-axis) to basal plane (a,b plane of hexagonal cell) when $x \approx 1.1$. The best magnetic properties and highest permeability were obtained in the sample with $x \approx 1.2$ [35].

Another widely studied substituted system is where Fe^{3+} ions have been replaced by Sc^{3+} ions, $BaSc_xFe_{12-x}O_{19}$. Neutron diffraction study by O.P. Aleshko.(1968) for single crystals with $0 \leq x \leq 1.8$ shows that the spin ordering is collinear within

blocks and non collinear between blocks i.e the direction of the spin axes may align with angles between blocks resulting in helical or other form of conical spin structure. The reason for this is related to the replacement of Fe^{3+} ions with non magnetic ions which disturb the exchange coupling between blocks [36].

Recently, Kumar.(2021) revealed that $BaFe_{12}O_{19}$ exhibits a conical spin structure at low temperature based on X-ray absorption spectra, X-ray magnetic circular dichroism (XMCD) and neutron diffraction studies at low temperature. From XMCD of the $L_{2,3}$-edges, they calculated the spin moment using the sum rules to be $m_{spin\|c}$ ≈0.2009 μ_B/Fe^{3+} and 0.56228 μ_B/Fe^{3+} for H=0 T and 0.5 T, respectively, and $m_{spin\perp c}$ ≈0.0538 μ_B/Fe^{3+} and 0.15058 μ_B/Fe^{3+} for H=0 T and 0.5 T, respectively. The presence of spin moment perpendicular to the c-axis is evidence of the non-collinear magnetic structure. The neutron diffraction study at 1.5 K confirmed the XMCD result by the presence of a $(00l \pm \tau)$ reflections, where l has odd values that arise from the magnetic structure, since these reflections were forbidden by the space group of the crystal. Based on this evidence, the authors suggested undoped M-type hexaferrite exhibits a conical spin structure at very low temperature [37]. This result raises many questions; why is the conical spin structure observed at very low temperature, < 4 K? At what temperature does the conical spin structure form? What is the mechanism behind it and is the conical spin structure, if it exists, capable of introducing the ME effect?

2.3 Ferroelectricity

2.3.1 An overview of Ferroelectricity

A ferroelectric material exhibits a spontaneous electric dipoles (polarisation) that can be switched by applying an external electric field. They are distinguished by high non-linear permittivities as well as the ability of retaining some polarisation after the removal of the external electric field, therefore, showing hysteretic behaviour. Typical ferroelectric materials are electrical insulators with full or empty d-orbitals bonding with p-orbitals of the anion, i.e. d^0, such as Ti^{4+} and Nb^{5+}. The polarisation requires a net of electric dipoles that can only be possible in a non-centrosymmetric structure, hence all ferroelectric materials break inversion symmetry. Like magnetic moments in a ferromagnetic, in a ferroelectric, electric dipoles can align parallel to each other (ferroelectric), antiparallel (antiferroelectric), or antiparallel with different magnitude (ferrielectric). The ferroelectric state develops usually at low temperature, below a critical temperature, T_c. Above T_c, the material is paraelectric [38]. The perovskite $BaTiO_3$ is a prototypical ferroelectric. Depending on temperature, the crystal symmetry evolves from a cubic structure above T_c, where the Ti ion is located at centre of octahedral TiO_6, to a rhombohedral structure below T_c, where Ti ion is positioned off centre. The former state is paraelectric whereas the latter is ferroelectric, see figure (2.10) [39].

The origin of ferroelectricity can be identified as polarisation induced by crystal structure or by magnetic structure. There are a variety of ferroelectric mechanisms that are independent of the magnetic structure such as in a compound that contains elements with ns^2 lone pair electrons, in which two valence electrons could have participated in chemical bonds using (sp) hybridised state but that are not shared with

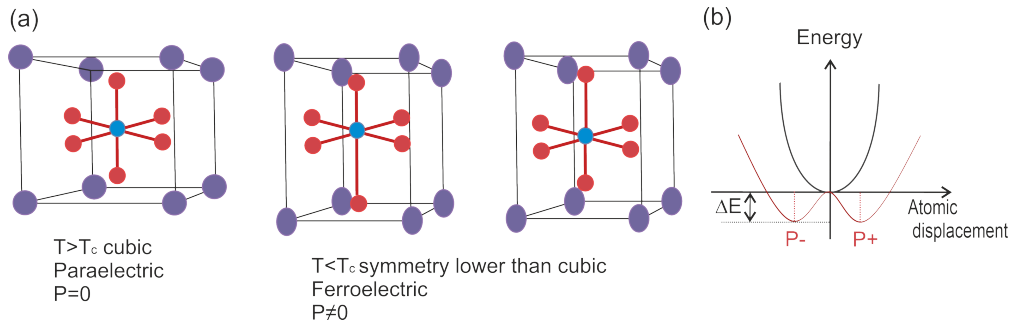

Figure 2.10: (a) Scheme of $BaTiO_3$ perovskite structure above and below T_c. The red circles represent (O^{2-}), the light blue circle represents (Ti^{4+}) and the dark blue circles represent (Ba^{2+}). (b) Scheme of energy potential of $BaTiO_3$. The black parabolic and red curves represent paraelectric and ferroelectric States, respectively. The ferroelectric state shows double well feature and ΔE is ferroelectric stabilisation energy.

another atom, thus showing a high polarisability e.g. $BiFeO_3$. Another mechanism is the geometric structure transition, for example, structure distorted by displacement of cation from the centre of a coordination polyhedra, e.g. $BaTiO_3$ without tilting and $NaNbO_3$ with tilting [39]. This displacement or distortion is at a local level, that could develop into a system where all electric dipoles line up, the ferroelectric phase or a system where the electric dipoles oppose, the antiferroelectric phase. In addition, ferroelectricity can arise from charge ordering. In strongly correlated systems, due to the strong interaction between electrons, ordering of charge carriers takes place on inequivalent sites in which disproportionation in charge leads to polarisation such as in $LuFe_2O_4$ [40].

The microscopic mechanism of magnetic ordering induced polarisation is usually described in three different mechanisms, see figure (2.11). The first mechanism is symmetric exchange striction, the interaction between collinear spins in frustrated magnets may induce striction in a certain direction producing finite electric polarisation, p. The polarisation is proportional to the magnetic moments which can be describe as $P_{ij} \propto e_{ij}(S_i.S_j)$ where e_{ij} is the unit vector connecting two sites, S_i and S_i are the magnetic moment at site i^{th} and j^{th}, respectively. This mechanism explains the ME effect in Cr_2O_3 [17].

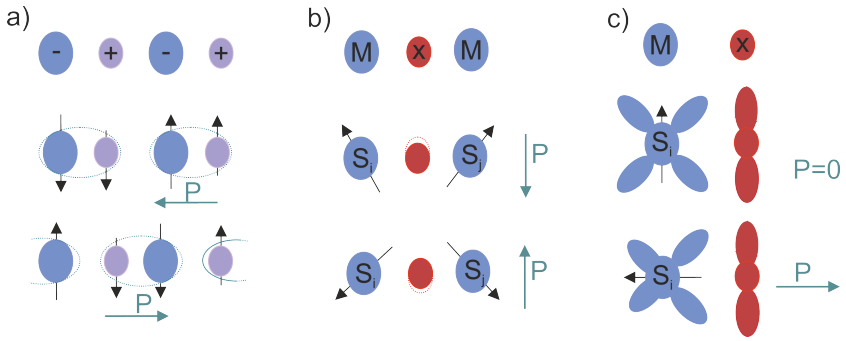

Figure 2.11: Scheme of three possible mechanisms of ferroelectricity induced by spin magnetic order. (a) Exchange-striction model arising from the symmetric spin exchange interaction. (b) Spin-current model arising from the antisymmetric spin exchange interaction and (c) Spin p-d hybridisation model arising from spin orbit coupling.

The second mechanism is spin current or inverse Dzyaloshinskii-Moriya (DM) which is based on the interaction between non-collinear spins leading to the displacement of the intervening ligand atom (oxygen) through spin-orbit coupling. For certain magnetic structures, such as cycloidal or transverse conical, the electric polarisation may be induced perpendicular to both spin spiral ($S_i \times S_j$) and the propagation vector e_{ij}, see figure (2.12). The net polarisation is described as $P_{ij} \propto e_{ij} \times (S_i \times S_j)$. This mechanism explains the presence of electric polarisation in $TbMnO_3$ and is proposed for hexaferrites [41].

The third mechanism is p-d hybridisation which is based on the interaction between transition metal and ligand (oxygen), this produces electric polarisation through spin-orbit coupling, which can be expressed as $P_{il}[(S_i.e_{il})^2]e_{il}$. This mechanism explain the presence of electric polarisation in low symmetry structure with non-collinear magnetic structure such as $CuFeO_2$ and $CuCrO_2$ [42][28].

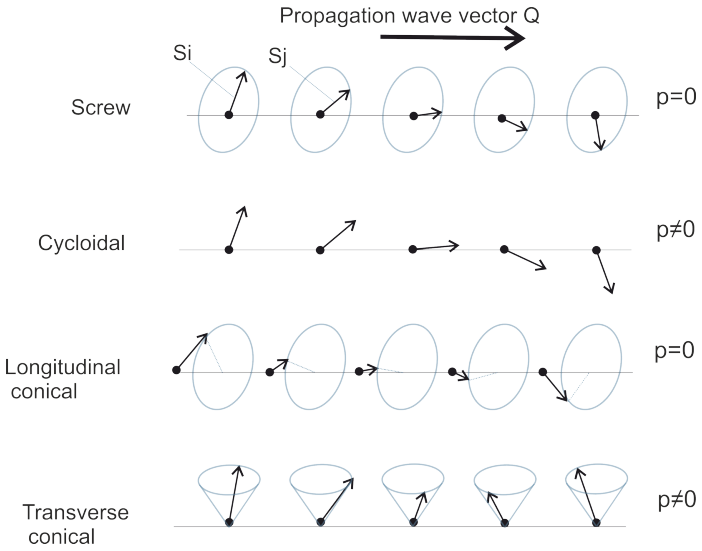

Figure 2.12: Scheme of non-collinear magnetic structures on a one dimensional array of magnetic moment. Electric polarisation is induced with cycloidal and transverse conical. For screw and longitudinal structures, no induction of p.

2.3.2 Ferroelectricity in M-type hexaferrite

Ferroelectricity in M-type hexaferrite is still not fully understood. Many studies attribute the induction of ferroelectric phase to inverse Dzyaloshinskii-Moriya (IDM) mechanism, with discrepancy about spin magnetic structure and whether M-type hexaferrite has longitudinal or transverse magnetic structure that induce polarisation [11][14][16].

Another explanation is that BaM exhibits quantum paraelectric behaviour similar to $SrTiO_3$ in which Fe^{3+} ions are shifted off centre on the bi-pyramidal site. Cao *et al.*(2015) carried out neutron diffraction and dielectric property measurements on BaM single crystal grown by float zone. The study shows that the displacement of Fe^{3+} ions off centre at the 2b site, is non-zero at 4 K and double its value compared to 300 K, i.e temperature dependent [43]. Shen, S., *et al.*(2014) supported the argument of the existence of electric polarisation based on displacement of transition

metal Fe^{3+} ion from the centre of O_5 trigonal bi-pyramidal unit in hexaferrites. Due to the competition interaction between the long range Coulomb interaction and the short range Pauli repulsion in the bi-pyramidal unit, with proper lattice parameters lead to displacement of Fe^{3+} ion from centre which induces a local polarisation. This suggestion is based on calculations of the local energy potential of the bi-pyramidal unit for Ba/ SrM hexaferrite and the temperature dependence of dielectric permittivity measurements. They observed that SrM has quantum paraelectric behaviour along the c-axis inducing p along the c-axis. In addition, by substituting Ba with Sr, the p will decrease, this is in disagreement with the previous works stated above [44].

P.S. Wang, *et al.*(2014) predicted that BaM hexaferrite shows an antiferroelectric - ferrimagnetic state at room temperature and by applying an external electric field, a ferroelectric state can be obtained. Based on their first principal calculations they suggested that the ferroelectric state in BaM hexaferrite is a metastable state resulting from a geometrically frustrated antiferroelectric state at the bi-pyramidal site, where Fe^{3+} is displaced out of the mirror plane site, and is attributed to the instability of the ferroelectric state to the high energy cost for flipping a dipole [45]. Their work agrees with the X-ray diffraction study by W.D.Townes.(1967) [46] and the Mössbauer study by J.G Rensen.(1969) [47].

G.Tan, *et al.*(2016) reported that $SrFe_{12}O_{19}$ exhibits large intrinsic ferroelectricity and ferromagnetism as well as magnetocapacitance effect at room temperature. They also highlighted the role of heat-treatment of the material in oxygen to improve the electric and magnetic properties by reducing the oxygen vacancies, hence suppression formation to Fe^{2+}. In their work, P-E measurements were obtained for both annealed and untreated $SrFe_{12}O_{19}$ polycrystalline samples [48]. The results show that the untreated sample exhibits a "banana shaped" P-E loop, similar to previous work G.Tan.(2013) due to the current leakage whereas the annealed sample shows a saturated ferroelectric hysteresis loop [48].

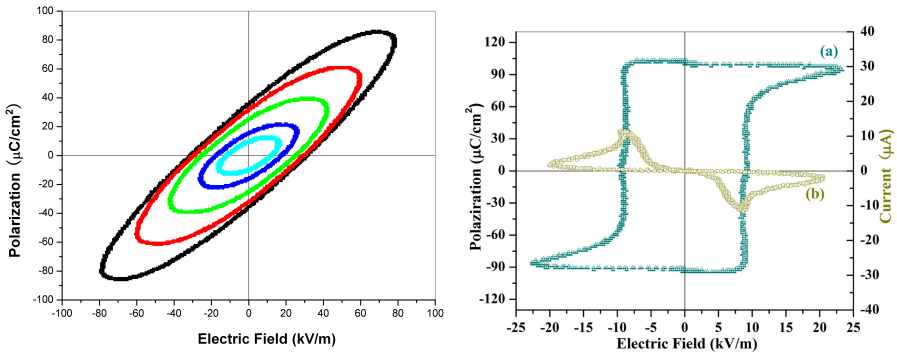

Figure 2.13: P-E loop from reference [49]. On the right, P-E loop for non-treated $SrFe_{12}O_{19}$ ceramic (figure: E from supporting materials). On the left, the saturated P-E loop for $SrFe_{12}O_{19}$ and a plot of the current as a function of voltage.

The ferroelectric behaviour for the latter sample was confirmed by the presence of two nonlinear I-V peaks along with polarisation switching, see figure (2.13). Moreover, dielectric measurement as a function of temperature for the latter sample with different frequencies show anomalies at ≈ 763 K that confirm the intrinsic ferroelectricity of $SrFe_{12}O_{19}$. They attributed the origin of the ferroelectricity in

$SrFe_{12}O_{19}$ to the displacement of Fe^{3+} ions off centre in the bi-pyramidal site and disagree with argument of the presence of quantum paraelectric behaviour [49].

2.4 Multiferroic Magnetoelectric effect (ME)

2.4.1 An overview of Magnetoelectric effect

The magnetoelectric (ME) multiferroic effect is defined as the induction of electric polarisation with the application of an external magnetic field, or vise versa. The induction of magnetisation with application of an external electric field is called the inverse ME effect. There are very few magnetoelectric materials due to the fact that ferroelectricity and ferromagnetism tend to be mutually exclusive. Ferroelectricity typically requires no unpaired electrons and breaks spatial inversion symmetry. In contrast, ferromagnetism requires unpaired electrons and breaks time reversal symmetry [17][42]. The ME effect can exist in a single phase compound, i.e. coexistence of electric dipoles and magnetic moments, simultaneously, as well as direct coupling between the orders. The single phase ME materials can be classified into type-I and type-II multiferroics. Type-I, also known as improper ferroelectrics, where the magnetic and electric ordering are separated with two distinct temperatures, i.e. $T_N(FM) \neq T_c(FE)$ such as in $BiFeO_3$, $T_N = 643$ K and $T_c = 1100$ K. Type-II, known as proper ferroelectrics, where the magnetic ordering breaks the inversion symmetry directly inducing ferroelectricity. Both properties exhibit the same transition temperatures, i.e. $T_N(FM) = T_c(FE)$ such as $TbMn_2O_5$ at 28 K [50]. Most of single phase ME materials show very weak ME coupling at room temperature.
In composite materials, that contain two or more phases of desirable properties, the ME coupling results from a product property of magnetostrictive and piezoelectric compounds, as described in equation (2.16) i.e. strain mediated coupling [51][2].

$$\text{ME effect} = \frac{\text{electrical}}{\text{mechanical}} \times \frac{\text{mechanical}}{\text{magnetic}} \tag{2.16}$$

The ME effect is obtained from expanding the relation for the free energy of a material in magnetic and electric fields, $\vec{H}$ and $\vec{E}$ at constant temperature and mechanical stress.

$$\begin{aligned} F(\vec{E},\vec{H}) = F_0 - P_i^S E_i - M_i^S H_i - \frac{1}{2}\epsilon_0\epsilon_{ij}E_iE_j - \frac{1}{2}\mu_0\mu_{ij}H_iH_j \\ -\alpha_{ij}E_iH_j - \frac{1}{2}\beta_{ijk}E_iH_jH_k - \frac{1}{2}\gamma_{ijk}H_iE_jE_k - ... \end{aligned} \tag{2.17}$$

where P_i^S and M_i^S denote the spontaneous polarisation and magnetisation, respectively. ϵ is the permittivity and μ is the permeability, α is tensor known as the linear ME effect and β and γ are higher order tensors. β and γ are very small compared to α, and often they are neglected. The polarisation can be obtained by derivative equation (2.17) with respect to the electric field:

$$\begin{aligned} P_i(\vec{E},\vec{H}) = -\frac{\partial(F)}{\partial(E_i)} = P_i^S + \epsilon_0\epsilon_{ij}E_j + \alpha_{ij}H_j + \frac{1}{2}\beta_{ijk}H_jH_k \\ +\gamma_{ijk}H_iE_j - ... \end{aligned} \tag{2.18}$$

And to the magnetisation with respect to the magnetic field:

$$M_i(\vec{E},\vec{H}) = -\frac{\partial(F)}{\partial(H_i)} = M_i^S + \mu_0\mu_{ij}H_j + \alpha_{ij}E_i + \beta_{ijk}E_iH_j + \frac{1}{2}\gamma_{ijk}E_jE_k - ... \tag{2.19}$$

ME effect where the magnetic field induces total P_I^S can be obtained by taking E=0, in equation (2.18) [52].

$$P_I^S = \alpha_{ij}H_j + \frac{1}{2}\beta_{ijk}H_jH_k \tag{2.20}$$

and the electric field induced total M_I^S, ME effect is obtained by taking H=0:

$$M_I^S = \alpha_{ij}E_i + \frac{1}{2}\gamma_{ijk}E_jE_k \tag{2.21}$$

Equations (2.20) and (2.21) are the basic equation for the dynamic ME_H and ME_E, respectively [52]. It can be seen that the linear ME effect, α_{ij} is direct cross coupling between the electric and magnetic fields and can be defined as [31]:

$$\alpha_{ij} = \left(\frac{\partial M}{\partial E}\right)_{T,H} = \left(\frac{\partial P}{\partial H}\right)_{T,E} \tag{2.22}$$

The ME response is limited by the permittivity and permeability tensors ϵ_{ij} and μ_{ij} as $\alpha_{ij}^2 < \epsilon_{ij}\mu_{ij}$ or more rigorously, $\alpha_{ij}^2 < \chi_{ij}^E\chi_{ij}^M$ where χ_{ij}^E and χ_{ij}^M are the electric and magnetic susceptibilities [31][2].

2.4.2 Magnetoelectric effect in M-type hexaferrite

Based on temperature dependences on magnetisation, Mössbauer studies and neutron diffraction studies, substituted M-type hexaferrite exhibits a non-collinear or spiral magnetic structure that induces polarisation via DM mechanism [16][8]. However, there are some discrepancies about spin magnetic structure, whether they possess longitudinal or transverse conical ordering.

Many studies have confirmed that substituted M-type hexaferrite with Sc, Sc-Mg and Co-Ti exhibit a longitudinal conical ordering along the c-axis. Neutron diffraction study of $BaSc_xMg_\delta Fe_{12-x-\delta}O_{19}$ single crystals where x=1.6 and 1.75 and $\delta = 0.05$, confirmed that the components exhibit longitudinal conical ordering up to room temperature. The addition of Mg was to reduce the conductivity by suppressing Fe^{2+} formation. The magnetic ordering of the samples can be considered as two divided blocks, R and R^*, see figure (2.14). In longitudinal conical ordering, at zero magnetic field, the spins are aligned collinearly within each block but non-collinearlly with respect to the adjacent block forming "block-type" conical magnetic structure along the c-axis. The net moment of each block will precess about the c-axis, making a half cone angle, α, and the pitch of the helix, ϕ, as defined in figure (2.14-b). They calculated α and ϕ for single crystal with x=1.8 to be 30° and 150°, respectively [14]. It should be emphasised that with longitudinal conical ordering, there is no electric polarisation. However, with the application of an external magnetic field at angle 45° with respect to the c-axis, the spin cone will be tilted away

from the c-axis and toward [100] direction and the polarisation will be induced in the direction perpendicular to H and $\vec{k}$. This is known as tilted state. In a case where H is applied along [100] direction, which is perpendicular to the direction of $k \parallel c$ axis, polarisation will be induced in the direction [120], this is known as transverse state [14][16]. From measuring magnetisation as a function of temperature, where H is applied along [100] and [001], they found that the transition temperature from ferrimagnetic state to conical spin state, T_{cone} are 270 K and 370 K for x=1.6 and x=1.75, respectively which coincides with the presence of $(00l \pm \tau)$ in neutron diffraction data, where l has odd values that arise from magnetic structure, since these reflection were forbidden by the space group of the crystal. The ME coupling was measured, after poling the sample, by integrating the polarisation current while sweeping the magnetic field to obtain p. The measurement was performed at low temperature with x=1.6 due to the low resistivity at room temperature $\sim 3 \times 10^7\,\Omega$ cm. The results show that as the applied magnetic field increases, p increases up to the maximum then decreases nearly to zero as the magnet saturates.

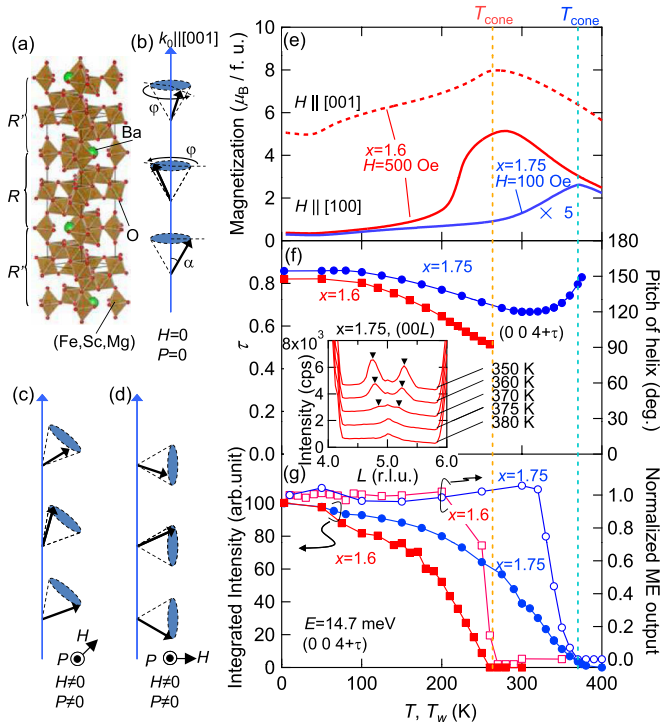

Figure 2.14: Scheme of the crystal and magnetic structure of $BaSc_xMg_\delta Fe_{12-x-\delta}O_{19}$ are shown in (a) and (b) respectively. The magnetic structure with application of a magnetic field with respect to the c-axis at, (c) 45°and (d) 90°. (e) (M-T) curves with 100 Oe and 500 Oe along and perpendicular to the c-axis. (f) the position of the magnetic superlattice reflection as a function of temperature, calculated value of ϕ. (g) integrated intensity of of the magnetic superlattice reflection and ME responses measured at 10 K [14].

At a temperature of 30 K with the application of a magnetic field $\approx$ 3 kOe , p was $\approx 15\,\mu Cm^{-2}$, whereas at T=5 K with H$\approx$ 5 kOe, p was $\approx 21\,\mu Cm^{-2}$, this is lower than one found in $BaSc_{1.5}Mg_{0.05}Fe_{10.45}O_{19}$ single crystal, where p was $\approx 305\mu Cm^{-2}$ at 4.2 K [15]. Also, p shows irreversible behaviour, once p is lost, it never recovers when the applied magnetic field is reversed to zero, even under the application of bias electric field [16].

Balbashov,*et al.*(2017) studied the electric, magnetic and ME properties of M-type hexaferrite Ba/ $SrCo_2Ti_2Fe_8O_{19}$ single crystals, where ($0.8 \leq x \leq 2$). The single crystals were grown by float zone under oxygen pressure 60-70 atm. Based on M-H measurements at 5 K and 300 K and temperature dependencies on magnetisation measurement at fixed fields, they confirmed the existence of conical spin structures for x =0.9 and 1.1 by the observation of different slopes of M-H measurements at different temperature, and the presence of the maximum in temperature dependence at fixed field, to be $T_{cone} \approx 170$ K and 280 K, respectively. ME measurements were performed on $BaCo_{0.8}Ti_{0.8}Fe_{10.4}O_{19}$ and $SrCo_{0.9}Ti_{0.9}Fe_{10.2}O_{19}$ single crystals at low temperature 2 K and 5 K respectively, due to the low resistivity in the surface of crystals at room temperature. After poling procedure, a magnetic field applied perpendicular to the direction of the c-axis, a low electric polarisation induced magnetically was observed with $p \perp H \perp c$. Since p was very small, the results were estimated only qualitatively not quantitatively [53].

Interestingly, Wang, L.,*et al.*(2012) observed converse ME effect in polycrystalline $SrCo_2Ti_2Fe_8O_{19}$ M-type hexaferrite at room temperature without magnetic bias field. From temperature dependencies of the polarisation, without application of a magnetic field, they related the sudden decreases of p with an anomaly in M(T) curve, suggesting that there is a coupling between ferroelectric and ferromagnetic orders. They suggested that the $SrCo_2Ti_2Fe_8O_{19}$ has a zero field transverse or cycloidal spiral structure which induces polarisation through the inverse DM improper ferroelectric mechanism. In addition, they highlighted the role of Co-Ti substitution and how this doping alters the magnetic structure by enhancing the non-collinear structure. This is intriguing as many studies assumed that doped M-type hexaferrite exhibits a longitudinal conical spin structure, which should not show any ME effect at zero field [11].

Mohebbi, M., *et al.*(2013) measured for the first time a magnetoelectric coupling on $SrCo_2Ti_2Fe_8O_{19}$ single crystal thin film at room temperature. The thin film was grown on sapphire substrate by Alternate Target Laser Deposition (ATLAD) technique, with 0.7 μm thickness. In their work, they measured indirect converse ME effect, which is defined as a change in magnetisation induced by the application of an electric field, E. They measured the change in remanent magnetisation to be 12.8% by applying only 1 V. The linear ME coupling coefficient, α, of (6.07×10^{-9}) sm^{-1} was deduced. In addition, they measured the change in remanent magnetisation as a function of electric field for $SrCo_2Ti_2Fe_8O_{19}$ polycrystalline sample by applying an electric field. A change in remanent magnetisation of 3% and 4% was observed with the application of a field of 12 $kVcm^{-1}$ parallel and perpendicular to direction of magnetisation, respectively. Their results show ME coupling in the thin film is stronger than the polycrystalline sample, since the result was the average of change in magnetisation along the direction of applied electrical field in each crystallite [34]. The ME effect in M-type hexaferrite was explained by introducing a "slinky helix" model, which treats hexaferrites as electrostrictive, by applying an external electric field the material strains and alters its physical structure, the Fe-O-Fe bond angles, hence this modifies the spiral spin structure inducing a change in magnetisation. They concluded that the spiral spin structure by itself is not sufficient to induce the ME effect at room temperature after unsuccessful ME measurements for $Ba/SrSc_{1.8}Fe_{10.2}O_{19}$ single phase bulk, which are characterised by longitudinal

conical spin structure. Moreover, they highlighted the role of substitution of TM ions in S block for moderating spin interactions between blocks and strain effect in ME effect [12].

Beevers, J.,*et al.*(2018) measured ME effect in $SrCo_2Ti_2Fe_8O_{19}$ thin films and highlighted the role of Co-Ti substitution on magnetic structure and the linear ME coupling of M-type hexaferrite. In their work, $SrCo_2Ti_2Fe_8O_{19}$ thin films were grown by PLD and characterised using magnetometer and soft X-ray magnetic spectroscopy. The ME effect was measured by detecting the change of magnetisation with application of a voltage at room temperature. The samples were pre-magnetised to 20 kOe then during the measurement, a small magnetic field was applied along the direction of electric field, H=400 Oe, to ensure a non-zero magnetisation. They observed that the magnetisation reduced with application of a voltage, which agrees with literature [11].

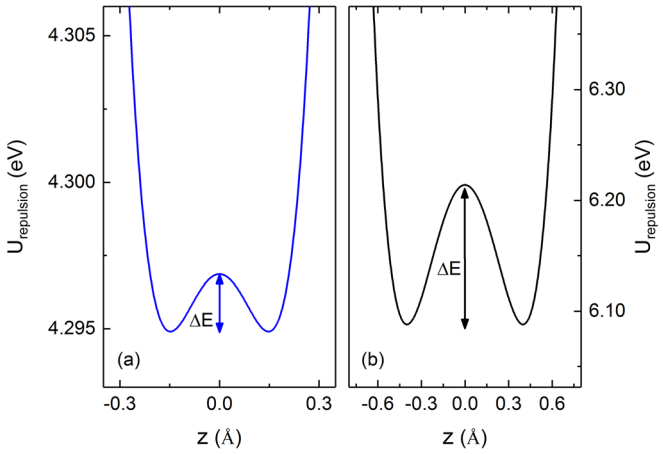

Figure 2.15: The calculated energy potential for $U_{repulsion}$ as a function of off-equatorial displacements for (a) Fe^{3+} and (b) Co^{2+} in the trigonal bi-pyramidal, 2b site, and Ti^{4+} in the octahedral, 12k site [9].

Moreover, density functional theory calculations were performed on $SrFe_{12}O_{19}$ and $SrCo_2Ti_2Fe_8O_{19}$ using CASTEP 8.0 code to understand the effect of Co-Ti substitution and their occupancy on the crystal structure. For $SrFe_{12}O_{19}$, the calculation of local potential energy for the bi-pyramidal site along the c-axis shows that the energy barrier, ΔE, is small ≈ 2 meV at room temperature which is easily overcome by thermal energy $k_BT \approx 25.7$ meV [9]. Therefore, an average equatorial potential is expected leading to a zero net polarisation. However, the result is different when Fe^{3+} ions are substituted with Co^{2+} and Ti^{4+} in the (2b) bi-pyramidal and (12k) octahedral sites, respectively. The energy barrier, ΔE, increases to 120 meV at room temperature, see figure (2.15). Hence, the Co-Ti substitution in these sites enhance the ME properties within structure [9][31].

The ME effect has also been reported in $SrFe_{12}O_{19}$ and $BaFe_{12}O_{19}$ compounds by V.Kostishyn *et al.*(2015). In their work, the compounds were prepared by solid state reaction method with the addition of 0.5-1.5 wt% of B_2O_3 during the heat treatment process in oxygen to improve the resistivity of the samples. The ME effect responses were detected by measuring the induced voltage on the sample with the application of a magnetic field at room temperature to be (0.032 ± 0.001) VA^{-1}

and (0.031 ± 0.001) VA^{-1} for $BaFe_{12}O_{19}$ and $SrFe_{12}O_{19}$, respectively. They also measured the magnetodielectric effect, which is the change of dielectric constant with application of a magnetic field, to be $(4.19 \pm 0.06\%)$ and $(4.125 \pm 0.045\%)$ for $BaFe_{12}O_{19}$ and $SrFe_{12}O_{19}$, respectively. The observation of high multiferroic proprieties were attributed to the addition of a dielectric layer B_2O_3 that impedes 180° domain walls motion on the grain boundaries of the ferrite, leading to the presence of electric polarisation, as well as the shift of Fe^{3+} from the centre of the trigonal bi-pyramidal sites [54].

G.Tan and *et al.*(2016) observed the ME response in $SrFe_{12}O_{19}$ polycrystalline samples at room temperature. They calculated the relative magnetic permeability, M_r, by measuring the capacitance as a function of the magnetic field. They found a change in dielectric constant in region 2 $kOe \leq H \leq 42$ kOe similar to $BaSc_xFe_{12-x}O_{19}$ [49].

Hence, the non-collinear magnetic structure and the displacement of TM off the centre of trigonal bi-pyramidal sites are important factors that affect or/and raise the ME effect on M-type hexaferrite at room temperature. The low resistivity of the materials especially at room temperature may screen the effect due to oxygen deficiencies. However, this can be tackled by performing a heat treatment process or adding elements such as Mg to improve the electric properties [14]. The non-collinear magnetic structure is developed depending on the amount of TM substitution and their site-specific occupancy.

Chapter 3

Experimental Methods and Analytical Techniques

This chapter gives an overview of the synthesis methods and characterisation techniques that were used in the work. General theoretical and experimental aspects are discussed. The experimental setups will be provided within the following chapters along with the experimental results and the discussions.

3.1 Synthesis Methods

In this work, three different type of M-type hexaferrite samples were prepared. The first type, polycrystalline samples were obtained using solid state reaction method. The second type, single crystals were grown using the float zone method and the last type, thin films that were grown by Pulse Laser Deposition, PLD. A brief description of the synthesis methods and instruments used to prepare these samples are discussed below.

3.1.1 Solid State Reaction method

The solid state reaction method is most commonly used to synthesise polycrystalline materials. The method involves weighing the raw materials, mixing at the level of individual particles and sintering at a high temperature, because reaction is diffusion limited. This method is relatively inexpensive and requires only simple devices these include; a ball mill and high temperature furnace. However, the resultant product may contain impurities, agglomeration and limited homogeneity. In order to obtain the desired phase, the starting materials should be pure, accurately weighed and mixed and milled to reduce particle size and increase the surface area of the reactant. The material should also be sintered at an appropriate temperature [38].

According to the phase diagram of M-type hexaferrite, $SrFe_{12}O_{19}$ melts incongruently, which means that a solid compound does not melt uniformly, in which the chemical composition of the resulting liquid is different from that of the solid. Langhof *et al.*(2009) investigated the Fe-rich part of the SrO-Fe_2O_3 system and found out that $SrFe_{12}O_{19}$ single phase is stable up to 1410 ℃ with 85.71 mol %Fe_2O_3 (Fe_2O_3/SrO=6) and decomposes at higher temperature into X and W-hexaferrites, see figure (3.1). For excess Fe_2O_3 at 87% (Fe_2O_3/SrO=6.69) sintered

at 1200 ℃ for 24 h in air, α-FeO_3 was found as second phases beside M-type hexaferrite [55][8].

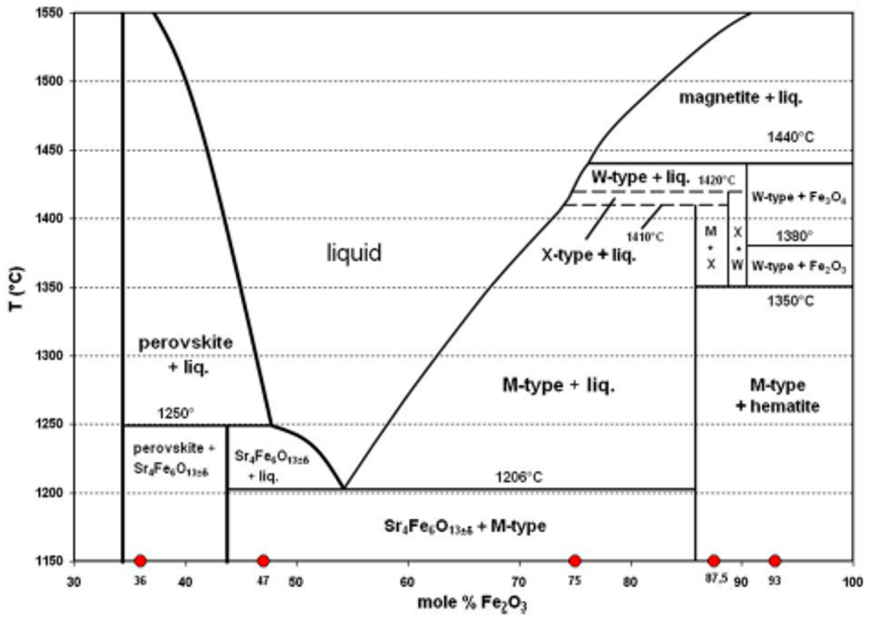

Figure 3.1: Phase diagram of the $SrO.Fe_2O_3$ system for Fe-rich part ($>$ 33 *mole* % Fe_2O_3 in air [55].

3.1.2 Float Zone method (FZ)

In the float zone method, a crystal is grown from solidification of a stoichiometric melt. The scheme of the optical float zone furnace is shown in figure (3.2). As illustrated, two sintered ceramic rods (feed and seed) are vertically mounted above each other in which their tips meet at the melting zone. Halogen lamps are used as a source of heating. The basic concept is that the IR from the halogen lamps are focused via ellipsoidal mirrors on a small area between the feed and seed rods to produce a melting zone. At a certain temperature, a molten droplet forms and floats between the end of the solid phases. Both of the rods are rotated in opposite directions around the z-axis in order to mix the liquid and distribute the temperature homogeneously within the melt. During the heating process the halogen lamp moves down the rods, the outer part of the rods crystallise at the hot zone boundary while the inner part melts at the zone [38].

These rods are usually prepared using solid state reaction method in which a correct amount of powder reactants are mixed, milled and pressed into pellets then sintered at a high temperature, as discussed above. Koohpayeh and Abell.(2008) outlined that the nature of the feed rod, growth rate, growth atmosphere, gas pressure, temperature gradient, molten zone temperature and rotation rate are crucial experimental parameters that may affect the quality of the grown single crystals [56].

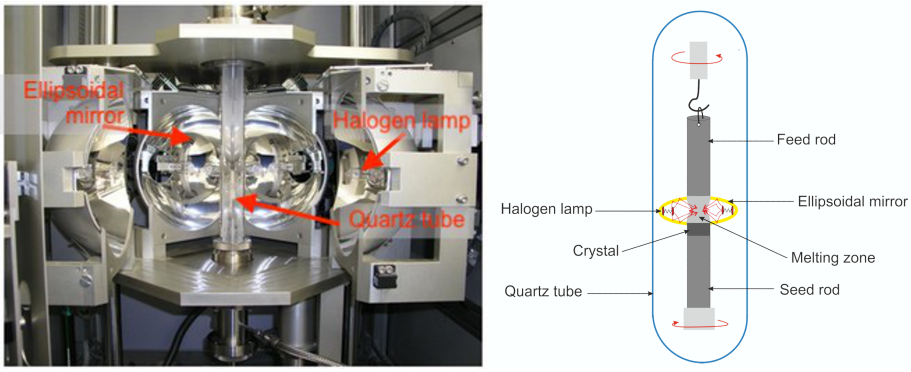

Figure 3.2: The float zone furnace at Durham University (on the left) and scheme of FZ method (on the right).

3.1.3 Pulsed Laser Deposition (PLD)

Pulsed laser deposition (PLD) is a type of physical vapor deposition technique for thin film growth. A high-power pulsed laser beam is focused onto a target material to ablate the material surface forming a "plume", as shown in figure (3.3). The plume condenses on a substrate surface forming layers of the thin film. Generally, the PLD system consists of a high-power pulsed UV laser and a growth chamber, where the growth takes place. The chamber allows for ultra-high vacuum conditions to be used or can be filled with partial pressures of gases such as oxygen and nitrogen. A vacuum pump system is used to control the background gas pressure in the chamber. The substrate is placed at a distance of 10 cm above the target and can be heated using a CO_2 laser. In order to increase homogeneity of the thin films, the substrate holder is rotated to distribute the heat and the deposited material uniformly [57].

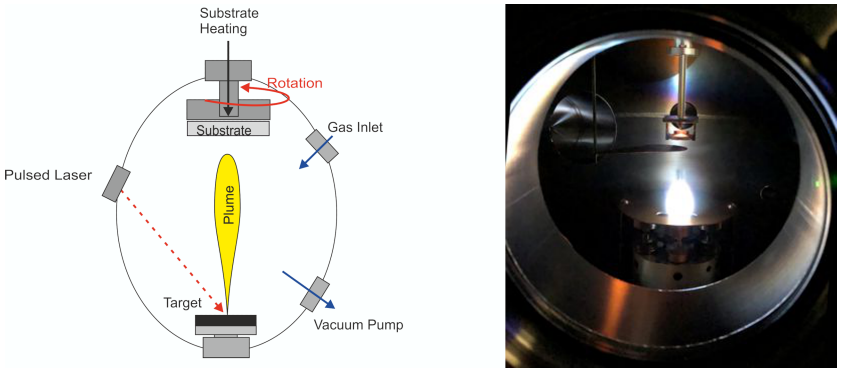

Figure 3.3: Scheme of the pulsed laser deposition (on the left). The PLD system at University of York (on the right).

There are many variables that affect the growth, such as laser pulse energy density (fluence), pulse duration, repetition rate, background gas pressure, substrate temperature, substrate-target distance as well as annealing conditions. One advantage of the PLD technique is stoichiometric transfer of complex unit cells from the target to the film. Another advantage is the ability of growth with multiple targets, as well as independent control of growth parameters and the ability to alter these during the growth [58][59].

3.2 Structural Characterisation

The structure of the samples was studied using the X-ray diffraction technique. A brief introduction of X-ray diffraction (XRD), as well as the instruments and software used for the experiments are given. Scanning electron microscope (SEM) was also used to study the element concentration of polycrystalline samples.

3.2.1 X-ray Diffraction technique

X-ray diffraction is a non-destructive analytical technique that reveals information about the crystal structure and physical properties of materials. In X-ray diffraction experiments, the intensity of the scattered wave from electrons bound to atoms is measured. When the incident X-rays interact with an atom containing Z electrons, each electron deflects part of the radiation coherently without loss of energy as described by Thomson scattering, which describes the relevant scattering amplitudes and scattering cross sections [60]. For scattering at an angle of 2θ to the incident beam as shown in figure (3.4), the phase difference between the scattered wave is given by:

$$\Delta\phi(\vec{r}) = (\vec{k'} - \vec{k}).\vec{r} = \vec{Q}.\vec{r} \tag{3.1}$$

where $\vec{k}$ and $\vec{k'}$ are the incident and scattered wavevectors, respectively. $\vec{Q}$ is the scattering vector, and from the scattering triangle $|Q| = 2|k|\sin\theta = \frac{4\pi}{\lambda}\sin\theta$.

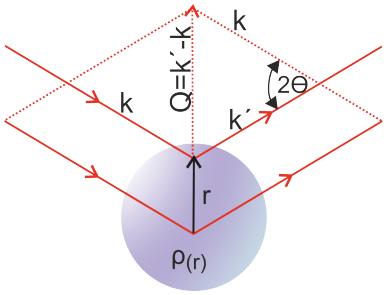

Figure 3.4: X-ray scattering of an atom. The incident wavevector $\vec{k}$ deflects by the electron distribution, $\rho(r)$ in an atom resulting the wavevector $\vec{k'}$. The scattering vector is $\vec{Q} = \vec{k'} - \vec{k}$ and the phase difference is $\vec{Q}.\vec{r}$.

The scattering length of an atom, known as the atomic form factor, $f^0(Q)$, can be calculated from the Fourier transform of the electron density in the sample as:

$$f^0(Q) = \int \rho(r)\, e^{iQ.r} dr \tag{3.2}$$

where $\rho(r)$ is the electron density and $e^{iQ.r}$ is a phase factor. The atomic scattering factor depends on the angle θ. When Q decreases to zero, all electrons scatter in phase so that $f^0(Q = 0) = Z$. On the other hand, when Q increases from zero electrons start to scatter out of phase hence $f^0(Q \to \infty) = 0$. Also the atomic form factor has a dependency on the wavelength of the incident X-ray at fixed value of θ, i.e. $Q \propto \frac{1}{\lambda}$, as shorter wavelength λ, the path differences will be larger relative to λ, resulting in more interference between scattered waves, therefore the atomic form factor will be smaller [60]. As a result, the X-ray diffraction patterns at higher angles ($2\theta < 60° - 70°$) are usually weak and the diffraction of the light atoms also

are very weak in comparison to heavy atoms [38][61][27].

It is worth emphasising that the argument above assumes the X-rays are scattering by an elastic collision from free electrons, i.e. without loss of their energy. However, X-rays can be scattered inelastically by the core electrons which are tightly bound electrons, see section (3.3.2). As result the atomic form factor can to be corrected to:

$$f(Q,\hbar\omega) = f^0(Q) + f^{'}(\hbar\omega) + if^{''}(\hbar\omega) \tag{3.3}$$

where $f^{'}$ and $f^{''}$ are anomalous corrections to f^0. $f^{'}$ and $f^{''}$ are function of the photon energy and independent on Q [62][60]. Ignoring inelastic scattering, the structure factor, F(Q), can be defined as the sum over all atoms j in the unit cell, given by:

$$F(Q) = \sum_j f_j(Q)\, e^{iQ.r_j} \tag{3.4}$$

The intensity of the scattered wave is proportional to the structure factor F(Q), given by:

$$I(Q) \propto F(Q)F^*(Q) = |F(Q)|^2 \tag{3.5}$$

The structure factor for a crystal is given by:

$$F^{crys}(Q) = \overbrace{\sum_j f_j(Q)\, e^{iQ.r_j}}^{\text{Unit cell structure factor}} \quad \overbrace{\sum_n e^{iQ.R_n}}^{\text{Lattice sum}} \tag{3.6}$$

The first term represents the unit cell structure factor and the second term is the sum over lattice sites, where R_n are the lattice vectors in real space, which can be written as $R_n = n_1a_1 + n_2a_2 + n_3a_3$. (a_1, a_2, a_3) are the basis vectors of the lattice and (n_1, n_2, n_3) are integers. The lattice sum in equation (3.6) is of order unity, except when the scattering vector is equal to:

$$Q.R_n = 2\pi \times \text{integer} \tag{3.7}$$

The scattering possibilities of a given crystal can be represented by a reciprocal lattice basis vectors, b_j, that can be defined for every real space lattice a_i by:

$$b_1 = 2\pi\frac{a_2 \times a_3}{a_1.(a_2 \times a_3)}, \quad b_2 = 2\pi\frac{a_3 \times a_1}{a_1.(a_2 \times a_3)}, \quad b_3 = 2\pi\frac{a_1 \times a_2}{a_1.(a_2 \times a_3)} \tag{3.8}$$

From the reciprocal lattice properties,

$$a_i.b_j = 2\pi\delta_{ij} \qquad \text{where} \quad \delta_{ij} = \begin{cases} 0 & i \neq j \\ 1 & i = j \end{cases} \tag{3.9}$$

δ_{ij} is the Kroenecker delta. Therefore, any lattice site in the reciprocal lattice is given by:

$$\vec{G} = h\, b_1 + k\, b_2 + l\, b_3 \tag{3.10}$$

where h, k and l are integers, known as Miller index that are obtained by taking the reciprocals of the fractional intercepts of the lattice constants a_1, a_2 and a_3,

respectively. Multiplying the reciprocal lattice vectors G, with the real lattice vectors R_n, results in:

$$\vec{G}.R_n = 2\pi(hn_1 + kn_2 + ln_3) = 2\pi \times \text{integer} \tag{3.11}$$

Hence, from equations (3.7) and (3.10), the diffraction condition is:

$$\vec{Q} = \vec{G}$$

Known as Laue condition which is equivalent to the Bragg's law. Bragg's law describes the essential conditions of diffraction. As shown in figure (3.5), diffraction occurs when a wavelength comparable to atomic spacing is scattered by atoms that arrange periodically producing constructive interference at specific angles, expressed as:

$$n\lambda = 2d\sin\theta \tag{3.12}$$

where n is integral number representing the order of reflection, λ is wavelength of the incident beam, d is the distance between adjacent planes and θ is the angle of the incident wave. The diffraction peak is only observed from constructive interference of waves, when X-rays scattered by parallel planes of atoms that are normal to the diffraction vector, Q, the vector that bisects the angle between incident and scattered beam, as shown in figure (3.5), and the difference in path length is one wavelength i.e in phase.

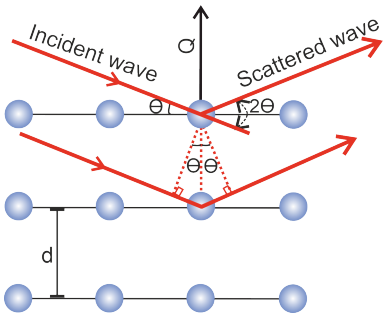

Figure 3.5: Scheme of Bragg's law.

The diffraction peak position gives the d-spacing as calculated by Bragg's law, which refers to the size and shape of the unit cell whereas the diffraction peak intensity describes the contents of the unit cell and the atoms arrangement within the crystal. Bragg law results from the periodicity of the lattice planes separated by a distance d. The d-spacing can be calculated for a particular crystal system, for a hexagonal system [63][27][61]:

$$\frac{1}{d^2} = \frac{4}{3}\left(\frac{h^2 + hk + k^2}{a^2}\right) + \frac{l^2}{c^2} \tag{3.13}$$

where h, k and l are Miller indices of (hkl) plane. a and c are the lattice constants of the hexagonal system, which can be determined by combining and rearranging equations (3.12) and (3.13) producing:

$$\sin^2\theta = \frac{\lambda^2}{3}\left(\frac{h^2 + hk + k^2}{a^2}\right) + \left(\frac{\lambda l}{2c}\right)^2 \tag{3.14}$$

For (0 0 l) planes, becomes:

$$\sin^2\theta = \left(\frac{\lambda l}{2c}\right)^2 \tag{3.15}$$

Equation (3.15) can be considered as a linear equation, therefore, by plotting $\sin^2\theta$ versus l^2 and fitting the data to a straight line, the value of c-lattice parameter can be obtained from the slope. Hence, once the value of c-lattice constant is known, by substituting the value into equation (3.14), the value of a-lattice constant can be easily determined from the θ values of the other reflections [31].

X-ray diffraction is an useful tool to study crystal structure and atomic arrangement. Most X-ray diffractometers are composed of five essential parts; X-ray source, incident optical system, goniometer, receiving optical system and detector. X-rays are generated by an x-ray tube; a high vacuum tube that pass electrical current from a cathode to an anode. By applying electric current to heat a tungsten filament (cathode), the heat energy expels some of the electrons in a process known as thermionic emission. The electrons will accelerate under high voltage and collide into a target (anode) producing X-ray radiation at a characteristic λ for the metal target via the photoelectric effect [27], as shown in figure (3.6).

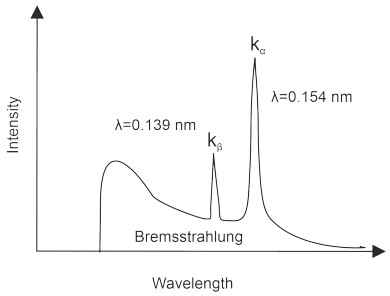

Figure 3.6: The spectrum from an X-ray tube.

In this work, thin films and single crystals were characterised using Rigaku SmartLab diffractometer. The X-ray source is a copper rotating anode producing Cu k_α. A Ge(220) double bounce monochromator was used, mounted between the X-ray tube and the sample. To remove the strip Cu k_{α_2} lines to allow just a Cu k_{α_1} lines with wavelength of 1.54059 Å. A 2 mm incident slit was used to limit divergence of the X-ray beam and parallel beam optics were used to refocus the beam into a parallel path. To enhance the resolution of the diffracted beam 1 mm receiving slits were used. The diffracted beam from the sample was detected with Scintillation counter (SC)-D(0) and Hypix-3000(1D) detectors. The scheme of optical systems used in the measurements is shown figure (3.7). The software contains tasks of package measurements and each package has steps depending on the purpose of the measurement. All packages have in common two essential steps, the first step is optic alignment. Before performing a measurement or changing a part of the optical system, it is recommended to run optic alignment for the part to correct any offset. The alignment starts with driving each axis to set default positions, before performing several scans for ω, z and 2θ to the peak position with different values of width slits to optimise and correct any offset. The second step is sample alignment with respect to direct beam half cut and surface normal alignments. Generally, the

sample height is optimised with respect to the incident and received X-ray beam on the sample surface, in which the intensity is equal to half of the maximum intensity as well as removing ω offset to ensure the surface is parallel with X-ray beam when $\omega = 0°$.

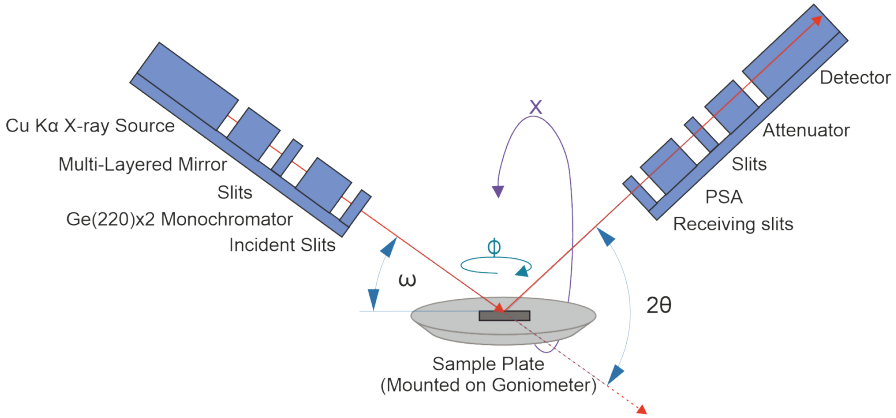

Figure 3.7: Scheme of the XRD optical systems Rigaku SmartLab diffractometer.

$(2\theta - \omega)$ measurements were performed to determine the crystal structure and unit cell lattice of the samples. In this measurement scheme both the incident angle, ω and the detector at 2θ were simultaneously moved while the sample position was fixed. The detector records the number of diffracted X-ray at each angle 2θ as a count per second. By plotting the X-ray intensity as a function of the angle 2θ, the resulting pattern displays peaks that are attributed to scattering from specific crystal planes that are normal to the diffraction vector. These planes can be identified using Miller indices (hkl). In this work, all peaks are assigned using predicted values from INDX software [64]. The input value for lattice constants were taken from reference [8].

Rocking curve measurements, also known as ω-scan, were performed to asses the quality of thin films. In this measurement, both the detector and sample positions were fixed while the incident angle ω was scanned. The detector was set and fixed at an angle of the reflection of interest, then a ω scan was performed. The resulting plot of intensity as a function of ω displays a peak. The Full-Width-at Half-Maximum (FWHM) of the peak is used to evaluate the degree of mosaicity of thin films. The smaller the value of FWHM, the better the individual crystallites are aligned [65].

The combination of both $(2\theta - \omega)$ and ω-scans results in Reciprocal Space Maps (RSM). RSM can provide additional information on crystal structure such as peak displacement and peak broadening due to strain or lattice relaxation and tilting. Also it can be used to investigate crystal orientation relationships between a thin film and its substrate. RSM measurement starts with scanning $(2\theta - \omega + \Delta\omega)$ for -2 °$<\Delta\omega <$1.2°. This sequence is repeated to produce a two dimensional region of reciprocal space. Before the measurement, it is necessary to define the orientation of the thin film with respect to the substrate. This is can be done with aid of Diffraction space simulation software for reciprocal lattice simulation [66]. The software requires information about the crystal structure for the substrate and the thin film and their direction with respect to the X-ray beam. The software posi-

tions the goniometer correctly, to chose the reciprocal lattice point of substrate and the thin film with index (hkl) in the same line of $(2\theta - \omega)$. In this measurement Hypix-3000(1D) detector was used to reduce the acquisition time by recording the diffraction intensities within an angular range of (2θ) without scanning, hence, RSM can be obtained by performing (ω) step scan and recording (2θ) profile, simultaneously. The resulting reciprocal lattice points of the thin film and the substrate can be plotted in the 2D diffraction space coordinates system, with (q_y) vertical axis and (q_x) horizontal axis in reciprocal lattice (rlu), instead of $(2\theta$ and $\omega)$, see figure (3.8)[67]. In the case of a symmetric scan, when the angle between the crystal surface and scattering plans are zero, i.e. $\omega = \theta$, the scattering factor is fully out of plane, whereas in an asymmetrical scan, there is an offset angle between the crystal surface and scattering plane equals to $(\omega - \theta)$.

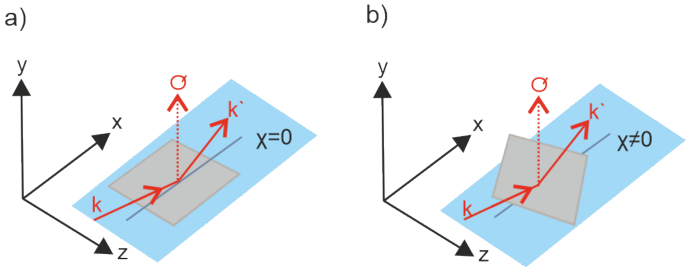

Figure 3.8: Scheme of the principle axis associated with the RSM measurement. (a) symmetric scan in which the sample is not tilted $(\chi = 0)$ and $(\omega = \theta)$. (b) asymmetric scan in which the sample is tilted $(\chi \neq 0)$ and $(\omega \neq \theta)$.

The diffraction space coordinates system of the lab can be expressed as a function of ω and 2θ as:

$$\begin{aligned} q_{\parallel} &= \frac{4\pi}{\lambda} \sin\theta \sin(\theta - \omega) \\ q_{\perp} &= \frac{2\pi}{\lambda} \sin\theta \cos(\theta - \omega) \end{aligned} \tag{3.16}$$

where $q_{\parallel}$ is the scattering vector along the beam direction (x-axis) and $q_{\perp}$ is the scattering vector out of plane along the (y-axis). q_x, q_y and q_z are in the coordinate system of the sample. q_x, q_z are the in-plane scattering vectors and q_y is the scattering vector parallel to the surface normal. If the sample is not tilted i.e. $\chi = 0$, $q_x = q_{\parallel}$, $q_y = q_{\perp}$ and $q_z = 0$. In case the sample is tilted i.e. $\chi \neq 0$, $q_{\perp}$ needs to be projected onto vectors parallel to the surface and perpendicular to it, therefore:

$$\begin{aligned} q_y &= q_{\perp} \sin\alpha \\ q_z &= q_{\perp} \cos\alpha \\ q_x &= q_{\parallel} \\ \alpha &= 90 - \chi \end{aligned} \tag{3.17}$$

a and c lattice constants can be determined using the following equation:

$$\begin{aligned} a &= \frac{1}{q_x} \frac{\lambda}{\sqrt{3}} h \\ c &= \frac{2\pi l}{q_y} \end{aligned} \tag{3.18}$$

where (q_x) and (q_y) are normalised to the incident wave vector, i.e in reciprocal lattice unit (rlu), of $(4\pi/\lambda)$.

Another measurement that gives insight to the epitaxial relationship between the thin film and its substrate is a ϕ-scan. In this measurement both the incident X-ray and the detector were fixed at particular $(2\theta - \omega)$ position for the lattice plane of interest while the sample was rotated in plane (ϕ) axis from zero to 360°. ϕ-scan can be combined with χ-scan, which is scanning along a titling angle from sample surface (out of plane). This measurement is known as Pole figure, where both $(2\theta - \omega)$ are fixed at a reflection of interest, while the sample was moving in two directions. During the scan, the sample was rotated in plane (ϕ) from zero to 360° at each out of plane tilting angle (χ) axis from zero up to 90°. The resulting plot is the diffracted intensity as a function of ϕ and χ. In this work Pole figure measurement and ϕ-scan were performed to study the crystal orientation and the degree of preferred orientation in thin films [68][67].

In Laue method, both the incident and detection angles and crystal position are fixed and only the X-ray wavelength is variable. However, during the experiment, a crystal position can be adjusted by moving and rotating the goniometer around different directions. A diffraction pattern occurs when a polychromatic (white) beam strikes a single crystal, with wavelengths, that satisfy Bragg's condition, producing spots known as Laue patterns [63].

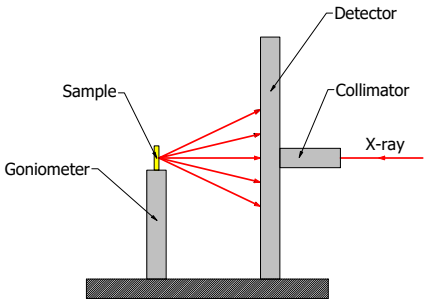

Figure 3.9: Scheme of the Back-reflection Laue camera.

There are two modes of Laue method: transmission and back reflection. In transmission mode, the crystal is placed between the X-ray source and the detector. The detector records the X-ray that are diffracted whilst travelling through the crystal. Whereas in back reflection mode, the crystal is placed behind the detector. The detector records the beams that are diffracted from the crystal in a backward direction [27]. In this work, a Real-Time-Back-reflection Laue camera system, at Durham University, was used to determine the crystal orientation for cutting the crystal perpendicular to the c-axis. The scheme of Back-reflection Laue camera is given in figure (3.9).

For polycrystalline samples, powder diffraction patterns were collected at I11-beamline High Resolution Powder Diffraction at Diamond light source, UK. The beamline produce hard X-rays with energy range (5-25) keV $(0.4 - 2.1)$ Å, the default is 15 keV$\approx$ 0.872 Å, and has a diffractometer mounted on the 2θ circle and a rotary sample stage mounted on the θ circle, see figure (3.10).

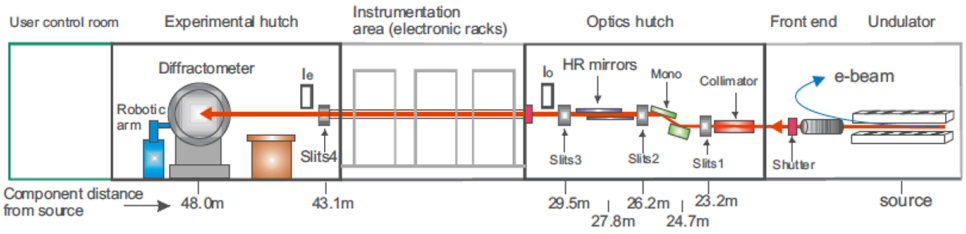

Figure 3.10: Schematic of I11-beamline showing the main components [69].

The experiments were performed in Debye-Scherrer scattering geometry, in which a parallel X-ray beam with sufficient cross section scans the sample on a capillary. The diffracted X-ray are collected by detectors that are placed on a detection circle, see figure (3.10). beam size at sample (FWHM) is $\sim 0.8\,mm(v) \times 2.5\,mm(h)$ [69]. The high resolution detector, $\Delta 2\theta = 0.005°$ at 10 keV, consists of 5 multianalysing arms known as (MAC), each arm containing 9 analysing Si crystals, in total 45 crystals, see figure (3.11). To perform full 2θ scan, each detector moves 40° with overlap between the detectors to give scan range from 3° to 150°. Constant velocity trajectory (CVT) scan mode were performed for all polycrystalline samples. In CVT mode, the total count time is specified by the user input, and the diffractometer motion trajectory is calculated to move at a constant 2θ angular speed [69][70].

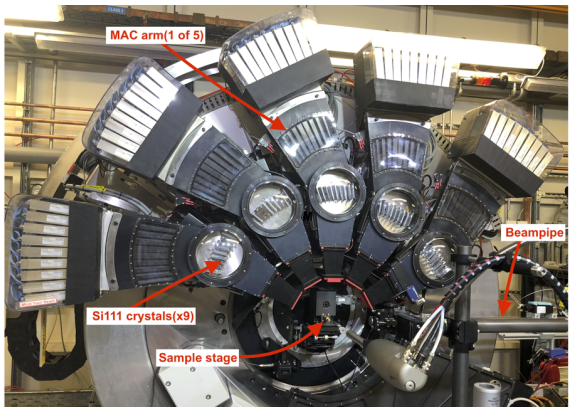

Figure 3.11: Close up of MAC detectors array I11-beamline at Diamond light source.

Rietveld Refinement method

Refinement of powder diffraction data is an essential step that can yield crystal structure of the sample and provide quantitative phase analysis. Structure refinement enables us to overcome overlap reflection issues and extract as much information as possible from the powder diffraction data. The Rietveld method is a structure refinement method that uses a whole powder pattern fitting to determine the crystal structure parameters or/and microstructural parameters such as size and strain. In this method, a theoretical or calculated structure model along side instrumental parameters are used to refine the initial calculated model in order to obtain the best possible agreement between the calculated and observed diffraction data [71][72] [73]. The calculated model contains initial values of structural parameters such as atomic position, symmetry of unit cell, occupancy and thermal parameters, that can be optimised using a Least-squares method. The Least-squares approach

is to minimise the squared sum of the difference between the observed ($y_{obs,i}$) and calculated ($y_{calc,i}$) intensities of a point i in the powder diffraction as [72]:

$$\Delta = \left(\sum_{i=1}^{N} w_i (y_{obs,i} - y_{calc,i})^2 \right) \tag{3.19}$$

where w_i is a weight of each observation point, given by:

$$w_i^{-1} = \sigma_i^2 = \sigma_{ig}^2 + \sigma_{ib}^2 \tag{3.20}$$

σ_{ig}^2 is the standard deviation associated with peak and σ_{ib}^2 is the standard deviation associated with background intensity. The value of calculated intensity ($y_{calc,i}$) can be expressed as [72]:

$$y_{calc,i} = \sum_{p} \left(S_p \sum_{s(p)} \left(|F_{calc,s,p}|^2 \Phi_{s,p,i} Corr_{s,p,i} \right) \right) + Bkg_i \tag{3.21}$$

where the outer summation is over all crystalline phases, p, and the inner summation is over all Bragg reflections s=(hkl) of a phase (p). (S_p) is a scale factor and ($F_{calc,s,p}$) is the structure factor. $\Phi_{s,p,i}$ is the reflection profile function that depends on the Bragg peak position and (Bkg_i) is the observed background intensity. ($Corr_{s,p,i}$) is a series of correction factors that depend on the scatting vector s, given by:

$$Corr(s) = M(s)LP(s)A(s)PO(s)E(s)\cdots, \tag{3.22}$$

where M(s) is multiplicity factor, LP(s) is the Lorentz-Polarisation coefficient, A(s) is an absorption correction, PO(s) is a preferred orientation corrections and E(s) is a primary extinction [72].

A typical powder diffraction pattern can be described by three components; peak position, integrated peak intensity and peak profile of Bragg reflections that result from contribution of the crystal structure of the material, the properties of the sample and the instrumental parameters. These three components can be adjustable in the Least-squares refinement with a set of structural, sample and instrumental parameters, that are listed in table (3.1). Bragg peak positions, that are a function of the wavelength and interplanar distance d-spacing, are determined by the unit cell parameters. The peak positions can be shifted due to instrumental error including misalignment of the sample or the diffractometer and axial divergence, or from the sample properties such as linear absorption or transparency and hence, correction is needed. Integrated peak intensities are determined by the structure factor for individual Bragg peaks and give information of contents of the unit cell and phase mixture [73][71].

Table 3.1: The components of the powder diffraction pattern as a function of the crystal structure, the properties of the sample and the instrumental parameters [71][72].

Pattern component	Crystal structure	Sample property	Instrumental parameter
Peak position	unit cell parameters (a , b, c, α, β, γ)	absorption/ transparency	sample alignment, zero shift, axial divergence (beam, soller)
Peak intensity	atomic position (x, y, z), displacement parameter B	preferred orientation, surface roughness, absorption/ transparency	geometry and configuration of radiation, Lorentz-polarization
Peak shape	crystallinity defects, disorder	(an)isotropic microstrain, (an)isotropic crystallite size	radiation(spectral purity), geometry, beam conditioning

There are many factors that influence peak intensities such as the atomic form factor, atomic displacement parameters and the structure factor. The structure factor, ($F_{calc,s,p}$) can be corrected using the corrections set, ($Corr_{s,p,i}$). Peak profile $\Phi_{s,p,i}$, is a mathematical convolution of three functions: the instrumental broadening, $\Omega(\theta)$, wavelength dispersion, $\Lambda(\theta)$ and the sample function, $\Psi(\theta)$ that can be expressed as [72]:

$$\Phi_{s,p,i}(\theta) = \Omega(\theta) \otimes \Lambda(\theta) \otimes \Psi(\theta) + b(\theta) \tag{3.23}$$

where $b(\theta)$ is the background function and $\otimes$ is a the convolution operation that defines between two functions, f and g as:

$$f(t) \otimes g(t) = \int_{-\infty}^{+\infty} f(\tau)g(t-\tau)d\tau = \int_{-\infty}^{+\infty} g(\tau)f(t-\tau)d\tau \tag{3.24}$$

which expresses the area of overlap between $f(\tau)$ and shifted $g(\tau)$[73][71].

The instrumental function, $\Omega(\theta)$, depends on several geometrical parameters including the position and geometry of the X-ray source, monochromator(s) and slits. The wavelength dispersion function, $\Lambda(\theta)$ is related to the finite width and nature of X-ray source and the monochromatisation technique. The sample function, $\Psi(\theta)$, depends on the physical properties of the sample such as average crystallite size, defect and strain [73][71][74].

The profile peak can be considered in two aspects; the profile shape and the peak width. The peak width profile can be determined by the full width at half maximum (FWHM), that is at half the maximum intensity, or by the integral breadth (IB) that is defined as the ratio of the peak area to the peak height. The width of peak, H, shows an angular dependence expressed by the Caglioti function as:

$$H^2 = Utan^2\theta + Vtan\theta + W \tag{3.25}$$

where U, V and W are refinable parameters. The observed peak broadening results from a contribution of the instrumental broadening, β_{instr}, and from the sample broadening, β_{sample}, due to the average crystallite size, τ, and microstrain, ϵ. Hence, the observed peak broadening can be expressed as:

$$\beta_{obs} = \beta_{instr} + \beta_{size} + \beta_{strain} \tag{3.26}$$

β_{instr} is determined experimentally with a diffraction standard or using the fundamental approach that is out of scope, more detail found in reference [72]. β_{sample} can be described by Scherrer formula:

$$\beta_{size} = FWHM^{hkl} = \frac{k\lambda}{\tau \cos\theta} \tag{3.27}$$

$$\beta_{strain} = FWHM^{hkl} = c\epsilon \tan\theta \tag{3.28}$$

β is in radians, k and c are constants. The former depends on crystallite shape, often assumed to be ≈ 0.89 and the latter depends on the type of strain, whether homogeneous or inhomogeneous strains. For inhomogeneous strain, c is ≈ 4 or 5 [74][75]. It should be noted that the instrumental broadening contribution should be corrected first in order to determine the sample broadening.

The peak shape profiles often described by a combination of Gauss and Lorentz functions, known as Pseudo-Voigt function, (PV), that can be expressed as:

$$PV = \eta L + (1-\eta)G \tag{3.29}$$

where η is mixing parameter, L and G are Lorentzian and Gaussian functions, respectively, given by:

$$L(x) = \frac{C_L^{\frac{1}{2}}}{\pi \acute{H}}\Big(1 + C_L x^2\Big) \tag{3.30}$$

$$G(x) = \frac{C_G^{\frac{1}{2}}}{\sqrt{\pi} H} exp\Big(-C_G x^2\Big)^{-1} \tag{3.31}$$

Hence, the Pseudo-Voigt function is:

$$PV(x) = \eta \frac{C_G^{\frac{1}{2}}}{\sqrt{\pi} H} exp\Big(-C_G x^2\Big) + (1-\eta)\frac{C_L^{\frac{1}{2}}}{\pi H}\Big(1 + C_L x^2\Big)^{-1} \tag{3.32}$$

where H and $\acute{H}$ are FWHM of Gaussian and Lorentzian functions, respectively. $x = (\frac{2\theta_i - 2\theta_k}{H_k})$ is the the Bragg angle of the i^{th} point in the powder diffraction pattern with its origin (calculated Bragg angle) in the position of the k^{th} peak divided by the peak's FWHM. C_G= 4ln2, $C_G^{\frac{1}{2}}/\sqrt{\pi}H$ and C_L= 4, $C_L^{\frac{1}{2}}/\pi\acute{H}$ are the normalisation factor for the the Gaussian and Lorentzian functions, respectively [73].

Generally, the observed diffraction pattern consists of Bragg reflection (signal), background and noise, see figure (3.12). The observed background in diffraction pattern is resulting from inelastic scattering, scattering from air, sample holder, x-fluorescence and detector noise [72][73]. Thus, the observed background can be processed by linear interpolation between selected points and then by subtracting the baseline, or by adding its contribution to the calculated intensity, $(y_{calc,i})$, during profile fitting. The latter method models the background using an analytical or empirical function with coefficients that are refinable during the fitting. The calculated background is then added to the value of calculated intensity as a function of Bragg

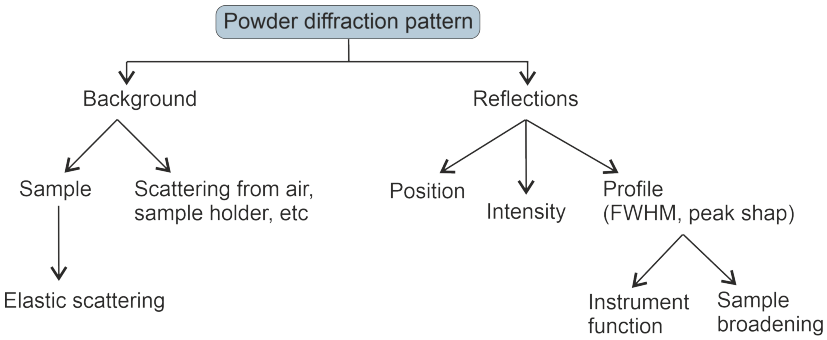

Figure 3.12: Scheme of information content of a powder diffraction pattern.

angle [72][73][76]. Chebyshev polynomial of the first kind is commonly used to fit background, represented as a function of x_i:

$$x_i = \frac{2(2\theta_i) - (2\theta_{max} + 2\theta_{min})}{2\theta_{max} - 2\theta_{min}} \tag{3.33}$$

where $2\theta_{max}$ and $2\theta_{min}$ are the maximum and the minimum Bragg angles in the diffraction pattern. The background value is calculated as:

$$Bkg_i = \sum_{k=0}^{n} c_k T_k(x_i) \tag{3.34}$$

where c_k are polynomial coefficients, their values are determined by Least-squares during the refinement and T_k is the Chebyshev functions that are defined as [77]:

$$\begin{aligned} T_o(x) &= 1 \\ T_1(x) &= x \\ T_{n+1}(x) &= 2xT_n(x) - T_{n-1}(x) \end{aligned} \tag{3.35}$$

To sum up, the parameters, that are usually refined, in the Rietveld method are listed bellow [74]:

- Background parameters, typically 5-15 coefficients [72]
- Instrumental parameters; zero shift, sample displacement, peak shape (U, V, W and asymmetry) parameters
- Sample parameters; unit cell parameters (a, b, c, α, β and γ), fractional atomic coordinates (x, y and z), site occupation factor, displacement parameter, linear absorption coefficient/transparency, preferred orientation, surface roughness, (an)isotropic crystallite size, (an)isotropic microstrain, scale factor for each phase and overall scale factor

The refinement of many parameters simultaneously, should be avoided, as it leads to unstable refinement or divergence [72][73].

The quality of refinement, known as figure of merit, which measures the agreement between observed diffraction data and calculated model can be estimated by several residual functions; the profile, R_p, the weighted profile, R_{wp}, expected, R_{exp},

and goodness of fit, χ^2 [72]. The profile R-value, which is the difference between the observed and calculated profile, given by:

$$R_p = \frac{\sum_{i=1}^{N} |y_{obs,i} - y_{calc,i}|}{\sum_{i=1}^{N} y_{obs,i}} \tag{3.36}$$

The R-value above does not take into account the weight scheme, therefore, R_p is overemphasized by strong reflections [72]. To overcome this problem, the weight scheme is applied to the weighted profile R-value, given by:

$$R_{wp} = \sqrt{\frac{\sum_{i=1}^{N} w_i(y_{obs,i} - y_{calc,i})^2}{\sum_{i=1}^{N} w_i(y_{obs,i})^2}} = \sqrt{\frac{\Delta}{\sum_{i=1}^{N} w_i(y_{obs,i})^2}} \tag{3.37}$$

The expected R-value, which reflects the quality of the data, is given by:

$$R_{exp} = \sqrt{\frac{N - P}{\sum_{i=1}^{N} w_i(y_{obs,i})^2}} \tag{3.38}$$

where N and P are the number of data points and the number of parameters, respectively. It is noteworthy to mention that the R-values above include a contribution from background. Therefore, the method of background processing may give different R-values. For example, if the background has been subtracted prior to refinement, $(y_{obs,i})$ is the net intensity after background correction, but if the background is refined, its contribution adds to $(y_{calc,i})$ and $(y_{obs,i})$. Moreover, if a background is high, a lower weighted R-value is obtained. However, subtracting the background from the observed step scan intensities in the denominator could overcome this problem [72][76][73]. The corrected R-value, $\acute{R}_p$, weighted R-value, $\acute{R_{wp}}$ and expected R-value, $\acute{R_{exp}}$ are given by:

$$\acute{R}_p = \frac{\sum_{i=1}^{N} |y_{obs,i} - y_{calc,i}|}{\sum_{i=1}^{N} |y_{obs,i} - Bkg_i|} \tag{3.39}$$

$$\acute{R_{wp}} = \sqrt{\frac{\sum_{i=1}^{N} w_i(y_{obs,i} - y_{calc,i})^2}{\sum_{i=1}^{N} w_i(y_{obs,i} - Bkg_i)^2}} \tag{3.40}$$

$$\acute{R_{exp}} = \sqrt{\frac{N - P}{\sum_{i=1}^{N} w_i(y_{obs,i} - Bkg_i)^2}} \tag{3.41}$$

The goodness of fit, which is the ratio between the weighted profile R-value and the expected R-value, is given by:

$$\chi^2 = \left[\frac{R_{wp}}{R_{exp}}\right]^2 = \frac{\sum_{i=1}^{N} w_i(y_{obs,i} - y_{calc,i})^2}{N - P} \tag{3.42}$$

Ideally the value of χ^2 is unity [72]. However, it should be noted that there is no threshold or accepted value of R-factors which indicate a good or reliable refinement since these R-values are the result of several contributions (the fitting calculated model to observed intensities, the background, the peak positions and peak shapes) and how well they fit. Also, the R-values are affected by the quality of data. For

example, for a given model with a certain imperfection, the lower the resolution of the data, the closer χ^2 to unity [78]. By improving the resolution of data, i.e. increasing the total number of counts collected for a observed pattern to reduce the statistical uncertainty, R_{exp} decreases, the difference between R_{exp} and R_{wp} increases, thus χ^2 increases [79]. Hence, it is important to view the observed, calculated and the difference between them graphically, this helps to judge the quality of the refinement [78].

3.2.2 Scanning Electron Microscopy and Energy Dispersive X-ray analysis

Scanning Electron Microscopy (SEM) is a versatile tool that uses an electron beam to scan a sample surface producing images that contain information about morphology, surface topography and composition of the sample over a wide range of magnification. SEM resolution is typically around ≈ 0.5 nm [80]. The SEM mainly consists of five parts, an electron gun, condenser, objective lenses, specimen chamber and detectors, see figure (3.13).

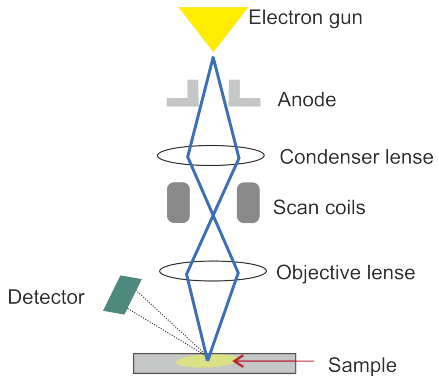

Figure 3.13: Scheme of the basic components of SEM.

The electron gun emits a beam of electrons that are focused by one or more of the objective lenses to a few nanometres beam size. This focused beam is scanned across the sample in a raster pattern. When the incident electron beam interacts with the sample surface, several scattering process may occur including Secondary Electrons (SE), these are generated from inelastic scattering of the incident electrons within the sample, and Back Scattered Electrons (BS), that are originated from elastic scattering of the incident electrons within the sample. Since the energy of SE is small, SE are sensitive to the sample surface. BS, have higher energy than the SE and so, are sensitive to the sample composition [81].

Energy Dispersive X-ray analysis (EDX) is a powerful technique that is used to identify the chemical composition of a sample. EDX spectrum is obtained from detecting the X-rays emitted from the sample due to inelastic scattering electrons. When the incident beam excites core electrons from an atom leaving holes, higher energy electrons , from higher orbitals, fill the holes left and release energies that are equivalent to the difference of the atomic energy levels depending on the atomic number of the atom. Therefore, the energy of emitted X-rays can be used to identify the chemical composition and the elements present within the sample [81][82].

3.3 Magnetic Characterisation

In this project, the magnetic properties of the samples were determined using Quantum Design MPMS3 (SQUID-VSM) magnetometer. In addition, X-ray absorption spectra at the iron, cobalt and titanium $L_{2,3}$ edges for M-type hexaferrite thin films were obtained at I06-beamline Diamond light source, UK. A brief description of these instruments and analysis methods are discussed below.

3.3.1 The Superconducting Quantum Interference Device

The superconducting quantum interference device (SQUID) is used to determine magnetic properties of materials. As shown in figure (3.14), a SQUID magnetometer consists of a SQUID sensor; a superconducting ring with a thin insulating layer known as Josephson junction. The SQUID sensor is attached to metal pickup coils placed inside the sample tube. The SQUID system also comprises; a cryogenic probe with a temperature control system that is used for low temperature measurements down to 4 K and provides refrigeration for the superconducting sensor and magnet; a gas controller system which provides gas flow control for temperature regulation and cleaning procedures; and a magnet control system which provides a magnetic field up to (±7) T along the z-direction [23][83]. The sample is driven through the coils via a linear motor transport unit. The sensitivity of this device is $\leq 10^{-8}$ emu. It is based on flux quantisation in closed superconducting loop and Josephson effect that occurs between two superconducting materials separated by a thin insulating layer experiencing tunneling of Cooper pairs of electrons through the junction. When a sample is moved slowly through pickup coils, a change in magnetic flux passing through the ring will induce a change in the pickup coil voltage that can be detected by the SQUID sensor. The device measures very small changes in the flux.

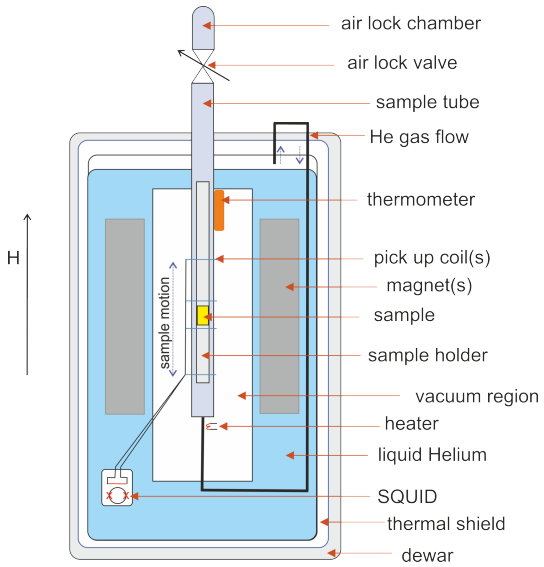

Figure 3.14: Scheme of the basic components of SQUID. The gas and temperature control systems are not shown.

In SQUID-VSM mode, the sample is vibrated at a constant frequency, resulting in a change in magnetic flux through the pickup coils that can be detected by SQUID sensor. In this project, the magnetisation as a function of magnetic field

M(H) and temperature M(T) are determined for all samples using Quantum Design MPMS3 (SQUID-VSM) magnetometer, at Diamond light source and ISIS Neutron and Muon source, UK.

M-H measurement shows the variation of magnetisation, M, with the applied field, H. For a ferromagnetic or ferrimagnetic material, a hysteresis loop is observed due to a change in the magnetic domain structure via domain wall motion and or domain rotation, imperfections such as dislocations or impurity elements in the metal, see figure (3.15). The measurement starts by magnetising the sample to achieve a saturation state. When a demagnetised sample is placed in a low applied magnetic field, the domains that are in the direction of field starts to grow, by motion of the domain walls. As the field increases, the magnetisation increases by domain wall motion and/ or rotation of the spins in regions which are not collinear with field until the saturation state, point A, where all spins are aligned with the field. As the field reduces down to zero, the magnetisation reduces to the remanent magnetisation, point B. Applying field in the negative x-direction to point C will reduce the magnetisation of the sample to zero, known as coercivity field $-H_c$. Increasing the field further to point D, the sample reaches a saturation state $-M_s$. By removing the field, the remanent magnetisation is obtained $-M_r$, at point E [24][23][84].

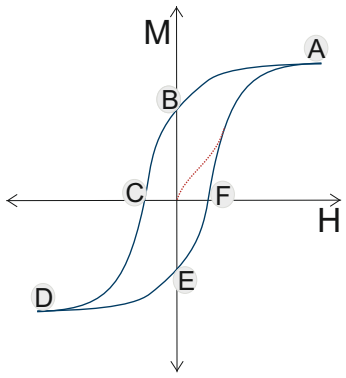

Figure 3.15: Scheme of a typical hysteresis loop. The red curve is the initial curve, A and D points are the saturation magnetisation for +H and -H, respectively. B and E points are the remanent magnetisation for +H and -H, respectively. C and F points are the coercivity field for +H and -H, respectively.

The hysteresis loop represents the bulk magnetisation of a sample. Several magnetic properties of the material can be determined from the loop including the saturation magnetisation, M_s, the remanent magnetisation, M_r, coercivity field, $-H_c$, hysteresis loss that can be calculated from the area inside the hysteresis loop, and permeability, μ, which is a measure of the material response to the magnetic field [84][23]. The permeability is defined as:

$$\mu = \frac{B}{H} \tag{3.43}$$

where B and H are the magnetic induction and the magnetic field, respectively. Since the relationship between them depends on the type of material or medium, it

is useful instead to use the relative permeability, μ_r, given by:

$$\mu_r = \frac{\mu}{\mu_0} \tag{3.44}$$

where μ_0 is the permeability of free space $\mu_0 = 4\pi \times 10^{-7}\ Hm^{-1}$. The relative permeability is related to susceptibility, χ, in SI units as:

$$\mu_r = \chi + 1 \tag{3.45}$$

where $\chi = \frac{M}{H}$.

The hysteresis loop of ferromagnetic or ferrimagnetic materials can be classified as soft or hard magnets depending on the coercivity. A soft magnet exhibits a narrow hysteresis loop and a high permeability. Soft magnetic materials are used in electromagnets, motors and transformers. On the other hand, a hard magnet shows a wide hysteresis loop that requires a large field to demagnetise, a small permeability and a large remanent magnetisation. Hard magnetic materials are used as permanent magnets, magnetic recording and electric motors [30][84].

In a high field region, where the domain rotation is predominant, the magnetisation changes slightly with the applied field, and the magnetisation behaviour can be modeled by the law of approach to saturation [19][23][84], given by:

$$M(H) = M_s\left(1 - \frac{A}{H} - \frac{B}{H^2}\right) + \chi_d\, H \tag{3.46}$$

where M_s is the saturation magnetisation, A and B are constants that are determined from fitting the equation. χ_d is the high field differential susceptibility that arises from the contribution of non-collinear spins [85]. The term (χ_d H) represents the "field-induced" increase in spontaneous magnetisation, and is usually small at temperatures well below T_c and is often neglected. The term (A/H) is related to the existence of inhomogeneities in the microcrystal which reduces the mobility of magnetisation. This term should be vanish at high field in order to saturate the sample. The term (B/H^2) is related to the magnetocrystalline anisotropy. For an uniaxial hexagonal system with $K_2 \ll K_1$ [86]:

$$B = \frac{H_a^2}{15} \tag{3.47}$$

where H_a is the anistropy field with $H_a = 2K_1/M_s$, and K_1 is the first anisotropy constant. From equation (3.46), by plotting the magnetisation against $1/H^2$ in the high region and extrapolating the straight line, the saturation magnetisation, which is the value of the intercepts, and the the anistropy field are obtained . This analysis is only applicable for single domain particles, in which there are no domain walls and when the exchange interactions between particles is excluded [87][85][19].

M(T) measurements show the variation of magnetisation with temperature and gives insight of phase transitions in the magnetic structure. The measurement can be performed under Zero Field Cooling (ZFC), or Field Cooling (FC). In ZFC mode, the sample is cooled down to a temperature T_i in zero field, where the spins are randomly orientated. At T_i, a weak magnetic field is applied, H_m, then the temperature is

increased to T_f and the magnetisation measured every 0.5 K. On the other hand, FC mode cools the sample with application of a high field, where spins are more likely to be aligned in the direction of the field, until T_i, The cooling field is removed and a bias field is applied, H_m. The temperature is increased to T_f and the magnetisation measured. Therefore, the resultant M(T) curves are different and give information on anistropy energy, spin glass transitions and the particle size distribution for nanoparticles [32][31].

3.3.2 X-ray Magnetic Circular Dichroism (XMCD)

X-ray Absorption Spectroscopy (XAS)

X-ray absorption spectroscopy (XAS) is the measurement of electron transitions from core states to unoccupied states above Fermi level. It is a versatile tool to study electronic and the magnetic properties of materials. XAS is an element specific method which is obtained by tuning the X-ray energy to correspond to the binding energy of core state for the element of interest [60]. The incident X-ray is absorbed by an atom in which the X-ray excites a core electron into unoccupied state above Fermi level, by photoelectric absorption, see figure (3.16).

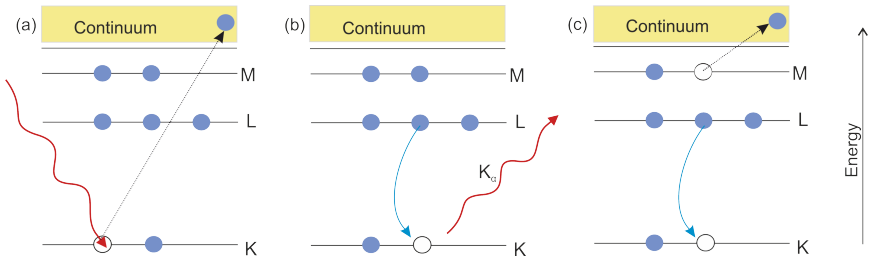

Figure 3.16: Scheme of the energy levels diagram of an atom. (a) The photoelectric absorption process, (b) The fluorescent X-ray emission, and (c) The Auger electron emission.

X-ray emission (fluorescence) occurs when an electron from the outer shell fills a core hole in the inner shell producing a photon with an energy equal to the difference between the shells. Alternatively, an electron is emitted via secondary electron emission, when an electron from the outer shell fills a hole in the inner shell emitting an electron, known as the Auger effect. The excited atom remains in an excited state with "a core hole" with lifetime for $\simeq 10^{-15}$ s before it decays by radiant and non-radiant processes [88]. XAS measures the X-ray absorption coefficient as a function of X-ray energy and can be measured in a transmission geometry, according to:

$$\begin{aligned} I_t &= I_0\, e^{-\mu t} \\ \mu t &= \ln \frac{I_t}{I_0} \end{aligned} \tag{3.48}$$

where I_0 and I_t are the incident and transmitted intensities, respectively, t is the thickness of the sample and μ is absorption coefficient, which depends on the sample density, ρ, the atomic number, Z, atomic mass, A, and the X-ray energy, E, ($\mu \approx \frac{\rho Z^4}{AE^3}$)[60].

XAS spectra are distinguished by sharp rises in X-ray absorption, called absorption edges which correspond to characteristic core level transition energies of the atom. Each absorption edge describes an electron transition from a specific orbital, K(n=1), L(n=2), M(n=3), $\cdots$, where n is the principle quantum number. For example, K-edge is resulting from the 1s-np transition, whereas the $L_{2,3}$ edges are from $2p-3d$ transitions. The core level energy increases with increasing the edge ranging from 7112 eV for Fe K-edge, to 844.6, 719.9 and 706.8 eV for Fe L_1, L_2 and L_3 edges, respectively [89]. The total intensity of the spectrum refers to the number of unoccupied states in the initial state whereas the spectral shape refers to the density of states for the core-hole state [90].

For circularly polarised X-rays, the electric field of an electromagnetic wave rotates in a helical pattern around the direction of propagation wave, $\vec{k}$. The direction of electric field rotation with respect of $\vec{k}$, can be either clockwise, which refers to right circularly polarised (RCP) or anti-clockwise for left circularly polarised (LCP). The difference between two absorption spectra measured with circularly polarised X-rays for a magnetic sample is called X-ray magnetic circular dichroism (XMC), i.e.(LCP)-(RCP) spectra. The resultant spectrum provides information about the individual contribution of the spin and orbital part on magnetic moments. XMCD signal can be explained using the atomic single electron model as the starting point, in which it describes the electronic transition from the core state to the valance state. The probability of a transition to occur is described by Fermi's Golden rule [91][60]:

$$P_{i\longrightarrow f} = \frac{2\pi}{\hbar}|\langle f|T|i\rangle|^2\rho(E_f)\delta(E_f - E_i - \hbar w) \tag{3.49}$$

where T is the transition operator (light-matter interaction) which can be written as ($T = \vec{p}.\hat{\epsilon}\, e^{i(\vec{k}.\vec{r})}$) in which $\vec{p} = -i\hbar\bigtriangledown$. $|i\rangle$ and $|f\rangle$ are the initial and final states, respectively. $\rho(E_f)$ is the density of states of the final state and δ is a Dirac delta function for the conservation of energy, given by:

$$\delta(x) = \begin{cases} 1 & x = 0 \\ 0 & x \neq 0 \end{cases} \tag{3.50}$$

The transition process is governed by dipole selection rules, allowing certain transitions with restrictions such as the change in total angular momentum, Δj can be zero or ± 1 (except $j = 0 \iff j = 0$ transition is not allowed), the change in orbital angular momentum, $\Delta l = \pm 1$ (except $l = 0 \iff l = 0$ transition is not allowed). The change of spin angular momentum, Δs is zero. The selection rules for polarised light are [92]:

$$\Delta j = 0, \pm 1, \quad \Delta l = \pm 1, \quad \Delta s = 0, \quad \Delta m = \begin{cases} +1 & \text{RCP photons} \\ -1 & \text{LCP photons} \\ 0 & \text{Linearly polarised} \end{cases} \tag{3.51}$$

where Δm is the difference in magnetic quantum number m, which refers to the projection of L vector on the z-axis defined by the field, and has value of $(m = -l, \cdots, l)$. To understand how the XMCD is generated, let us consider first a system that contains a Co^{2+} ion that has electron configuration $1s^2/2s^22p^6/3s^23p^63d^7$, with 7

unoccupied state in d-orbital. These states are all degenerate under the influence of spin-orbit coupling into a four-fold degenerate level, this does not take into account to the crystal field splitting. According to the Hund's rules, the total spin and orbital moments are $S = \frac{3}{2}$ and $L = 3$, respectively. The total angular moments $J = |L - S|, \ldots, |L + S| = \frac{9}{2}, \ldots, \frac{3}{2}$. By applying a magnetic field, these energy levels can be split up further into several non-degenerate energy levels with different energies, known as fine structure [24], see figure (3.17).

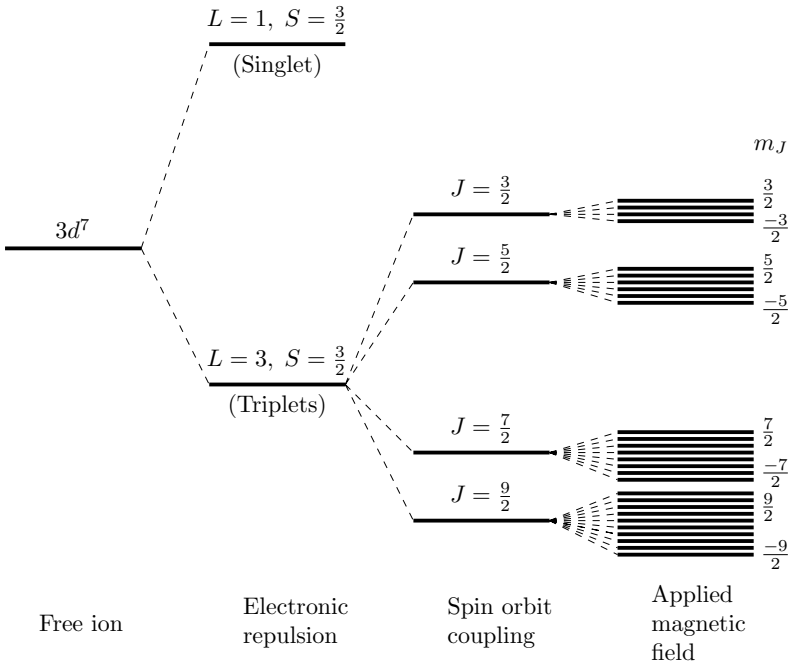

Figure 3.17: Scheme of the energy level for Co^{2+}. Note: the crystal field splitting is not taken into account in this diagram.

The principle of XMCD can be described as a two-step process, see figure (3.18-a). During the first process, polarised photons excite spin polarised electrons from the split 2p-levels, due to spin-orbit coupling. When RCP (LCP) photons with spin up (spin-down) apply at the $2p_{\frac{3}{2}}$ level, electrons are preferentially excited with spin up (spin-down). The case is opposite at $2p_{\frac{1}{2}}$ state, where electrons are preferentially excited with spin down (spin up) by RCP (LCP) photons. During the second step, the spin polarised electrons occupy the empty 3d-valence states, resulting in an imbalance between the spin up and spin down electrons. When the spin-down holes are dominant, the XMCD spectrum has a net negative (L_3) and positive (L_2) peak [91].

Since photons interact only with the orbital part of the wave function, XMCD is used to obtain information about the contribution of spin and orbital part of the magnetic moments from sum rules. The sum rules relate to the integral over the XMCD signal of a given absorption edge directly to the orbital and spin moments of the ground state. According to Chen et al [88], the orbital and spin sum rules for 3d metals are:

$$m_{orb}[\mu_B/atom] = -\frac{4q(10 - n_{3d})}{r} \tag{3.52}$$

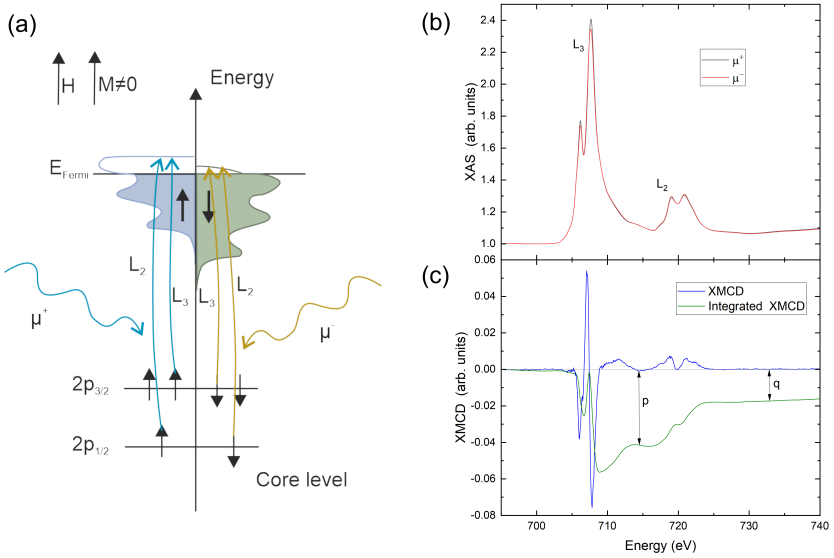

Figure 3.18: (a) Scheme of the principle of XMCD. (b) Fe XAS at $L_{2,3}$ for right (μ^+) and left (μ^-) circular polarised light. (c) XMCD spectrum (blue line) along the values of the integral p and q which appear in the sum rule (green line).

$$m_{spin}[\mu_B/atom] \equiv \frac{(6p-4q)(10-n_{3d})}{r} \tag{3.53}$$

$$\frac{m_{orb}}{m_{spin}} \equiv \frac{1}{(\frac{9}{2})(\frac{p}{q})-3} = \frac{2q}{9p-6q} \tag{3.54}$$

where n_{3d} is the number of electrons in 3d state, and q and p are shown in figure (3.18) and given by:

$$\begin{aligned} q &= \int_{L_3+L_2} (\mu^+ - \mu^-)dE \\ r &= \int_{L_3+L_2} (\mu^+ + \mu^-)dE \\ p &= \int_{L_3} (\mu^+ - \mu^-)dE \end{aligned} \tag{3.55}$$

It should be noted that the spin sum rule is only an approximation, (assuming the spin-orbit splitting in the core electrons is larger than the core-valance interaction, which is valid for Fe and Co $L_{2,3}$ edges), and not taking into account the term $\langle T_Z \rangle$; the anisotropy of the spin moment within the atom. Therefore, there is an error of a few % [88]. Equation (3.54) shows the ratio between orbital and spin moments which is related to the g-factor as [31]:

$$g = 2\left(1 + \frac{m_{orb}}{m_{spin}}\right) \tag{3.56}$$

where g≈2 for transition metals.

Experimental step for XAS experiment

XAS measurements are obtained by tuning the X-ray energy across the absorption edges. Hence, a tunable X-ray energy source is needed to perform the experiment. Synchrotron facilities offer a high intensity, tunable X-ray beam with

high stability. In this project, XAS absorption experiments were performed at I06-beamline Diamond light source, UK, to measure $L_{2,3}$ absorption edges for iron, cobalt and titanium in the hexaferrite thin film samples. More details about the experimental parameters can be found in section 6.3.2.

Diamond light source offers a high flux X-ray beam ranging from 100 eV (soft X-ray) to 35 keV (hard X-ray). Generally, the beam is generated by accelerating electrons through three phases, see figure (3.19). Firstly, an electron gun ejects a pulse of electrons in to the 30 metres long straight section (linac) from there they pass in to the 158 metre circumference booster ring where the powerful bending magnets send them on a circular path, here they are accelerated to almost the speed of light, before passing into the 562 metre circumference storage ring. Here the insertion device/undulator generates the X-ray beam. The generated X-ray beam is transferred into experimental beamlines [93]. Different undulators are installed depending on the needs of experiments. For I06-beamline, "Apple-II type" undulators with four magnetic arrays are used to tune the X-ray beam with energy ranging

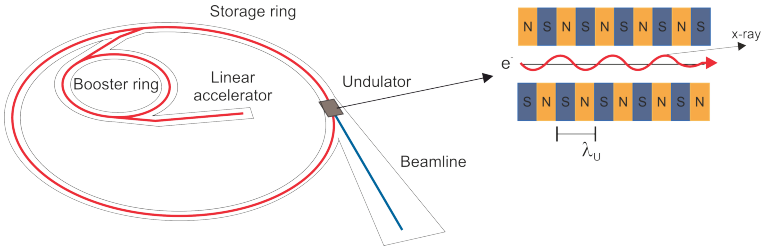

Figure 3.19: Scheme of Diamond light source layout showing the electrons path through an undulator array and the emission of X-rays.

from 106 eV to 1300 eV, as well as to polarise the X-ray beam. The energy of the beam can be varied by changing the distance "gap" between magnetic arrays whereas the polarisation can be switched by changing the phase of arrays. In addition, several mirrors and grating monochromators are utilised to reflect and focus the X-ray beam before passing to the experimental chamber, as well as to reduce unwanted wavelengths, see figure (3.20). The experimental chamber is kept under ultra high vacuum $< 10^{-9}$ mbar due to the fact that soft X-rays are easily absorbed by air. A superconducting vector magnet is installed to apply a magnetic field (max ± 6) T across the sample [91].

The XAS signal can be detected by either a Total Electron Yield (TEY) or Fluorescence Yield (FY) methods. The TEY detection mode measures the drain current as a result of photoelectron, secondary electron and Auger electron emissions. Since the total number of electrons emitted from the sample is proportional to the number of core holes created, the TEY mode is proportional to absorption coefficient, [60] as:

$$I_{TEY}(\Omega) \propto \frac{\lambda_e}{\lambda_e + \lambda_p(\Omega) sin\theta} \tag{3.57}$$

where θ is the angle of incident X-ray with respect to the surface normal, λ_e is the electron escape depth and λ_p is the X-ray perturbation length [88]. When $\lambda_e \ll \lambda_p \sin\theta$, then the total electron yield is inversely proportional to λ_p, so that the yield is proportional to the absorption coefficient. On the other hand, when

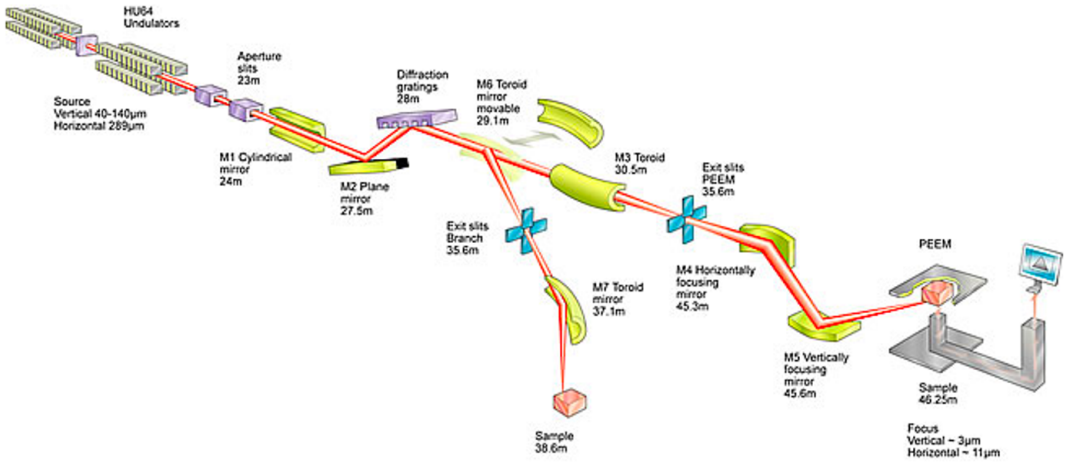

Figure 3.20: Scheme of I06-beamline at Diamond light source [93].

$\lambda_e \gg \lambda_p \sin\theta$, the absorption structure disappears. If $\lambda_e \approx \lambda_p \sin\theta$, the saturation effects occur resulting in a diminishing and broadening of the largest absorption peaks [91]. The measurement can be recorded using a drain current from the sample giving information about absorption coefficient, μ [94]. It is a surface sensitive technique and requires a conductive materiel to prevent charging effect that might modify the spectrum. Whereas in FY detection mode, the measurement is recording the number of emitted fluorescence photons. FY detection method provides bulk information, i.e. FY probes deeper than TEY methods. It should be mentioned that FY suffers from self-absorption effect, which is defined as the absorption of fluorescence photons within the sample before it reaches a detector. This causes a reduction in the measurement and correction is needed [91].

Calculation of core-level excitation in 3d TM using CTM4XAS code

Multiplet effects are used to calculate the XAS spectra based on a single electron Hamiltonian model as starting point. By taking into account electron-electron repulsion and spin orbit coupling (atomic multiplet effect), the transition of electrons from core state to valence state for a single atom can be simulated. The calculation can be improved by taking into consideration the effect of the surrounding environment on TM atom, known as the crystal field effect, see section (2.2.6).

Another modification that can be applied is the Charge Transfer effect, which is related to electrons hopping between the ligand to the 3d-orbital TM atom, therefore, the number of electrons in the 3d-orbital fluctuates. This effect adds new dipole transitions, therefore, the configuration $3d^{n+1}\underline{\mathrm{L}}$ adds to the $3d^n$ ground state, and the $3d^{n+2}\underline{\mathrm{L}}^2$ adds to the $3d^{n+1}$ final states. All these effects are available to use in CTM4XAS software [95].

To simulate XAS spectrum using atomic multiplet calculations, many input parameters have to be defined by the user. The first step is the selection of the electronic configuration system, based on that, the initial and final states are automatically loaded. The software panel allows the user to modify the Slater integral reduction, F_{dd}, F_{pd} and G_{pd}, which describe the interaction between the d-electrons, and between the core-electrons and d-electrons. The atomic parameters are calcu-

lated within the Hartree-Fock limit [95]. These parameters can have a value between 0 to 1.5, the default setting is 1 meaning 80% of Hartree-Fock values. This reduction of the atomic value accounts for the interatomic interaction and screening effect. Moreover, the software panel allows the user to control the value of 3d spin-orbit coupling, by default the value is 1. The second step is choosing the symmetry of crystal field parameters. There are four symmetries that can be calculated, Octahedral (O_h), tetragonal(D_{4h}), trigonal distortion (C_{3i}) and four-fold rotational (C_4). The user defines the value of ($10D_q$) in (eV), which is the energy gap between the t_{2g} and e_g levels. For octahedral (O_h) symmetry, the ($10D_q$) value is usually positive whereas for tetrahedral (D_{4h}) symmetry the value is negative, if ($10D_q$) is set to zero, i.e. no crystal field effect, the symmetry is spherical. Additional crystal field parameters such as (D_τ) and (D_σ) are available for all symmetries (except for (O_h)), see section (2.2.6). The exchange field can be used allowing the study of magnetic effects, i.e to calculate XMCD and XMLD spectra. In addition, charge transfer effect can be applied by activating the option and defining the parameters in eV; Δ, U_{dd}, U_{pd} and hopping T, where Δ is the energy difference between the centre of the $3d^n$ and $3d^{n+1}\underline{\mathrm{L}}$ configurations, U_{dd} and U_{pd} are the on-site dd Coulomb repulsion and the core-hole potential, respectively. The hopping T parameters; T(a_1), T(b_1), T(b_2) and T(e) are given for different symmetries. The T(a_1) and T(b_1) are related to (z^2) and($x^2 - y^2$) the e_g orbitals and T(b_2) and T(e) are related to (xy) and (xz, yz), respectively. The last step is plotting the parameters. The spectrum broadening can be corrected to fit the experimental resolution and core-hole lifetime effects using Gaussian and Lorentzain functions, respectively [96]. In this thesis iron, cobalt and titanium spectra are calculated using CTM4XAS code. Only atomic multiplet calculations and crystal field effect are applied to generate $L_{2,3}$ edges for $3d^5$, $3d^6$, $3d^7$ and $3d^0$ configurations.

After the measurement is run, the calculated spectrum is generated and saved. The calculated spectrum file, (file.xy) can be plotted along side the experimental data and compared using origin software. Fitting the calculated to experimental spectra allows the user to assess the oxidation state, site occupancy and give crystal field energy for a certain element within the sample [97].

Chapter 4

$SrCo_xTi_xFe_{12-2x}O_{19}$, $0 \leq x \leq 2$ Polycrystalline Samples

This chapter presents the synthesis and characterisation of $SrCo_xTi_xFe_{12-x}O_{19}$ polycrystalline samples with x= 0, 0.7, 1.1, 1.5 and 2. The discussion starts with the synthesis method, followed by structural characterisation, using X-ray diffraction and scanning electron microscopy, and finishes with the magnetic properties of the samples using VSM-SQUID magnetometer.

4.1 Polycrystalline samples prepared using solid state method

$SrCo_xTi_xFe_{12-x}O_{19}$ polycrystalline samples with x= 0, 0.7, 1.1, 1.5 and 2 were prepared using the solid state method. The starting materials used were $SrCO_3$ (Sigma Aldrich, $\geq$ 99.9%), TiO_2 (Sigma Aldrich, $\geq$ 99.98%), Fe_2O_3 (Sigma Aldrich, $\geq$ 99.995%) and CoO (Stanford, $\geq$ 99.9%). Firstly, $SrCO_3$ and Fe_2O_3 were dried at 130 ℃ for 2 h, prior to use to ensure the removal of any absorbed water. Correct amounts of the starting materials were mixed together with acetone using an agate mortar and pestle. The resultant material was then milled using a high speed ball mill (MSK-SFM-3) with a nylon jar and zirconia milling balls. The milling process was carried out at 350 rmp for 4 h, with acetone. The powder to liquid mass ratio was 1: 1, and the powder to Zirconia balls weight ratio was 1:9.7. Later, the material was dried and then transferred to an alumina crucible and sintered in a tube furnace (GSL-1500X-42-HGL). The samples were sintered at 1200 ℃ for 10 h twice in an oxygen atmosphere, following references [34][11]. After the first sintering process, the samples were milled again with the same conditions stated above, prior to the second sintering. The crystal structure and phase purity of the samples were determined using X-ray diffraction.

4.2 XRD analysis

All hexaferrite polycrystalline samples were characterised by X-ray diffraction. The XRD pattern of the samples were collected at the I11-beamline, Diamond light source, UK, with a maximum X-ray flux at 15 keV, which is equivalent to 0.826504(10) Å wavelength. The experiments were performed in the Debye-Scherrer

scattering geometry using a parallel X-ray beam. In order to reduce the sample absorption effect, the samples were mounted around a 0.3 mm capillary using a high vacuum grease. The capillary was mounted on a brass holder, as shown in figure (4.1).

Figure 4.1: Sample (x=0) mounted on capillary.

Scans were recorded over a 2θ range of $(4° - 150°)$. The total count time was 1800 s. The XRD pattern of the samples are shown in figure (4.2). For comparison and clarity, the XRD patterns were plotted from $(10°$ to $70°)$ due to the low intensity peaks at the high angle.

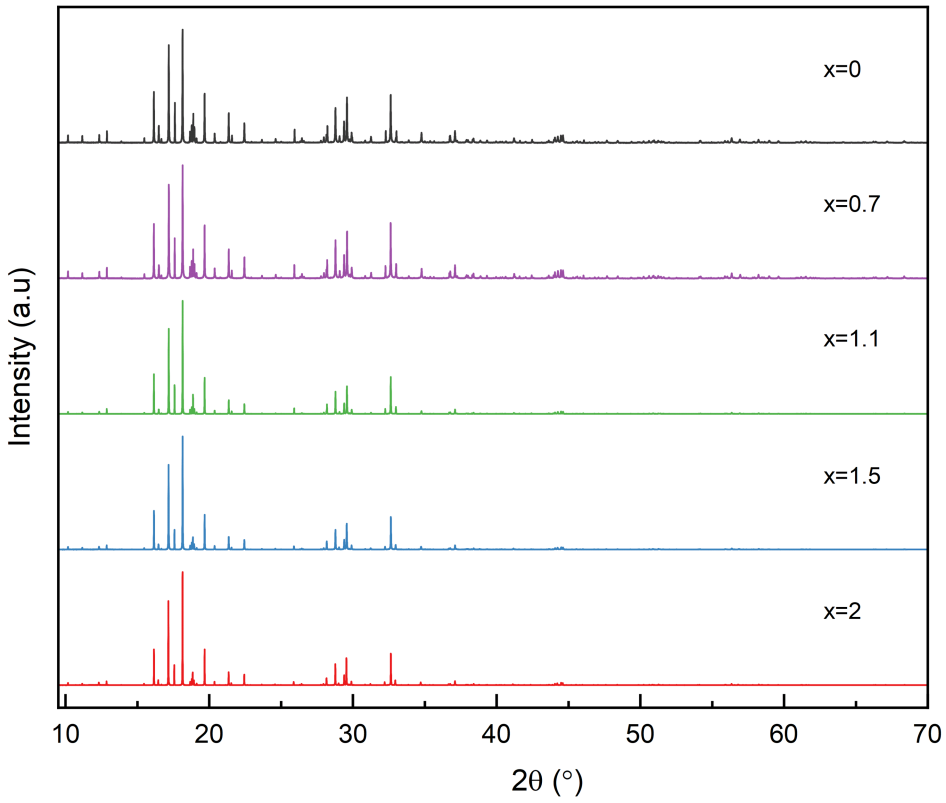

Figure 4.2: XRD patterns for $SrCo_xTi_xFe_{12-x}O_{19}$ M-type hexaferrite samples, where the black line represents x=0, the purple blue is x=0.7, the green line is x=1.1, the blue line is x= 1.5 and the red line is x= 2. The intensity of XRD patterns were normalised and shifted for comparison.

As seen from the figure (4.2), all samples show similar diffraction patterns with slightly shifted peak positions as the (Co-Ti) substitution is introduced. Phase identification was carried out by comparing peak position with database entries and indexing the diffraction patterns. Figure (4.3) shows that the peaks in the XRD pattern for x=0 sample can be indexed to M-type hexaferrite phase with the addition of an impurity phase that can be assigned to Fe_2O_3. This result is consistent with the standard pattern of $SrFe_{12}O_{19}$ (COD-1006001) and Fe_2O_3 Hematite (COD-15840), the figure is found in appendix (B).

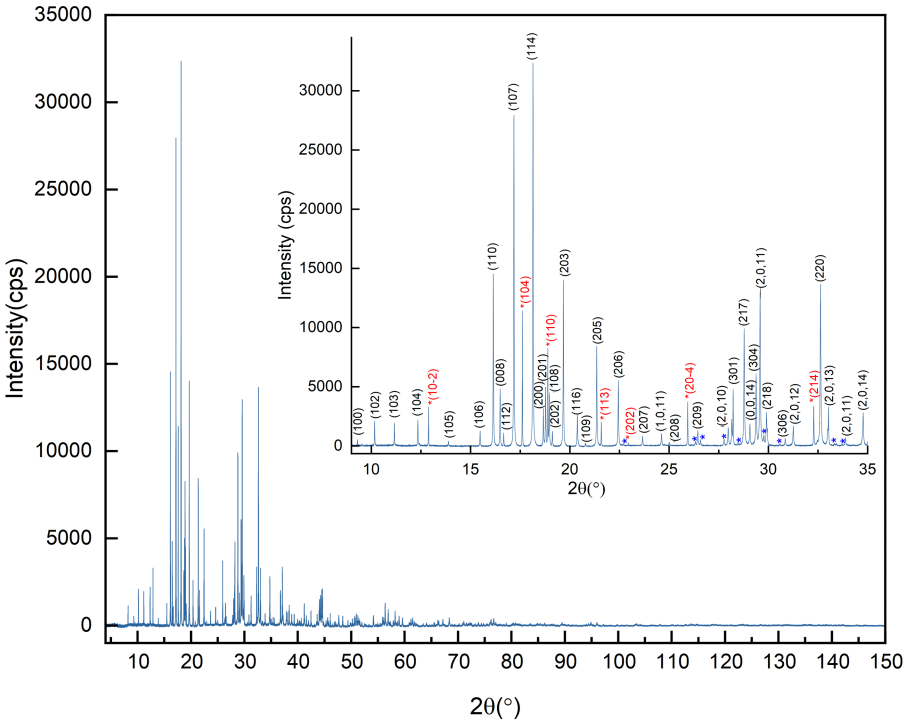

Figure 4.3: XRD pattern for x=0 sample with corresponding planes (hkl), the black (hkl) label belongs to $SrFe_{12}O_{19}$ phase and the red label belongs to Fe_2O_3 phase. The blue asterisks are corresponding to $SrFe_{12}O_{19}$ phase, labels are omitted for clarity.

Further analysis of the phase mixture was performed using Match! software [98]. The results show that the XRD pattern of the samples exhibit M-type hexaferrite as the major phase and Fe_2O_3 (Hematite) as the minor phase as shown in table (4.1).

Table 4.1: The weight percentage of the phase mixture for the samples using Match!.

Sample	M-type hexaferrite (%)	Fe_2O_3 (%)
x=0	89.4 ± 1	10.6 ± 1
x=0.7	87.7 ± 4	12.3 ± 4
x=1.1	88.2 ± 3	11.8 ± 3
x=1.5	94.6 ± 1	5.4 ± 1
x=2	95.2 ± 1	4.8 ± 1

The size of the coherently diffracting domains, commonly known as "the average particle size", for the hexaferrite samples was estimated using Scherrer equation. Recalling equation (3.27):

$$\beta_{size} = FWHM^{hkl} = \frac{k\lambda}{\tau \cos\theta} \tag{4.1}$$

where λ is equal to 0.826504 Å and the Scherrer constant, k, is taken to be 0.9 [99]. The FWHM was determined from (1 1 0), (1 0 7), (1 1 4), (2 0 3), (2 0 5) and (2 0 6) reflections. The result is given in figure (4.4). As can be seen, the size of the coherently diffracting domains increased linearly with (Co-Ti) substitution. For x=0, the size of the coherently diffracting domains is (1050 ± 50 nm). As the (Co-Ti) ions were introduced, β increased to (1230 ± 70 nm) for x=0.7. As the (Co-Ti) content increases further, β increases from (1280 ± 80 nm) for x=1.1, (1310 ± 90 nm) for x=1.5, to (1440 ± 70 nm) for x=2. This result is consistent with work in [8].

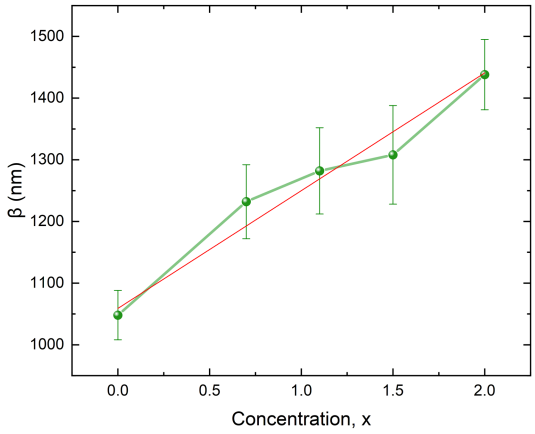

Figure 4.4: The size of the coherently diffracting domains for the M-type hexaferrite samples fitted with linear Regression model.

The XRD pattern for the M-type hexaferrite samples were analysed with the Rietveld method using GSAS-II software [77], see section 3.2.1. The structural calculated patterns are ; $SrFe_{12}O_{19}$ (model-1) [100], $BaCo_{0.85}Ti_{0.85}Fe_{10.3}O_{19}$ (model-2)[101] , $BaCo_1Ti_1Fe_{10}O_{19}$ (model-3) and $BaCo_2Ti_2Fe_8O_{19}$ (model-4)[102], as well as Fe_2O_3 [103], given in appendix (B). Before performing the refinement, modifications were applied to models (2, 3 and 4) in order to match the chemical formulas.

The refinements were carried out at 2θ range 10°-90° using M-type hexaferrite and hematite phases that belong to ($P6_3/mmc$) space group (194), and ($R\bar{3}c$) space group (164), respectively. The background of the patterns were refined using a Chebyschev-1 function with 16 coefficients. The zero point was set to 0.00124°. The patterns were corrected for preferred orientation using the spherical harmonic model with 8 harmonic orders. There was no additional improvement for higher order spherical harmonics.

$SrFe_{12}O_{19}$ (model-1) along with Fe_2O_3 were used to refine the XRD pattern for x=0, see figure (4.5). As can be seen, the experimental data fits well with the models. The refined lattice parameters along with the weight fraction for the phases

are given in table (4.2) and the structure parameters for refined $SrFe_{12}O_{19}$ is given in table (4.3).

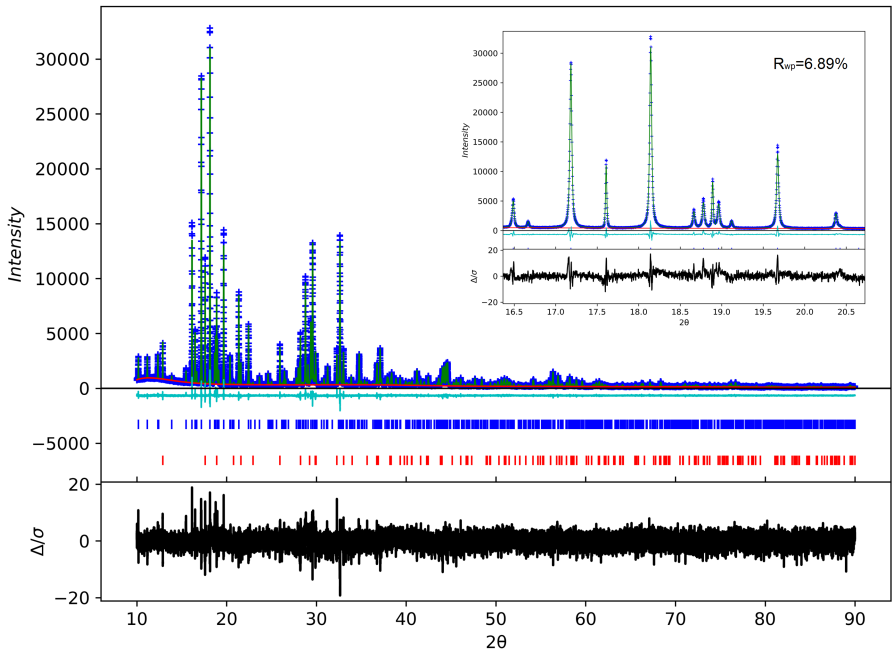

Figure 4.5: The refined XRD pattern of x=0 data using Rietveld refinement. The blue crosses are the observed data, the green line is the fitted calculated pattern and the black line is the difference between them. The blue and red tick marks indicate the expected 2θ positions for M-type hexaferrite and hematite phases, respectively. Zoom in reflections (1 0 7) and (1 1 4) shown as inset.

At convergence, the final values of all refined parameters were as follow; the scale factor was 1.37(1) and the peak width parameters were (u=0.960°^{2}, v=-0.697°^{2} and w=0.188 °^{2}). The magnitude of the preferred orientation was 1.011(2), which is close to unity, indicating that the texture is random [104][72]. The number of observations was 40001 and the number of variables parameters was 26. The quality of the refinement, R factors, were $R_{wp} = 6.98\%$, $\chi^2 = 163456$ and GOF = 2.02.

Table 4.2: The unit cell parameters and weight fraction of x=0 pattern.

Sample	M-type hexaferrite	Fe_2O_3	M-type hexaferrite literature [21]	Fe_2O_3 literature [105]
a (Å)	5.8853(5)	5.0354(6)	5.8847	5.0324(9)
c (Å)	23.0451(4)	13.7512(3)	23.0511	13.764(4)
V (Å^3)	691.6(2)	302.08(1)	-	301.88
wt.fraction	88.73(5)	10.80(5)	-	-

Table 4.3: The atomic coordinates (x, y, z), fractional occupancy (Occ.), isotropic temperature factors (B), occupancy site (Site) and symmetry of the site (sym.) for refined $SrFe_{12}O_{19}$ pattern.

Structure parameters	x	y	z	Occ.	B	Site	Sym.
Sr1	0.66670	0.33330	0.25000	1	0.895	2d	-6m2
Fe1	0.00000	0.00000	0.00000	1	0.372	2a	-3m
Fe2	0.00000	0.00000	0.25538	0.50	0.521	4e	3m
Fe3	0.33330	0.66670	0.02721	1	0.345	4f	3m
Fe4	0.33330	0.66670	0.19091	1	0.388	4f	3m
Fe5	0.17102	0.34203	0.89081	1	0.399	12k	m
O1	0.00000	0.00000	0.15140	1	0.468	4e	3m
O2	0.66670	0.33330	0.05540	1	0.490	4f	3m
O3	0.18190	0.36380	0.25000	1	0.719	6h	mm2
O4	0.15640	0.31280	0.05252	1	0.416	12k	m
O5	0.50390	0.00780	0.15093	1	0.508	12k	m

For x=0.7 sample, the refinement was preformed using $BaCo_{0.85}Ti_{0.85}Fe_{10.3}O_{19}$ (model-2) and Fe_2O_3 calculated patterns, see figure (4.6). Model-2 was modified to match the $SrCo_{0.7}Ti_{0.7}Fe_{10.6}O_{19}$ compound. The first adjustment was replacing the Ba ion with Sr ion. The second adjustment was to alter the amount of (Co, Ti and Fe) cations to match the chemical formula to that of the experimental one, including the occupancy of sites for Co1, Co2, Ti1 and Ti2 ions which were reduced to (0.090), and for Fe3 and Fe4 ion which was increased to (0.91), Fe(5) to (0.820).With the assumption that Co and Ti ions occupy equally octrahedral and tetrahedral sites, and only the Fe ions the bi-pyramidal trigonal (2b) site, as suggested in literature [8]. As shown, the experimental data fits well with the models. The refined lattice parameters and weight fraction for the phases are given in table (4.4).

Table 4.4: The unit cell parameters and weight fraction of x=0.7 pattern.

Sample	M-type hexaferrite	Fe_2O_3	Fe_2O_3 literature [105]
a (Å)	5.8850(7)	5.0342(1)	5.0324(9)
c (Å)	23.045(3)	13.760(4)	13.764(4)
V (Å^3)	691.216(2)	302.41(3)	301.88
wt.fraction	91.07(2)	8.93(2)	-

The structure parameters for refined $SrCo_{0.7}Ti_{0.7}Fe_{10.6}O_{19}$ is given in table (4.5). At convergence, the final values of all refined parameters were as follow; the scale factor was 1.335(1) and the peak width parameters were (u=0.814$^{\circ 2}$ v=-0.799$^{\circ 2}$ and w=0.012 $^{\circ 2}$). The texture index was 1.003(0), suggesting the texture is random. The number of observations was 40001 and the number of variables parameters was 17. The quality of refinement was $R_{wp} = 8.87\%$, $\chi^2 = 219433$ and GOF = 2.34.

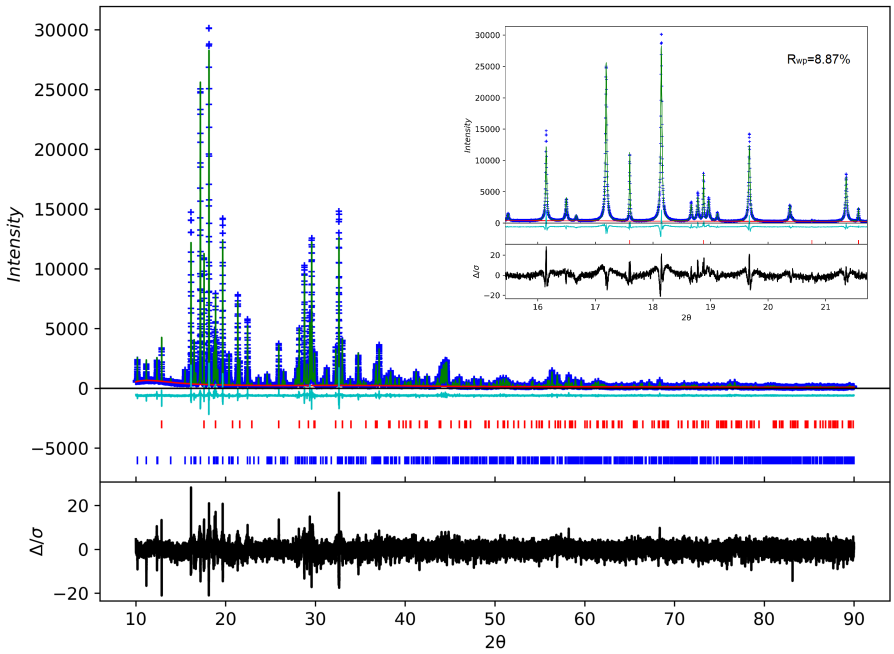

Figure 4.6: The refined XRD pattern of x=0.7 data. The blue crosses are the observed data, the green line is the fitted calculated pattern and the black line is the difference between them. The blue and red tick marks indicate the expected 2θ positions for M-type hexaferrite and hematite phases, respectively. Zoom in reflections (1 0 7) and (1 1 4) shown as inset.

Table 4.5: The atomic coordinates (x, y, z), fractional occupancy (Occ.), isotropic temperature factors (B), occupancy site (Site) and symmetry of the site (sym.) for refined $SrCo_{0.7}Ti_{0.7}Fe_{10.6}O_{19}$ pattern.

Structure parameters	x	y	z	Occ.	B	Site	Sym.
Sr1	0.66670	0.33330	0.25000	1	0.730	2d	-6m2
Fe1	0.00000	0.00000	0.00000	1	0.660	2a	-3m
Fe2	0.00000	0.00000	0.25755	0.50	0.410	4e	3m
Fe3	0.33330	0.66670	0.02689	0.893	0.250	4f	3m
Co1	0.33330	0.66670	0.02313	0.090	0.250	4f	3m
Fe4	0.33330	0.66670	0.18947	0.893	0.600	4f	3m
Ti1	0.33330	0.66670	0.18851	0.090	0.600	4f	3m
Fe5	0.16910	0.33821	0.89213	0.840	0.480	12k	m
Co2	0.16704	0.33408	0.88798	0.090	0.480	12k	m
Ti2	0.17384	0.34767	0.88851	0.090	0.480	12k	m
O1	0.00000	0.00000	0.15353	1	0.47	4e	3m
O2	0.33330	0.66670	0.94310	1	0.540	4f	3m
O3	0.18503	0.37005	0.25000	1	0.440	6h	mm2
O4	0.15152	0.30305	0.05296	1	0.500	12k	m
O5	0.51098	0.02197	0.15147	1	0.470	12k	m

For x=1.1, the refinement was preformed using $BaCo_1Ti_1Fe_{10}O_{19}$ (model-3) and Fe_2O_3 calculated patterns, see figure (4.7). Model-3 was modified by replacing the cation type with Sr ion and increasing the Co and Ti contents from (0.0833) to (0.090). Hence, Fe ion was reduced from (0.8333) to (0.815) to match the $SrCo_{1.1}Ti_{1.1}Fe_{9.8}O_{19}$ formula, assuming Co, Ti and Fe ions occupy equally all five sites. As shown, the experimental data fits reasonably well with models. The refined lattice parameters and weight fraction for the phases are given in table (4.6).

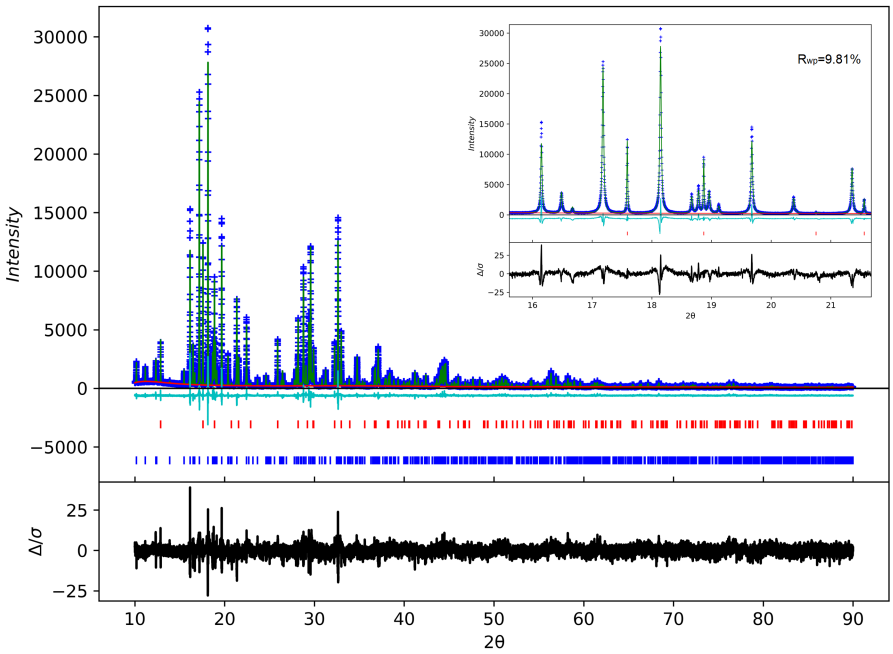

Figure 4.7: The refined XRD pattern of x=1.1 data using Rietveld refinement. The blue crosses are the observed data, the green line is the fitted calculated pattern and the black line is the difference between them. The blue and red tick marks indicate the expected 2θ positions for M-type hexaferrite and hematite phases, respectively. Zoom in reflections (1 0 7) and (1 1 4) shown as inset.

Table 4.6: The unit cell parameters and weight fraction of x=1.1 pattern.

Sample	M-type hexaferrite	Fe_2O_3	Fe_2O_3 literature [105]
a (Å)	5.8841(7)	5.0334(6)	5.0324(9)
c (Å)	23.0589(4)	13.7582(3)	13.764(4)
V (Å^3)	691.48(2)	302.07(1)	301.88
wt.fraction	88.53(1)	11.47(1)	-

The structure parameters for refined the $SrCo_{1.1}Ti_{1.1}Fe_{9.8}O_{19}$ is given in table (4.7). At convergence, the final values of all refined parameters were as follow; the scale factor was 1.533(1) and the peak width parameters were (u=0.603$^{\circ 2}$ v=-0.506$^{\circ 2}$ and w=0.201 $^{\circ 2}$). The texture index was 1.003(0). The number of observations was 40001 and the number of variables parameters was 19. The quality of refinement was $R_{wp} = 9.81\%$, $\chi^2 = 256429$ and GOF = 2.53.

Table 4.7: The atomic coordinates (x, y, z), fractional occupancy (Occ.), isotropic temperature factors (B), occupancy site (Site) and symmetry of the site (sym.) for refined $SrCo_{1.1}Ti_{1.1}Fe_{9.8}O_{19}$ pattern.

Structure parameters	x	y	z	Occ.	B	Site	Sym.
Sr1	0.33330	0.66670	0.25000	1	1	2c	-6m2
Co1	0.00000	0.00000	0.00000	0.090	1	2a	-3m
Ti1	0.00000	0.00000	0.00000	0.090	1	2a	-3m
Fe1	0.00000	0.00000	0.00000	0.815	1	2a	-3m
Co2	0.00000	0.00000	0.025000	0.090	1	2b	-6m2
Ti2	0.00000	0.00000	0.025000	0.090	1	2b	-6m2
Fe2	0.00000	0.00000	0.025000	0.815	1	2b	-6m2
Co3	0.33330	0.66670	-0.02526	0.0903	1	4f	3m
Ti3	0.33330	0.66670	-0.02532	0.0903	1	4f	3m
Fe3	0.33330	0.66667	-0.02705	0.8153	1	4f	3m
Co4	0.33330	0.66670	-0.18733	0.0903	1	4f	3m
Ti4	0.33330	0.66670	-0.18733	0.0903	1	4f	3m
Fe4	0.33330	0.66670	-0.18984	0.8153	1	4f	3m
Co5	0.16836	0.33672	0.10929	0.090	1	12k	m
Ti5	0.17151	0.34303	0.10932	0.092	1	12k	m
Fe5	0.16744	0.33488	0.10831	0.815	1	12k	m
O1	0.00000	0.00000	0.15361	1	1	4e	3m
O2	0.33330	0.6670	0.05649	1	1	4f	3m
O3	0.81837	0.63673	0.25000	1	1	6h	mm2
O4	0.84390	0.68780	0.05366	1	1	12k	m
O5	0.49539	0.00921	0.15117	1	1	12k	m

For x=1.5, the refinement was preformed using $BaCo_1Ti_1Fe_{10}O_{19}$ (model-3) and Fe_2O_3 calculated patterns, see figure (4.8). Similar to x=1.1, model-3 was modified by replacing the cation type with Sr ion and increasing the Co and Ti contents from (0.0833) to (0.125). Therefore, Fe ion was reduced from (0.8333) to (0.750) to match $SrCo_{1.5}Ti_{1.5}Fe_9O_{19}$ formula. It was assumed that Co, Ti and Fe ions occupy equally all five sites. The refined lattice parameters and weight fraction for the phases are given in table (4.8). The structure parameters for refined $SrCo_{1.5}Ti_{1.5}Fe_9O_{19}$ are given in table (4.9).

At convergence, the final values of all refined parameters were as follow; the scale factor was 4.77(5) and the peak width parameters were (u=0.777$^{\circ 2}$ v=-0.565$^{\circ 2}$ and w=0.200$^{\circ 2}$). The texture index was 1.006(0). The number of observations was 40001 and the number of variables parameters was 17. The quality of refinement was $R_{wp} = 9.8\%$, $\chi^2 = 266935$ and GOF = 2.58.

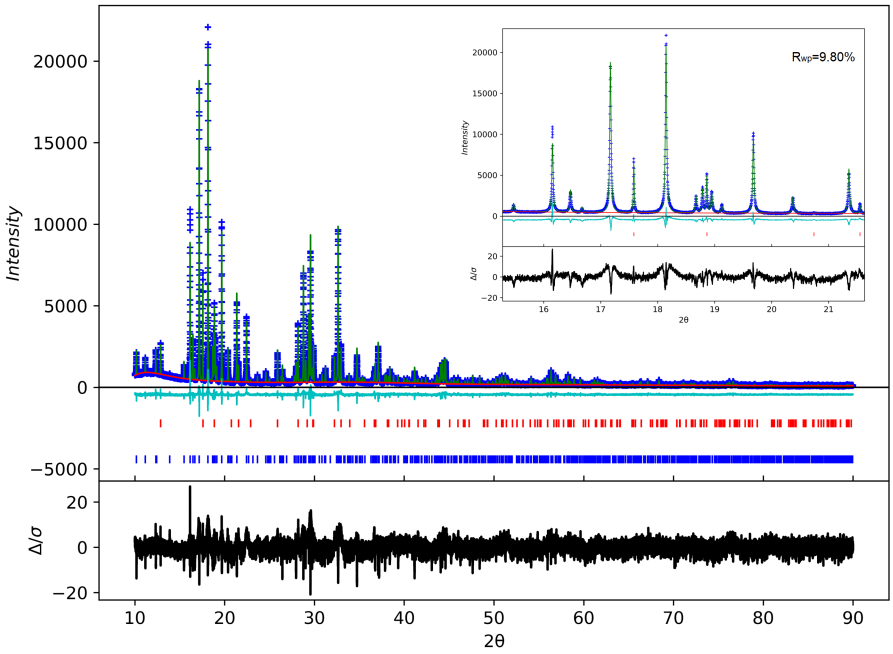

Figure 4.8: The refined XRD pattern of x=1.5 data using Rietveld refinement. The blue crosses are the observed data, the green line is the fitted calculated pattern and the black line is the difference between them. The blue and red tick marks indicate the expected 2θ positions for M-type hexaferrite and hematite phases, respectively. Zoom in reflections (1 0 7) and (1 1 4) shown as inset.

Table 4.8: The unit cell parameters and weight fraction of x=1.5 pattern.

Sample	M-type hexaferrite	Fe_2O_3	M-type hexaferrite ref [106]	Fe_2O_3 ref [105]
a (Å)	5.8826(6)	5.0340(1)	5.8831	5.0324(9)
c (Å)	23.082(4)	13.77(3)	23.084	13.764(4)
V (Å^3)	691.83(7)	302.48(6)	-	301.88
wt.fraction	90.47(1)	9.53(1)	-	-

Table 4.9: The atomic coordinates (x, y, z), fractional occupancy (Occ.), isotropic temperature factors (B), occupancy site (Site) and symmetry of the site (sym.) for refined $SrCo_{1.5}Ti_{1.5}Fe_9O_{19}$ pattern.

Structure parameters	x	y	z	Occ.	B	Site	Sym.
Sr1	0.33330	0.6667	0.25000	1	1	2c	-6m2
Co1	0.00000	0.00000	0.00000	0.125	1	2a	-3m
Ti1	0.00000	0.00000	0.00000	0.125	1	2a	-3m
Fe1	0.00000	0.00000	0.00000	0.750	1	2a	-3m
Co2	0.00000	0.00000	0.025000	0.125	1	2b	-6m2
Ti2	0.00000	0.00000	0.025000	0.125	1	2b	-6m2
Fe2	0.00000	0.00000	0.025000	0.750	1	2b	-6m2
Co3	0.33330	0.66670	-0.02594	0.1253	1	4f	3m
Ti3	0.33330	0.66670	-0.02594	0.1253	1	4f	3m
Fe3	0.33330	0.66670	-0.02623	0.7503	1	4f	3m
Co4	0.33330	0.66670	-0.18689	0.1253	1	4f	3m
Ti4	0.33330	0.66670	-0.18653	1253	1	4f	3m
Fe4	0.33330	0.66670	-0.10917	0.7503	1	4f	3m
Co5	0.17000	0.34000	0.10891	0.125	1	12k	m
Ti5	0.17000	0.34000	0.10879	0.125	1	12k	m
Fe5	0.17000	0.34000	0.10782	0.750	1	12k	m
O1	0.00000	0.00000	0.15123	1	1	4e	3m
O2	0.33330	0.6670	0.05675	1	1	4f	3m
O3	0.81856	0.63712	0.25000	1	1	6h	mm2
O4	0.85123	0.70247	0.05332	1	1	12k	m
O5	0.50186	0.003720	0.15054	1	1	12k	m

For x=2, the refinement was preformed using $BaCo_2Ti_2Fe_8O_{19}$ (model-4) and Fe_2O_3 calculated patterns, see figure (4.9). Model-4 was modified by replacing the cation type with Sr ion to match the $SrCo_2Ti_2Fe_8O_{19}$ formula. It was assumed that Co, Ti and Fe ions occupy equally all five sites. As shown, the experimental data fits reasonably well with the models. The refined lattice parameters and weight fraction for the phases are given in table (4.10).

At convergence, the final values of all refined parameters were as follow; the scale factor was 0.8770(1) and the peak width parameters were (u=0.309°^{2}, v=-0.473°^{2} and w=0.154°^{2}). The texture index was 1.014(0). The number of observations was 40001 and the number of variables parameters was 19. The quality of refinement was R_{wp} = 9.97%, χ^2 = 194806 and GOF = 2.21. The structure parameters for refined $SrCo_2Ti_2Fe_8O_{19}$ is given in table (4.11).

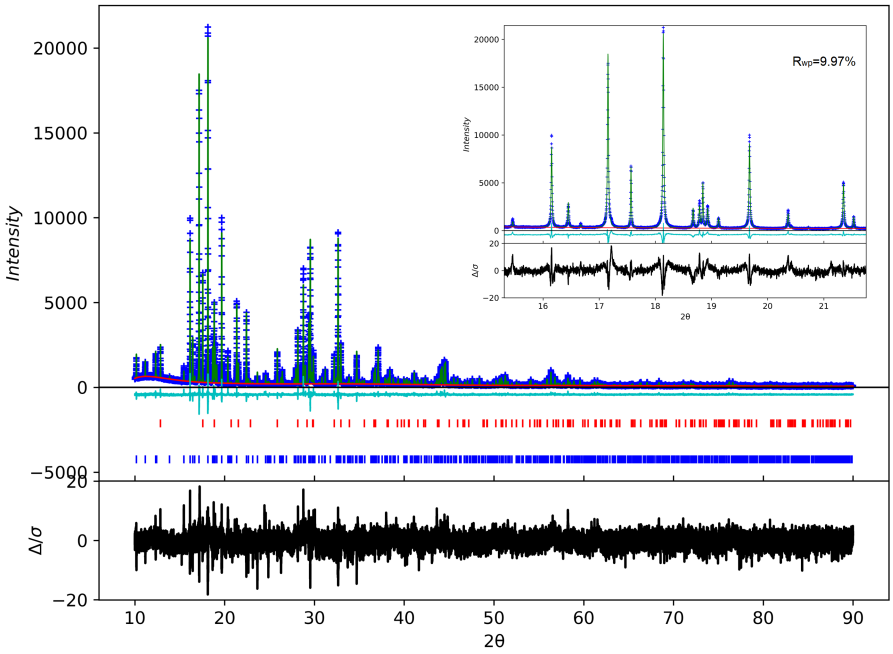

Figure 4.9: The refined XRD pattern of x=2 data from Rietveld refinement. The blue crosses are the observed data, the green line is the fitted calculated pattern and the black line is the difference between them. The blue and red tick marks indicate the expected 2θ positions for M-type hexaferrite and hematite phases, respectively. Zoom in reflections (1 0 7) and (1 1 4) shown as inset.

Table 4.10: The unit cell parameters and weight fraction of x=2 pattern.

Sample	M-type hexaferrite	Fe_2O_3	M-type hexaferrite ref [106]	Fe_2O_3 ref [105]
a (Å)	5.8829(8)	5.0380(2)	5.8831	5.0324(9)
c (Å)	23.109(3)	13.77(4)	23.084	13.764(4)
V (Å^3)	692.85(1)	302.20(2)	-	301.88
wt.fraction	87.3(3)	12.67(2)	-	-

Table 4.11: The atomic coordinates (x, y, z), fractional occupancy (Occ.), isotropic temperature factors (B), occupancy site (Site) and symmetry of the site (sym.) for refined $SrCo_2Ti_2Fe_8O_{19}$.

Structure parameters	x	y	z	Occ.	B	Site	Sym.
Sr1	0.33330	0.66670	0.25000	1	1	2c	-6m2
Co1	0.00000	0.00000	0.00000	0.167	1	2a	-3m
Ti1	0.00000	0.00000	0.00000	0.167	1	2a	-3m
Fe1	0.00000	0.00000	0.00000	0.667	1	2a	-3m
Co2	0.00000	0.00000	0.025000	0.167	1	2b	-6m2
Ti2	0.00000	0.00000	0.025000	0.167	1	2b	-6m2
Fe2	0.00000	0.00000	0.025000	0.667	1	2b	-6m2
Co3	0.33330	0.66670	-0.02525	0.167	1	4f	3m
Ti3	0.33330	0.66670	-0.02577	0.167	1	4f	3m
Fe3	0.33330	0.66670	-0.02636	0.667	1	4f	3m
Co4	0.33330	0.66670	-0.19160	0.167	1	4f	3m
Ti4	0.33330	0.66670	-0.18923	0.167	1	4f	3m
Fe4	0.33330	0.66670	-0.18923	0.667	1	4f	3m
Co5	0.16648	0.33296	0.10913	0.167	1	12k	m
Ti5	0.18578	0.371	056.10779	0.167	1	12k	m
Fe5	0.16759	0.33519	0.10773	0.667	1	12k	m
O1	0.00000	0.00000	0.151212	1	1	4e	3m
O2	0.33330	0.6670	0.05804	1	1	4f	3m
O3	0.80671	0.61342	0.25000	1	1	6h	mm2
O4	0.84491	0.68981	0.05288	1	1	12k	m
O5	0.49847	0.00307	0.15213	1	1	12k	m

Rietveld Refinement of the XRD pattern of the samples shows that the experimental data fits well with M-type hexaferrite structure, though not perfectly. The results show that c-lattice parameter increases slightly and a-lattice parameter decreases marginally as the Co-Ti ion increases, implying that the unit cell volume increase with substitution, which is in agreement with literature [107][8][106]. This can be explained by the average ionic radius of the (Co-Ti) ions, which is (0.627 Å), this is larger than Fe ion, (0.55 Å) [106]. The refined lattice parameters for the M-type hexaferrite samples compared with literature are given in figure (4.10).

In addition, the presence of Fe_2O_3 as secondary phase (less than 13%), was confirmed in all samples. Improvements to the refinement process could be carried out by refining the occupancy site of Co and Ti ions, instead of making the assumption that Co and Ti ions occupy equally all sites, except for x=0.7 where only the Fe ions enters the bi-pyramidal trigonal (2b) site. This could explain why the quality of fit for x=0 and 0.7 are better than the rest.

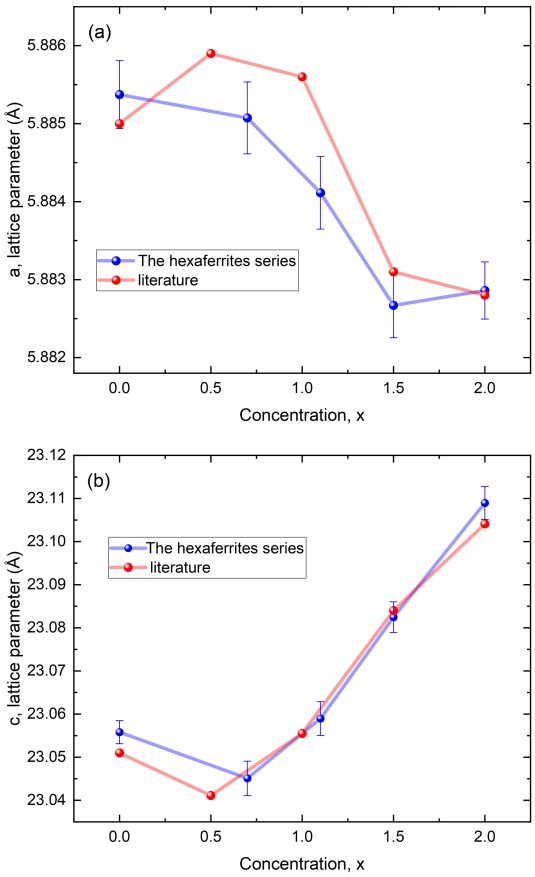

Figure 4.10: Variation of the lattice parameters as a function of concentration (a) The *a*-lattice parameter and (b) The *c*-lattice parameter. The literature value for x=0 is taken from ref [8] and the rest of literature values are taken from ref [106].

4.3 SEM analysis

The morphology and the chemical composition of the $SrCo_xTi_xFe_{12-x}O_{19}$ samples were determined using a 7800F-SEM with a beam energy of 20 keV and 8 nA probe current. The samples were mapped using the Oxford Instruments UltiMax-100EDS detector and the AZtecLive software at a magnification of (1000×) in order to cover a relatively broad area of the samples. The loose powders were mounted onto a 25 mm aluminium stub using sticky carbon tabs; more details can be found in appendix (C).

ZAF corrections were applied to EDS measurement to take into account the effect of the atomic number (Z) which affects the penetration of primary electrons into the material, absorption of X-rays in the specimen (A) and fluorescence caused by secondary X-rays generated in the specimen (F). A visual inspection of the SEM images indicates that the $SrFe_{12}O_{19}$ sample has a smaller average particle size.

Moreover, as the Co-Ti substitution increases the grains become larger. These results are consistent with the XRD measurements and in agreement with ref [106]. Figure (4.11) with a higher magnification of (16000×) showing that the samples exhibit agglomerations of small particles with hexagonal and plate-like shape, similar to ref [108].

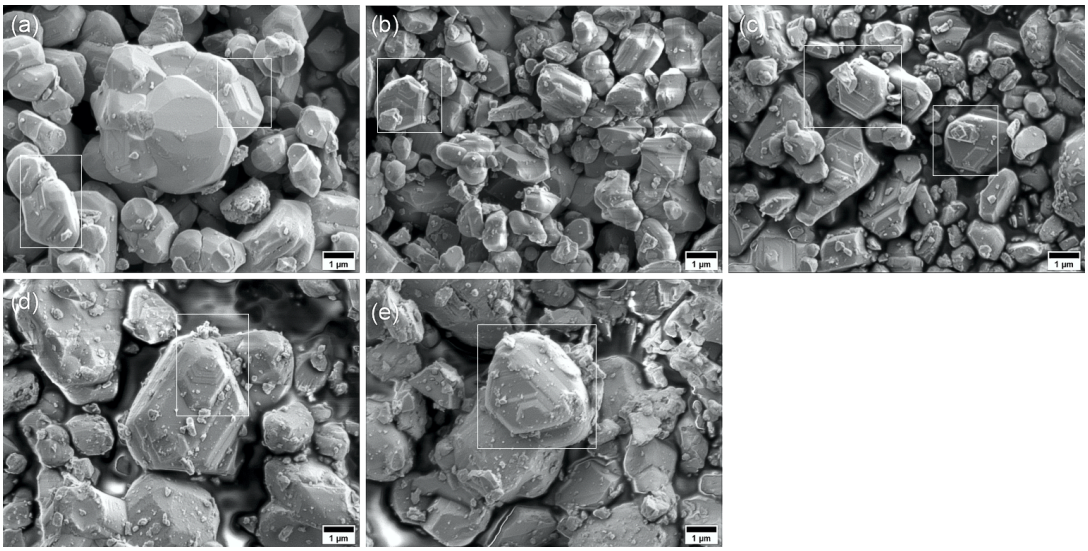

Figure 4.11: SEM images for $SrCo_xTi_xFe_{12-x}O_{19}$ hexaferrite with 16000× magnification (a) x=0, (b) x=0.7, (c) x=1.1,(d) x= 1.5 and (e) x= 2.

The EDS elemental analysis of the samples detected the elements Sr, Co, Ti, Fe and O. The results confirm that the substitution of Co and Ti ions for Fe ion increases in the samples. There is a small amount of Co and Ti elements in $SrFe_{12}O_{19}$ sample, as shown in figure (4.12). This contamination may have resulted from using the air gun to remove the excess powder. There is an excess of Fe and O elements, more than stoichiometry for M-type hexaferrite that could be attributed to the presence of the second phase Fe_2O_3 which is consistent with the XRD results. The average atomic percentage and the weight percentage of the samples along with the elemental maps for two sites are found in appendix (C) tables (C.1) and (C.2), respectively.

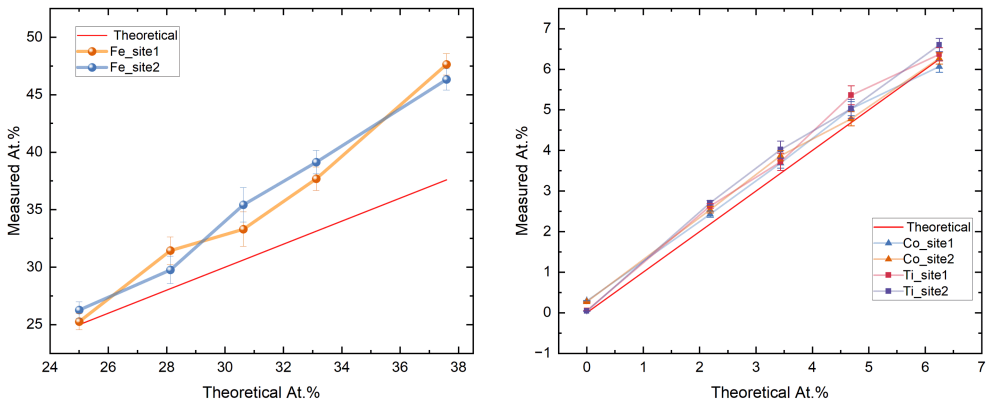

Figure 4.12: The measured versus nominal (theoretical) atomic percentages for the $SrCo_xTi_xFe_{12-x}O_{19}$ samples, for Fe ion (on the left) and Co-Ti substitution (on the right).

4.4 VSM analysis

Magnetisation measurements were carried out with a Quantum Design MPMS3 (SQUID-VSM) magnetometer, at the ISIS Neutron and Muon source, UK. The samples were loaded into powder sample holders (4096-388) and then mounted in

a brass half-tube. M-H measurements were obtained in the temperature range (6 K-380 K) and in an applied magnetic field up to 30 kOe. However, the samples did not reach saturation magnetisation at low temperature, even with an applied field of 70 kOe. This behavior has also been reported for substituted M-type hexaferrite, which could be associated with the presence of a large magneto-crystalline anisotropy [109] or canted spins [23][110]. Therefore, the values of saturation magnetisation were estimated using the law of approach to saturation (LAS), equation (3.46), in the field range from 25 kOe to 30 kOe with the assumptions that the field is high enough to saturate the sample and that the sample is homogeneous leading to the constant A≈0. The error associated with the saturation magnetisation value represents the error of the fitting to equation (3.46). The coercive field, H_c and the remanent magnetisation, M_r values were extracted directly from the loop. The first anisotropy constant values were obtained using equation (3.47).

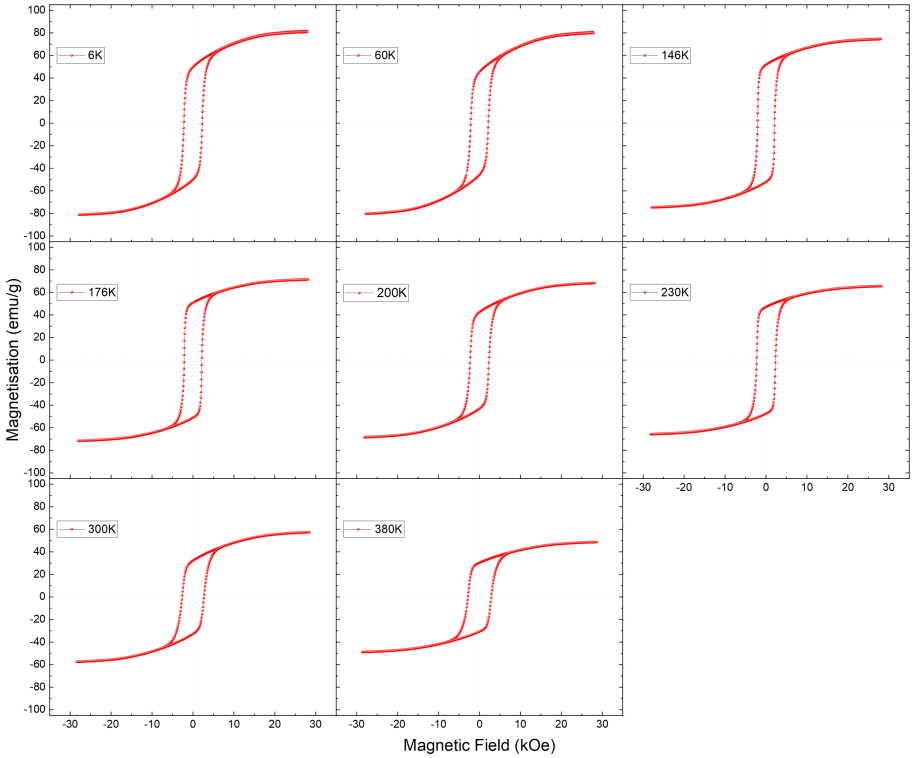

Figure 4.13: Hysteresis curves for x=0 at various temperatures.

Figure (4.13) shows the hysteresis curves for the sample x=0 at (6 K, 60 K, 146 K, 176 K, 200 K, 230 K, 300 K and 380 K). As shown, the sample exhibits a high coercive field of (2400 ± 300) Oe, indicating that the sample is a permanent magnet above room temperature as expected. In addition, the sample has a saturation magnetisation of (83 ± 2) emu/g at 6 K, which is close to the expected saturation magnetisation value of (100) emu/g at 0 K [19]. As the temperature increases the saturation magnetisation decreases to (50±2) emu/g at 380 K. The saturation magnetisation at room temperature was (59 ± 2) emu/g which is slightly higher than ($M_s \sim 50$) emu/g, found in ref [99] and slightly lower than one reported ($M_s \sim 70$) emu/g [111]. The remanent magnetisation was (50±2) emu/g at 6 K. Generally the remanent magnetisation, tends to decrease with temperature except between 150 K and 250 K.

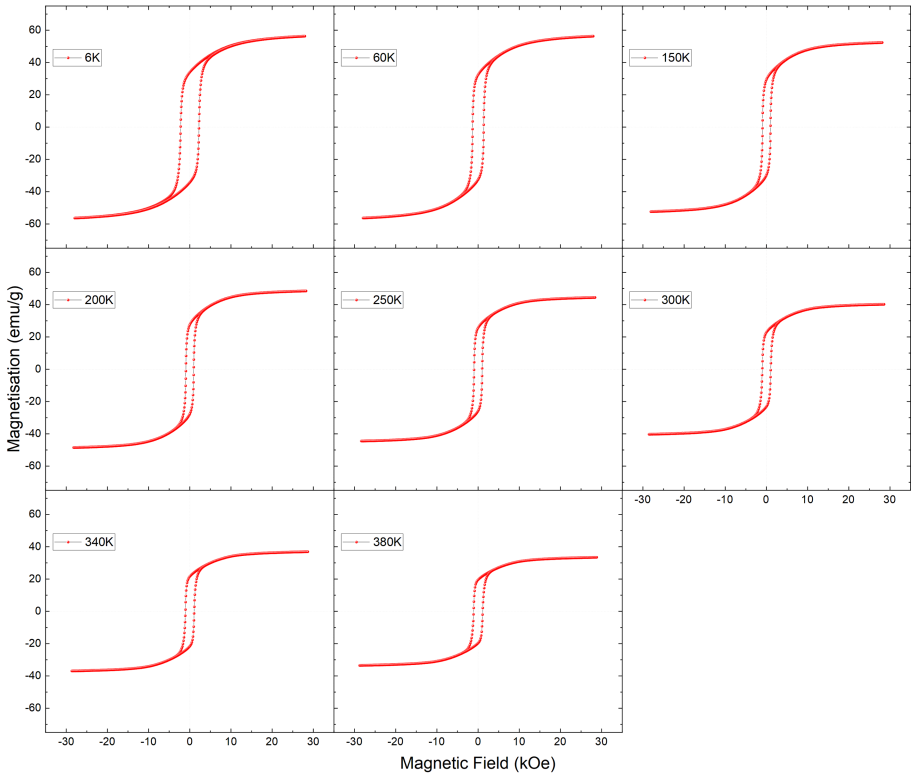

Figure 4.14: Hysteresis curves for x=0.7 at various temperatures.

Figure (4.14) shows the hysteresis curves for the sample x=0.7 at (6 K, 60 K, 150 K, 200 K, 250 K, 300 K, 340 K and 380 K). As shown, the sample exhibits high coercive field at a low temperature of (2230 ± 20) Oe. As the temperature increases, the coercive field decreases until 200 K, then starts to increase slowly up to (1105 ± 35) Oe at 380 K. The sample has a saturation magnetisation of (73 ± 3) emu/g at 6 K. As the temperature increases the saturation magnetisation decreases to (43 ± 2) emu/g at 380 K. The saturation magnetisation at room temperature was (52 ± 3) emu/g. The remanent magnetisation decreases with temperature from (33 ± 5) emu/g at 6 K to (21 ± 4) emu/g at 380 K.

The hysteresis curves for the sample x=1.1 at (6 K, 60 K, 150 K, 200 K, 230 K, 250 K, 300 K, 320 K and 380 K) are given in figure (4.15). The sample shows a wide range of coercive fields with temperature between (1312 ± 9) Oe and (126 ± 2) Oe. At 6 K, the coercive field has the highest value and starts to decrease down to (126 ± 2) Oe as the temperature increases. As the temperature increases further, the coercive field starts to increase once again reaching (311 ± 3) Oe at 380 K. The sample has a saturation, M_s of (62 ± 3) emu/g at 6 K, and decreases to (52 ± 3) emu/g and (43 ± 2) emu/g at 300 K and 380 K, respectively. The remanent magnetisation decreases with temperature from (36 ± 2) emu/g at 6 K to (20 ± 2) emu/g at 380 K.

Figure (4.16) shows the hysteresis curves for the sample x=1.5 at (6 K, 60 K, 150 K, 200 K, 230 K, 250 K, 300 K, 320 K and 380 K). At 6 K, the sample exhibits a weak wasp-waisted shape, in which the hysteresis curve narrows as the applied field approaches zero and then opens back up. Generally, this behavior is observed in materials that have two or more contrasting magnetic components such as a high-coercivity component mixed with a low-coercivity component that can be a mixture

of grain size in a single phase or mixture phases with contrasting coercivity [112].

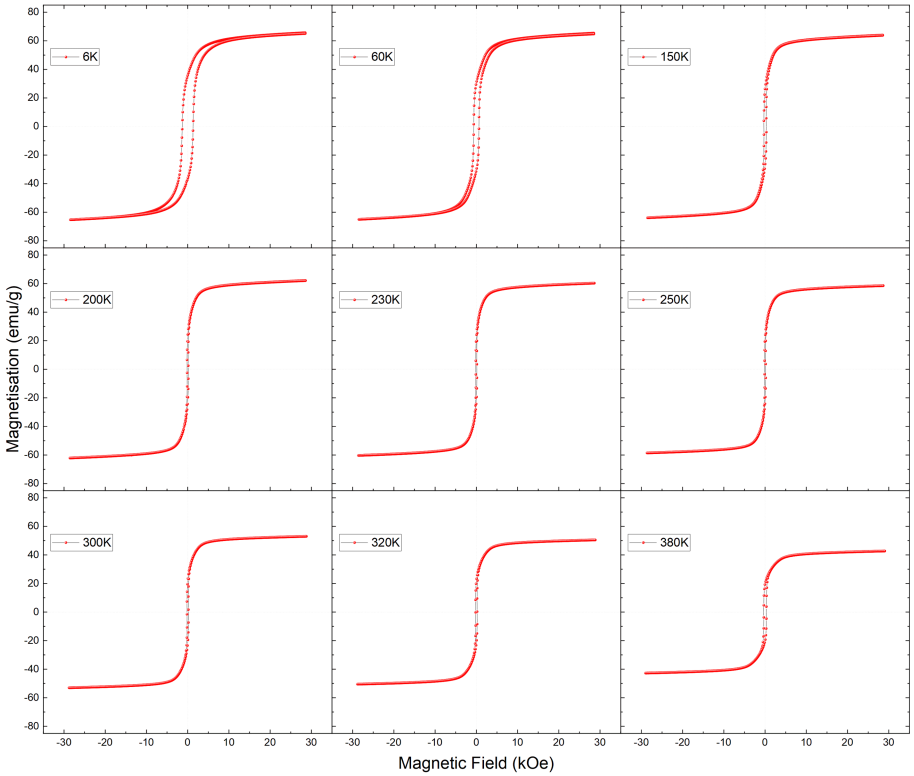

Figure 4.15: Hysteresis curves at for x=1.1 various temperatures.

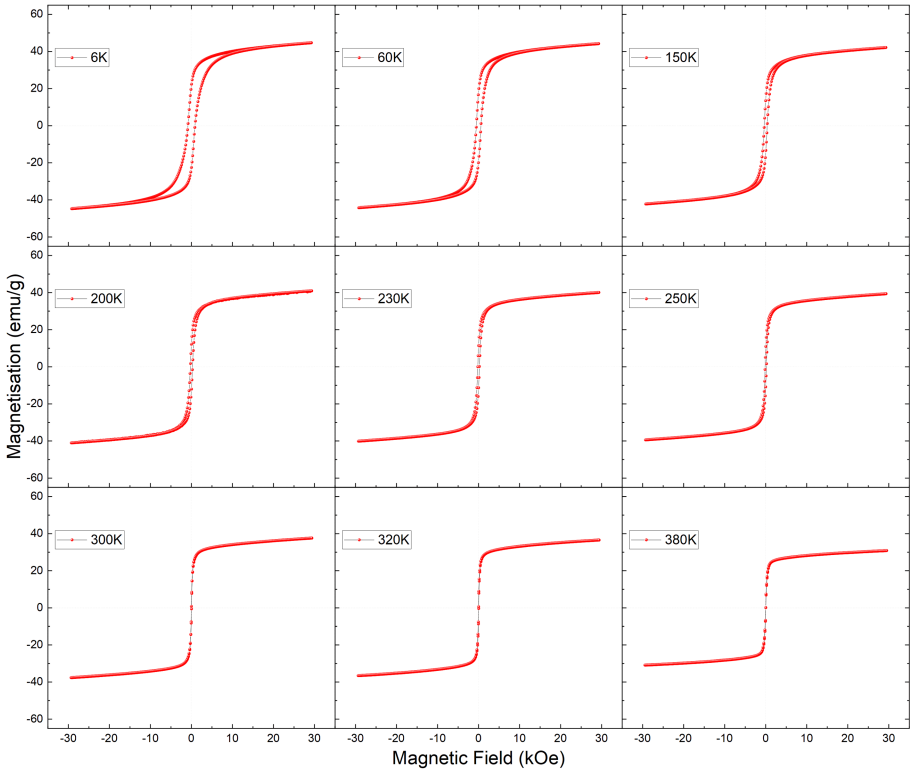

Figure 4.16: Hysteresis curves for x=1.5 at various temperatures.

In this work, haematite was observed as secondary phase in XRD data for all polycrystalline samples. Hematite is a collinear antiferromagnetic (AF) up to the Morin temperature around 250 K, and a weakly ferromagnetic or canted spin structure as the temperature increase up to 948 K. The magnetic properties of Haematite are complex depending on synthesis, morphology and microstructure. For example, the Morin temperature decreases by reducing the particle size and tends to be suppressed for particles of about 10 nm. The coercive field ranges between (0.3 - 3) kOe [113][114]. Therefore, it is not possible to confirm whether this effect arises from the coexistence of haematite with $SrCo_{1.5}Ti_{1.5}Fe_9O_{19}$ causing different coercivities. However, since, the observation of wasp-waisted shape was at low temperature, when Hematite is AF and the amount of Hematite is constant for all samples, around 10%, this behaviour is more likely due to the substitution of the Co-Ti ions at different sites within the lattice for different grain sizes and further investigation is required to establish the reason for this effect. As the temperature increases, the coercive field decreases (1.2 ± 0.5) Oe at 380 K. The value of the coercive field at room temperature was (17 ± 5) Oe which is similar to the one prepared by the sol-gel method (20 Oe) [106]. The sample has a low saturation temperature of (47 ± 4) emu/g at 6 K. As the temperature increases the saturation magnetisation decreases to (32 ± 2) emu/g at 380 K. The saturation magnetisation at room temperature was (40 ± 5) emu/g, which is slightly lower than the one prepared by sol-gel method (55.4) emu/g [106]. The remanent magnetisation decreases with temperature from (25 ± 2) emu/g at 6 K to (0.8 ± 0.4) emu/g at 380 K.

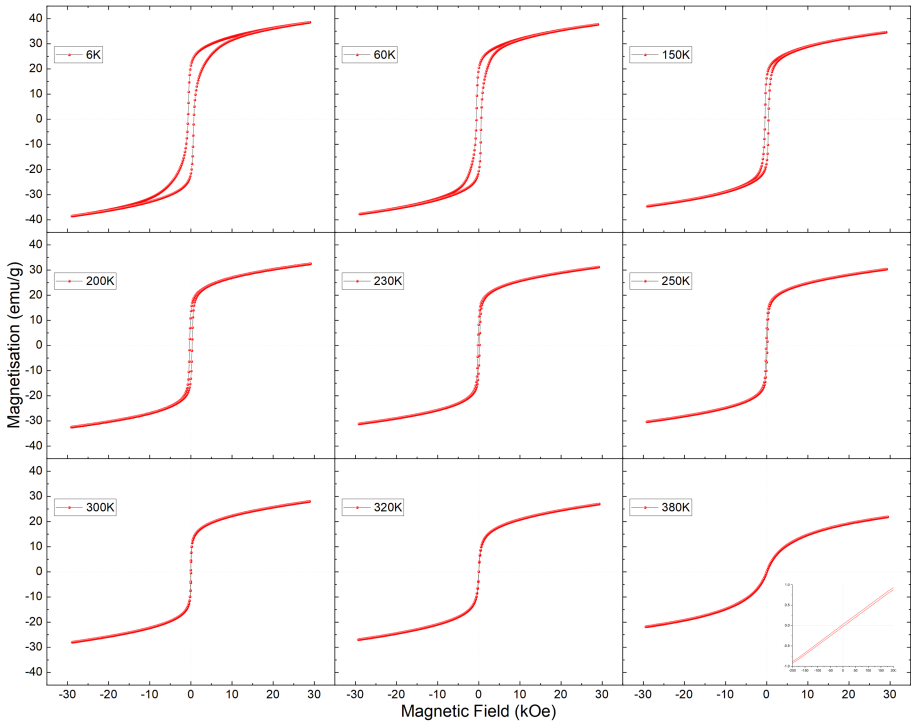

Figure 4.17: Hysteresis curves for x=2 at various temperatures.

The hysteresis curves for the sample x=2 at (6 K, 60 K, 150 K, 200 K, 230 K, 250 K, 300 K, 320 K and 380 K) are given in figure (4.17). The sample shows a pronounced wasp-waisted hysteresis loop at 6 K and 60 K. As the temperature increased, the wasp-waisted shape disappeared and the coercive field decreased to (6 ± 5) Oe at 380 K. The value of the coercive field at room temperature was (26 ± 5)

Oe which is lower than the one prepared by sol-gel method (65 Oe) [106]. The sample has a saturation magnetisation of (37 ± 6) emu/g at 6 K. As the temperature decreases, the saturation magnetisation decreases to (22 ± 5) emu/g at 380 K. The saturation magnetisation at room temperature was (25 ± 8) emu/g similar to the sample prepared by solid state method (30) emu/g [45]. The remanent magnetisation decreases with temperature from (23 ± 2) emu/g at 6 K to (5 ± 2) emu/g at 300 K, then its value becomes (<1 emu/g), at higher temperatures.

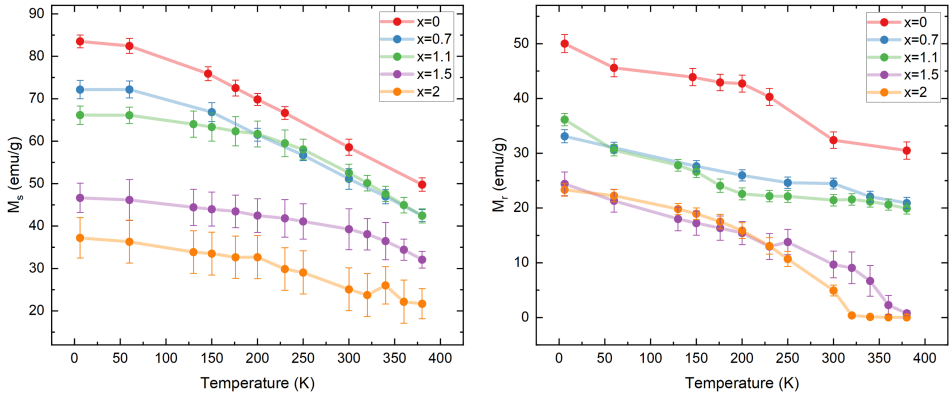

Figure 4.18: The saturation magnetisation and the remanent magnetisation as a function of temperature for the M-type polycrystalline samples.

The temperature dependence of the saturation magnetisation and the remanent magnetisation for the samples are given in figure (4.18). As can be seen, the saturation magnetisation decreases with an increase of Co-Ti substitution and temperature. The reduction in the saturation magnetisation can be attributed to replacing Fe^{3+} ions, which have a magnetic moment of $5\mu_B$, with non magnetic Ti^{4+} ions and Co^{2+} ions, which have a smaller moment of $3\mu_B$ [106]. In addition, the value of net magnetic moment depends on the preferential site occupancy of Co-Ti ions. According to neutron diffraction study, Ti^{4+} ions have a strong preference to occupy octahedral sites whereas Co^{2+} ions tend to occupy tetrahedral sites, and trigonal bipyramid (2b) site for (x>0.8) [8][115]. The remanent magnetisation also decreases with an increase in amount of Co-Ti substitution and temperature.

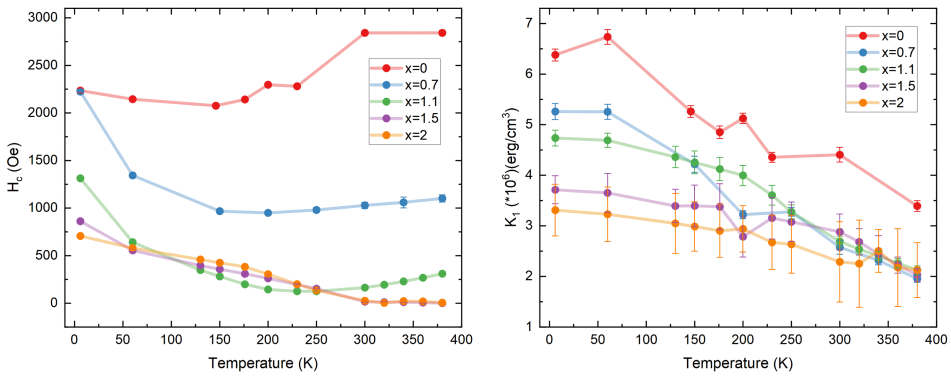

Figure 4.19: The coercive field and the first anisotropy constant as a function of temperature for the polycrystalline samples.

The temperature dependence of the coercive field and the first anisotropy constant of the M-type samples are given in figure (4.19). The coercive field for x=0 increases with temperature which could be associated with the presence of multi domain grains that have less Bloch walls and a reduction of the anisotropy constant as temperature increases [116][8]. Similar to other magnetic properties, the coercive field decreases with Co-Ti substitution, especially for (x >0.7), which agrees with the reported behaviour for the similar range, (0< x <1) [117]. The dramatic reduction of the coercive field for (x >0.7) can be explained by the tendency of Co^{2+} ions to occupy the trigonal bipyramid (2b) sites, leading to non-collinear magnetic structure and the development of a cone magnetisation [8]. The coercivity starts to level off for (x >1.1). Unlike, x=0, as temperature increases, the coercive field decreases, which can be explained by the presence of imperfections and defects due to substitution of Co-Ti, (especially for x=1.5 and 2) that interact with domains walls causing pinning and impedance to domain wall motion.

The first anisotropy constant for x=0 is calculated to $(4.4 \pm 0.2) \times 10^6\ erg/cm^3$ at 300 K which is slightly higher than the one reported ($3.5 \times 10^6\ erg/cm^3$) [21]. Generally, the first anisotropy constant decreases with Co-Ti substitution, which is consistent with references [86][117]. The reduction of the first anisotropy constant can be attributed to the change of magnetocrystalline anisotropy from uniaxial to planar as Co-Ti substitution increases, as a result of Ti^{4+} ions occupying the octahedral (12k) sites and Co^{2+} ions occupying the tetrahedral $4f_2$ sites and the trigonal bipyramid (2b) sites [85][106][8]. It should be noted that the analysis of the magnetisation curves was based on the Stoner-Wohlfarh model which describes the magnetisation curves of randomly distributed, single domain particles with a high uniaxial anisotropy, and has not taken into account the interaction between particles and the thermal effects, despite this it is widely used and has relevance to permanent magnets [84][118][119].

To investigate the temperature dependent magnetic properties, zero field cooled (ZFC) and field cooled (FC) measurements were performed for the samples with a 400 Oe applied field, between 4 K and 380 K, see figure (4.20).

For FC measurements, a 30 kOe field was applied during cooling. As can be seen, for x=0, a typical behaviour of ferrimagnetic M-type hexaferrite, in which the magnetisation curves of both ZFC and FC decrease with temperature, is observed, similar to the one measured at 100 Oe [117]. Both curves and their derivatives show an anomaly of magnetisation at (36 ± 2) K, marked with the blue rectangle in the figure (4.20-a). This observation was found in the magnetisation curve of FC mode only measured with 50 Oe and 100 Oe in [111]. In [111], the authors found a jumping behaviour in the magnetisation when measured in the ZFC mode between 258 K and 380 K. This behaviour was more pronounced in a low measuring field, 50 Oe, and was suppressed by increasing the measuring field or in FC mode. The authors summarised that this jump arises from the interactions among Fe^{3+} ions leading to a sudden switch of the moments which form a "metastable state" in a particular temperature range [111].

In this work, the ZFC data and the derivative show a very small jump measured with 400 Oe around (300 ± 2) K, marked by the arrow in figure (4.20-a), which could

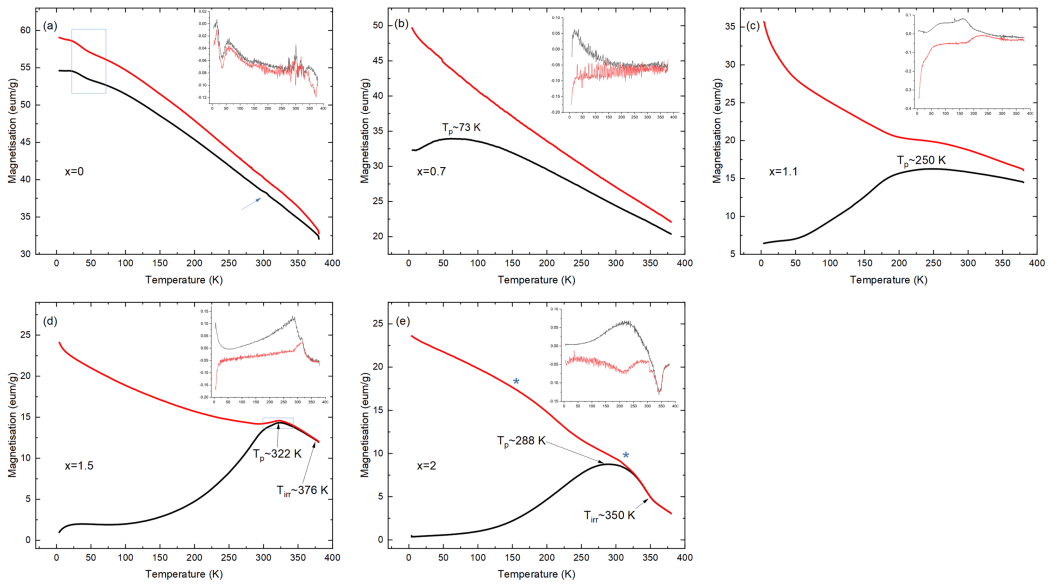

Figure 4.20: Field cooled (red line) and Zero field cooled (black line) as a function of temperature for (a) x=0, (b) x=0.7, (c) x=1.1,(d) x=1.5 and (e) x=2, measured with 400 Oe and the cooled in 30 kOe, for FC measurements. The derivative of ZFC (black line) and FC (red line) shown as inset.

be the observation of jumping behaviour. As the Co-Ti substitution is increased, the magnetisation curves of ZFC mode no longer follow the tendency of the FC curves. For x=0.7, the ZFC curve starts with a slight increase in magnetisation and develops a peak around (73 ± 3) K, before decreasing with temperature. The FC curve rapidly decreases with temperature. For x=1.1, the ZFC curve starts with a slight increase in magnetisation up to (52 ± 2) K then increases rapidly to reach maximum at T_p of (248 ± 4) K, then the magnetisation decreases gradually with temperature. This tendency is similar to that reported in [117] for x=1 in which the authors found $T_p \sim 230$ K when measured with 100 Oe applied field. For x=1.5 at low temperature, the magnetisation of the ZFC curve increases gradually until (34 ± 2) K followed by a region where the magnetisation levels off up to (83 ± 2) K. The magnetisation then increases reaching a maximum at (323 ± 2) K, before decreasing with temperature. Interestingly, the FC curve decreases with temperature up to (291 ± 3) K, then the magnetisation increases showing a cap at (323 ± 2) K, followed by decreasing with temperature, marked with the blue rectangle in figure (4.20-d). Clearly, the bifurcation of ZFC and FC magnetisation, T_{irr} was observed at (376 ± 3) K. For x=2, the magnetisation of the ZFC curve increases with temperature up to (290 ± 3) K, then decreases with temperature. The FC curve displays double broad peaks as the temperature increases, marked by the asterisks in figure (4.20-e). There is also a bifurcation of ZFC and FC magnetisation appearing at (340 ± 3) K.

Batlle *et al.*[85] observed a similar broad peak in M_{ZFC} curve of a small (superparamagnetic) particle system. The presence of the peak was associated with particle size distribution. In which the magnetic moment of each particle is randomly orientated along its easy magnetisation direction at temperature, T*. This temperature depends on the particle volume, anisotropy and orientation. Since, the samples contain crystallites that are distributed in volume, each crystallite is

blocked at a different temperature, T* which is not affected by the easy magnetisation direction in absence or in weak field. Hence, the observation of peak in the ZFC curve can be associated with the distribution of blocking temperature, F(T*) [85]. However, this explanation is not applicable to the results, since the average particle size of the samples ranges between 1000 nm and 1500 nm, which is much higher than the superparamagnetic limit and the estimated critical single domain size of BaM ferrite which is between 300 nm and 900 nm [8].

Another explanation of the presence of a peak in M_{ZFC} nanocrystalline powder is due to the competing effects of thermal agitation, the magnetisation decreases with temperature, and unpinning of the magnetic domain walls resulting from crystal imperfections leads to an increase in magnetisation due to the increase in thermal activation [120], which is more likely to explain the results. Moreover, many studies also suggest that the temperature, T_p corresponds to the transition from a collinear ferrimagnetic phase to a non-collinear (conical) magnetic phase, T_{cone} [14][45][16].

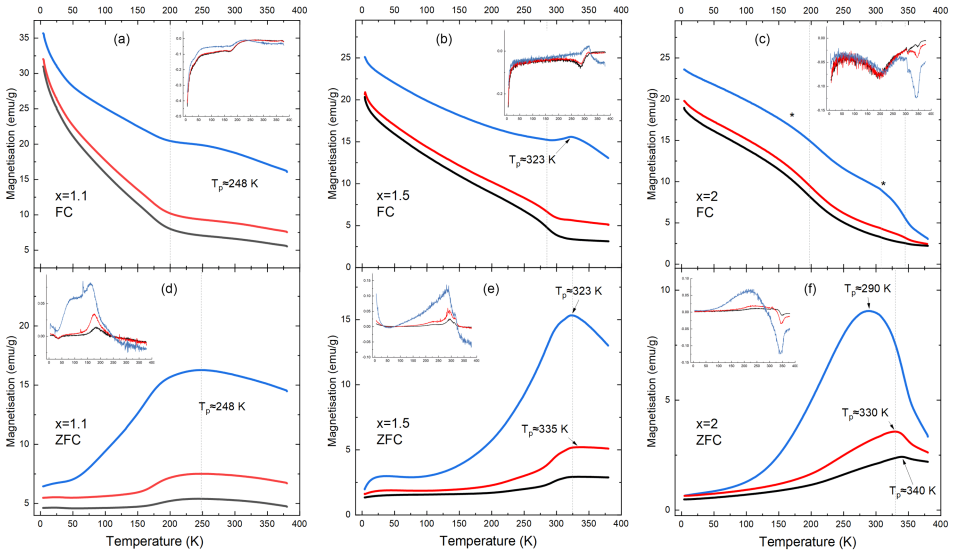

Figure 4.21: Field cooled (FC) and zero field cooled (ZFC) as a function of temperature for x= 1.1, 1.5 and 2, measured with 50 Oe (black line), 100 Oe (red line) and 400 Oe (blue line). For FC measurements, the samples were cooled in 30 kOe applied field. The derivative of ZFC and FC shown as inset.

To gain a further understanding of the magnetic structure, ZFC and FC measurements were performed with a lower applied field of 50 Oe and 100 Oe, for x=1.1, 1.5 and 2 and compared with data measured with 400 Oe, see figure (4.21). As shown in figure (4.21-a), the M_{FC} curves for x=1.1 decrease dramatically with the temperature up to (200 ± 4) K, and starts to develop a broad peak at (248 ± 4) K with a 400 Oe measuring field. Whereas the M_{ZFC} curves increase slowly up to (32 ± 3) K before developing a broad peak around (248 ± 4) K, as shown in figure (4.21-d). The stronger the applied field, the broader and higher the peak becomes. The M_{FC} curves for x=1.5 exhibits similar behavior to x=1.1, in which the magnetisation decreases dramatically with the temperature up to (285 ± 4) K, and develops a more pronounced peak at (323 ± 2) K with 400 Oe, see figure (4.21-b). As shown in figure (4.21-e), the M_{ZFC} curves increase with temperature and display a peak around (335 ± 3) K and (323 ± 3) K with 100 Oe and 400 Oe measuring field,

respectively. For x=2, the M_{FC} curves develop a peak in all measuring fields at (125 ± 3) K, marked with an asterisk in figure (4.21-c). In addition, a peak observed at (305 ± 3) K with 400 Oe measuring field, as shown in figures (4.21-c) and (4.20-e). In figure (4.21-f), the M_{ZFC} curves increase with temperature and show maximum magnetisation observed at (340 ± 3) K, (330 ± 2) K and (290 ± 3) K, with 50 Oe, 100 Oe and 400 Oe measuring field, respectively.

Clearly, the formation of the peak is more pronounced for those samples that contain a higher amount of (Co-Ti) substitution and becomes more pronounced with an increase in the measuring field. The maximum magnetisation is observed at a lower temperature with a higher measured field. It should be mentioned that the bifurcation of ZFC and FC magnetisation was observed only for x=2 and x=1.5 measured with 400 Oe. The observation of broad peak in M_{ZFC} curve can be associated with the formation of multi domains particles due to the relatively large particle size and the presence of imperfections and dislocations. These imperfections and defects (substitution of Co-Ti) interact with domains walls causing pinning and impedance to domain wall motion. The wall can be unpinned if the activation energy is supplied magnetically or thermally [121]. In ZFC, at very low temperature within each domain, the moments are locked into a particular direction due to the balance between exchange and anisotropy energies. By applying a weak magnetic field that can not unpin domains, the balance between energies will be disturbed and cause the moments to rotate slightly in favour of the field direction. By increasing the temperature, the thermal energy of magnetic moments increases causing them to precess about the field direction, hence the magnetisation reduces. However, since the applied field is fixed as the temperature increases, the thermal energy can unpin the domain walls causing a growth of the domains that are in the direction of the applied field, leading to an increase in the magnetisation [84][117]. Hence, we observed the distribution of pinning fields, due to the competition between the effect of thermal activation on the domain walls and thermal agitation in the presence of a weak field. In FC, since the samples had not reached the saturation magnetisation with the application of a 30 kOe applied field, at low temperature some domain walls still pinned, as the temperature increases, the thermal energy can activate the domain wall pinning causing an increase of the magnetisation. The peak position was plotted as a function of the applied field, see figure (4.22).

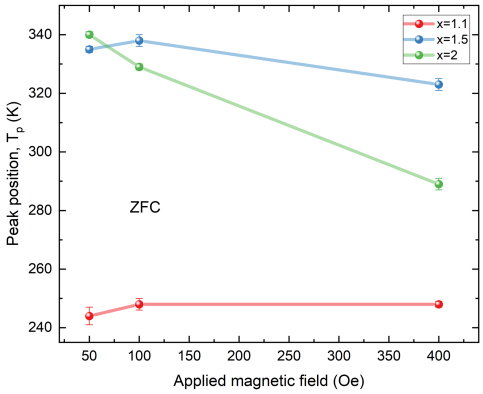

Figure 4.22: The peak position as a function of applied field for x=1.1, 1.5 and 2.

For ZFC curves measured at 50 Oe, the peak position is shifted to a higher tem-

perature as x increases, which agrees with reference [120][117], indicating a stronger domain walls pinning as Co-Ti substitution increases. As shown, the peak position for x=1.1, is not much affected by the strength of the measured field, whereas for x=1.5 and x=2, the peak position is shifted toward a lower temperature as the measured field increases. It could be interpreted that as the applied field increases, the activation energy required to unpin the domain wall reduces, therefore, the peak will be shifted towards a lower temperature, as reported for other magnetic systems [121].

4.5 Summary and Conclusions

$SrCo_xTi_xFe_{12-x}O_{19}$ polycrystalline samples with x= 0, 0.7, 1.1, 1.5 and 2 were prepared using the solid state method. The XRD measurements show that the samples exhibit M-type hexaferrite phase and impurity hematite phase less than 13%. The size of the coherently diffracting domains of the samples "the average particle size" of the samples range between 1000 nm and 1500 nm. Rietveld Refinement method was performed to confirm crystal structure and determine the lattice parameters and phases present. The results confirmed the presence of both M-type hexaferrite phase as the majority, and hematite phase as the minority with less than 13%. The results show a slight increase in the c-lattice parameter whilst the a-lattice parameter shows a marginal decrease as the Co-Ti substitution increases, this is in agreement with the literature [8][106]. The experimental data fits well with M-type hexaferrite structure. Improvement of the refinement process could be carried out by refining the occupancy site of Co and Ti ions, instead of making the assumption that Co and Ti ions occupy equally all sites, with the exception for x=0.7 where only the Fe ions enter the bi-pyramidal trigonal (2b) site. This could explain why the quality of the fit for x=0 and 0.7 are better than the rest. SEM images show that the samples exhibit agglomerations of small particles with a hexagonal and plate-like shape. The EDS elemental analysis confirm that the substitution of Co and Ti ions for Fe ion increases in all samples with an excess of Fe and O elements more than stoichiometry for M-type hexaferrite, supporting the presence of the second phase Fe_2O_3.

The magnetic properties of the M-type hexaferrite samples were investigated using VSM magnetometer. The results show that $SrFe_{12}O_{19}$ exhibit typical behaviour of ferrimagnetic M-type hexaferrite, and as the Co-Ti substitution was introduced, the saturation magnetisation and remanent magnetisation decreased gradually. The reduction in the magnetisation can be attributed to replacing Fe^{3+} ions with non magnetic Ti^{4+} ions and Co^{2+} ions, which have a smaller moment [106]. Moreover, the coercive field decreases dramatically with Co-Ti substitution, which can be explained by the tendency of Co^{2+} ions to occupy the tetrahedral $4f_2$ and trigonal bipyramid (2b) sites, leading to a non-collinear magnetic structure and the development of cone magnetisation [8]. As the amount of Co-Ti substitution increases further, the magnetocrystalline anisotropy constant, K_1 reduces, suggesting that the magnetocrystalline anisotropy gradually changes from uniaxial to planar anisotropy as a result of Ti^{4+} ions occupying the octahedral (12k) sites and Co^{2+} ions occupying both the tetrahedral $4f_2$ sites and the trigonal bipyramid (2b) sites [85][106][8]. Interestingly, the wasp-waisted hysteresis loop was observed for x=1.5 and 2, at low temperature up to 250 K, which can be attributed to the substitution of the

Co-Ti ions at different sites within the lattice. Temperature dependence of the magnetisation measurements reveal that when the Co-Ti substitution was introduced, a broad peak developed in the ZFC curve, this is most likely to be associated with the different distribution of domain wall pinning. The occurrence of the peak can be explained by competition between effects of thermal agitation and the unpinning of the magnetic domain walls, in which the former tends to reduce magnetisation while the latter tends to increase the magnetisation as the temperature increases. The results show that the peak position is sensitive to the strength of the applied field, as the applied field increases the peak position is shifted towards lower temperatures. The peak shape is also sensitive to the amount of Co-Ti substitution, as the substitution rate increases the peak is more pronounced and shifted towards a lower temperature with higher field. This could be due to an increase of domain wall pinning as Co-Ti substitution increases [117]. More measurements need to be carried out at a various range of applied fields in order to investigate the evolution of maximum magnetisation with Co-Ti substitution further.

Chapter 5

$SrCo_2Ti_2Fe_8O_{19}$ Single Crystal

In this chapter, the structural and magnetic characterisation of $SrFe_{12}O_{19}$ and $SrCo_2Ti_2Fe_8O_{19}$ single crystals will be given, where the substitution induced magnetic anisotropy changes from uniaxial to planar anisotropy. The discussion starts with the growth method, followed by the structural characterisation, X-ray diffraction and the magnetic properties of the samples using VSM-SQUID magnetometer.

5.1 Single crystals growth using Float Zone (FZ)

Single crystals of $SrFe_{12}O_{19}$ and $SrCo_2Ti_2Fe_8O_{19}$ were grown by the float zone method. Polycrystalline feed and seed rods were made by solid state reaction, see section (4.1). The starting materials were mixed and ground for 4 h in acetone at 350 rmp. The resulting product of polycrystalline material was transferred into an alumina ceramic boat and sintered at 1000 ℃ for 10 h under atmospheric oxygen pressure. The resultant material was mixed with PVA and pressed, using an in house developed hydrostatic press system, under 10 tons to form rods with a diameter of 4 mm and a length of 60 mm. Later, the rods were placed in an alumina ceramic boat and sintered for a second time at 1300 ℃ for 10 h under a flowing atmospheric oxygen pressure. Crystal growth was performed using the optical floating zone furnace, (Crystal Systems Corporation), situated at Durham University. The growth process carried out with 500 W lamps under 7 bar oxygen pressure.

Figure (5.1) illustrates the growth steps and formation of a molten zone. As shown, the rod tips were melted, which can be recognised by their shiny appearance. As soon as the melted rod tips formed liquid droplets, the feed rod was lowered to join together with the seed rod and form a column of molten material. When the growth terminated, the power of the lamps was reduced allowing the molten zone to cool down, meanwhile, the feed rod was moved upward for separation.

The growth rate was 4 mm/h and the rotation speed of the feed and the seed were 20 rpm. The grown crystals were obtained as cylinders with a diameter $\sim$ 3.8 mm and a length $\sim$ 20.2 mm, see figure (5.2). The growth direction was almost perpendicular to the c-axis, which is consistent with that previously reported [122]. The initial stages of crystal growth are mixed phases, the single phase growth was found around $\sim$ 13.5 mm from the end of growth. This is expected as Balbashov.(2017) obtained M-type hexaferrite single phase growth after $\sim$ 15 mm with a growth rate of 5-10 mm/h [53].

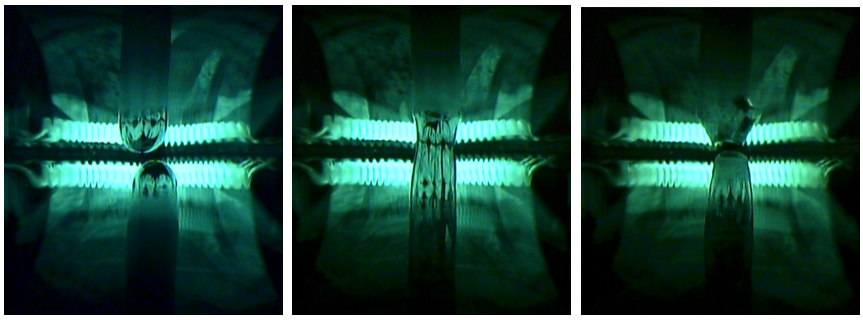

Figure 5.1: Single crystal growth by FZ method. From left to right, the melted rod tips, joined rods forming melting zone, and separation between the feed rod and the grown crystal.

The crystals were cut and polished with the c-axis perpendicular to the surface plane. The specimens had dimension ($2.72\,mm \times 1.7\,mm \times 0.83\,mm$) and ($2.5\,mm \times 2.7\,mm \times 1.5\,mm$) for $SrFe_12O_{19}$ and $SrCo_2Ti_2Fe_8O_{19}$ crystals, respectively.

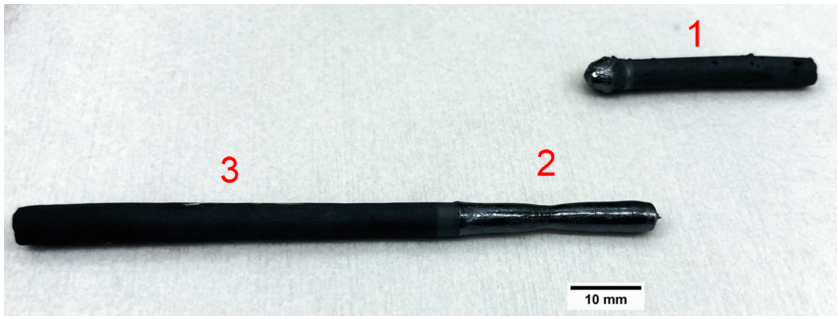

Figure 5.2: The result of $SrCo_2Ti_2Fe_8O_{19}$ crystal growth using FZ method. (1) The polycrystalline feed rod followed by quenched molten zone. (2) Quenched molten zone, followed by the grown single crystal. (3) The polycrystalline seed rod.

In order to polish the crystals, brass jigs were manufactured to insure the specimens were held rigidly and flat during the polishing process. The specimens were mounted on the jig using melted dental wax. The polishing procedure was as follow: polish the specimen with P1200 wet and dry paper on a flat surface, and spray liberally with Kemet OS lubricating fluid using a forward and back motion. Once a satisfactory result was achieved, the sample and jig were thoroughly cleaned using isopropyl alcohol and technicloth (non woven wipes). Then the above procedure was repeated using P1500, P2000 and P2500 silicon carbide abrasive paper. Later, the sample (with jig) was mounted on an optical polisher and polished for 10 min using 6 Micron diamond compound, the sample and jig were thoroughly cleaned using isopropyl alcohol and technicloth (non woven wipes) to remove all diamond compound. Then the above steps were repeated using 3 micron, 1 micron, and $\frac{1}{4}$ micron diamond compound, ensuring the sample and jig were thoroughly cleaned to remove all diamond compound before proceeding to the next stage, see figure (5.3).

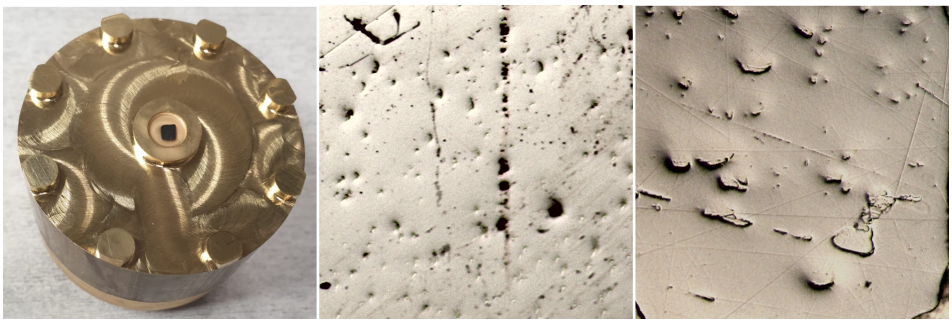

Figure 5.3: From left to right, the $SrCo_2Ti_2Fe_8O_{19}$ single crystal mounted on the brass jig, the polished $SrCo_2Ti_2Fe_8O_{19}$ single crystal, and the $SrFe_{12}O_{19}$ polished single crystal.

5.2 Crystal structure

The orientation of the crystals were determined using a MWL120 Real-Time-Back-refraction Laue camera system at Durham University, and tungsten X-ray tube operated at 7 kV and 12 mA. Figure (5.4) shows that the crystals exhibit hexagonal Laue diffraction patterns around [0 0 1] direction, Miller index. The black Laue dots could be indexed to ($P6_3/mmc$) space group, using the Cologne Laue Indexation Program (CLIP)[123]. The green and pink dots are a simulation of Laue patterns for $SrFe_{12}O_{19}$ and $SrCo_2Ti_2Fe_8O_{19}$, respectively.

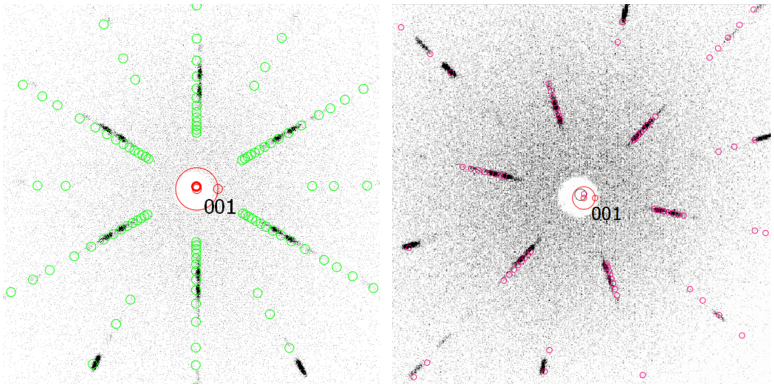

Figure 5.4: Laue diffraction pattern for single crystals, $SrFe_{12}O_{19}$ (on the left) and $SrCo_2Ti_2Fe_8O_{19}$ (on the right). The green and pink dots are a simulation of Laue patterns using ($P6_3/mmc$) space group and lattice parameters.

($2\theta - \omega$) measurements were performed for both crystals and are shown in figure (5.5). The presence M-type hexaferrite phase was confirmed by the observation of sharp and high (0 0 2n) reflections. $SrFe_{12}O_{19}$ shows an extra peak of very low intensity around 32.2° marked with an asterisk which is highly likely to be an impurity. The c-lattice parameter was obtained using equation (3.15). The c-lattice parameter was (23.07 ± 0.02)Å and (23.09 ± 0.01)Å for $SrFe_{12}O_{19}$ and $SrCo_2Ti_2Fe_8O_{19}$, respectively, consistent with reference [53].

To gain an insight into the quality of the crystals, rocking curve measurements were performed on (0 0 8) reflection, shown as inset. The peak was fitted using Voigt function with FWHM was $(0.023 \pm 0.001)°$ and $(0.02 \pm 0.002)°$ for $SrFe_{12}O_{19}$ and $SrCo_2Ti_2Fe_8O_{19}$, respectively. These value are very small indicating good quality

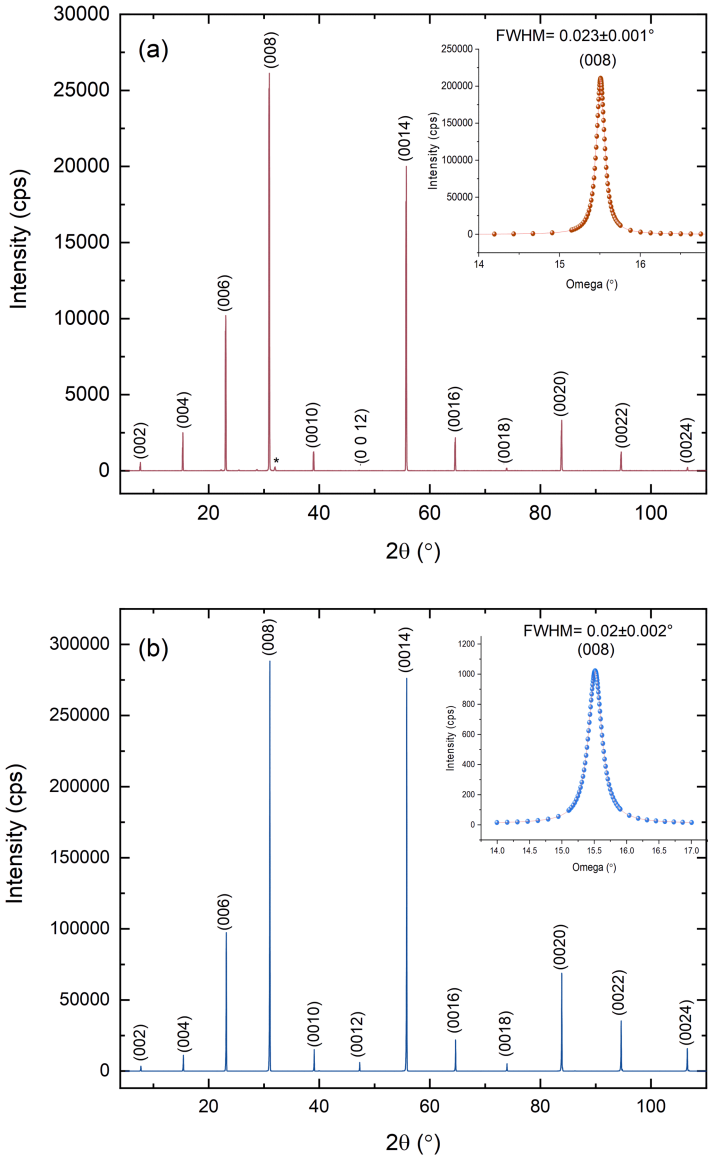

Figure 5.5: XRD pattern for single crystals. (a) $SrFe_{12}O_{19}$, (b) $SrCo_2Ti_2Fe_8O_{19}$, with Miller index labeled for observed hexaferrite diffraction peaks. Rocking curve measurement (red and blue balls) and Voigt fit (red line) for (0 0 8) reflection shown as inset.

crystals. For $SrFe_{12}O_{19}$, the Lorentzian and Gaussian widths were $(0.018 \pm 0.002)°$ and $(0.011 \pm 0.003)°$, respectively, whereas for $SrCo_2Ti_2Fe_8O_{19}$ the Lorentzian and Gaussian widths were $(0.016 \pm 0.003)°$ and $(0.012 \pm 0.003)°$, respectively, indicating that the value of FWHM is intrinsic broadening in the material, since the instrumental broadening is small.

5.3 Magnetic properties

The magnetisation curves for $SrFe_{12}O_{19}$ and $SrCo_2Ti_2Fe_8O_{19}$ crystals were measured at various temperatures by applying the field along [0001] (the c-axis) and [10$\bar{1}$0] directions (ab-plane), see figure (5.6) and (5.7), respectively. The measurements were corrected for the demagnetisation field using equation (2.12), with N≈1 and 0 for applied field along and perpendicular to the c-axis, respectively. The hysteresis loops of $SrFe_{12}O_{19}$ display a typical behaviour of uniaxial crystal

anisotropy, in which the hexagonal c-axis is the easy magnetisation axis and the ab-plane is the hard magnetisation direction, similar to the one found in [124]. Since the crystals were not fully saturated with 30 kOe applied field in both directions, the value of saturation magnetisation was estimated using (LAS), equation (3.46). As shown, the saturation magnetisation of the sample differs slightly when applying the field along the c-axis and ab-plane. This could be due to the fact that the calibration was only carried out in-plane geometry. The value of saturation magnetisation was taken by the average of both measurements, which explains the large error in M_s value.

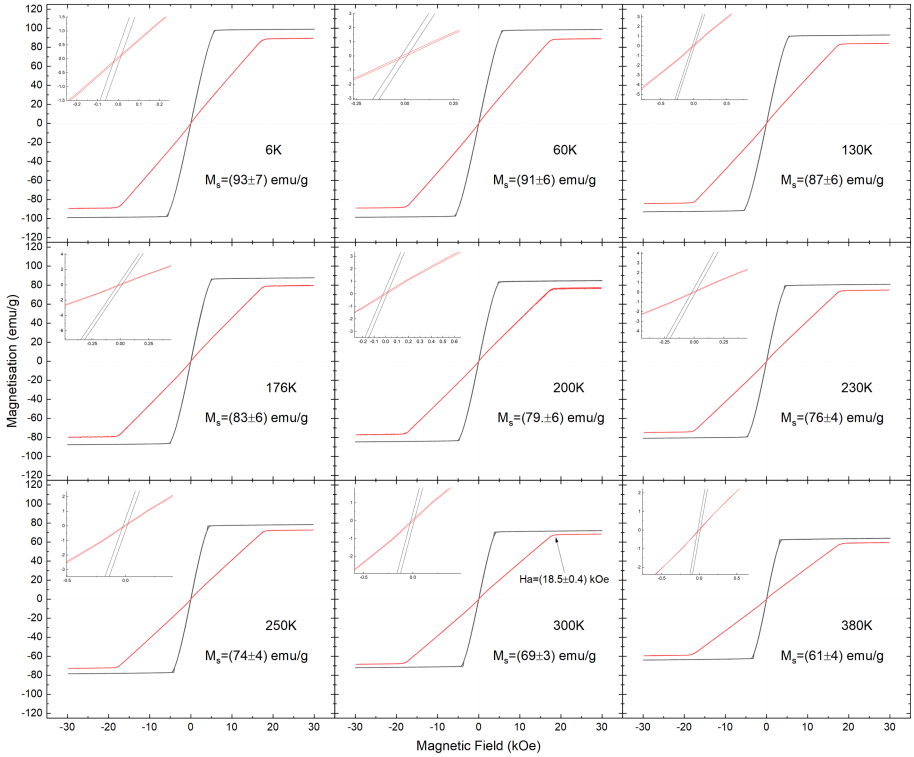

Figure 5.6: M-H loop for $SrFe_{12}O_{19}$ at various temperatures. The black curves represent the measurement for $H \parallel$ c-axis and the red curves represent the measurement for $H \parallel$ ab-plane.

The anisotropy field, H_a, was determined from magnetisation curves, at the intersection of the easy and hard axis, i.e. $H \parallel$ c-axis and $H \parallel$ ab-plane, marked by the arrow in figure (5.6)[125][126]. The value of anisotropy field was around (18.5 ± 0.4) kOe, which is similar to the one reported in reference, H_a was 20 kOe [8].

The hysteresis loop for $SrCo_2Ti_2Fe_8O_{19}$ at various temperatures are given in figure (5.7). Interestingly, $SrCo_2Ti_2Fe_8O_{19}$ shows wasp-waisted hysteresis loop for $H \parallel$ ab-plane measurements from low temperatures up to 250 K, and then begins to disappear as the temperature is increased above this temperature. Whereas with $H \parallel$ c-axis, no distinct behaviour was found. Moreover, at low temperature, the initial curve lies outside of the subsequent hysteresis, up to 200 K. As the temperature increases, the initial curve is partially observed outside of the loop up to (1800 ± 100) Oe at 230 K and (500 ± 200) Oe at 250 K and 300 K, suggesting that the crystal could have a non-collinear magnetic structure [127].

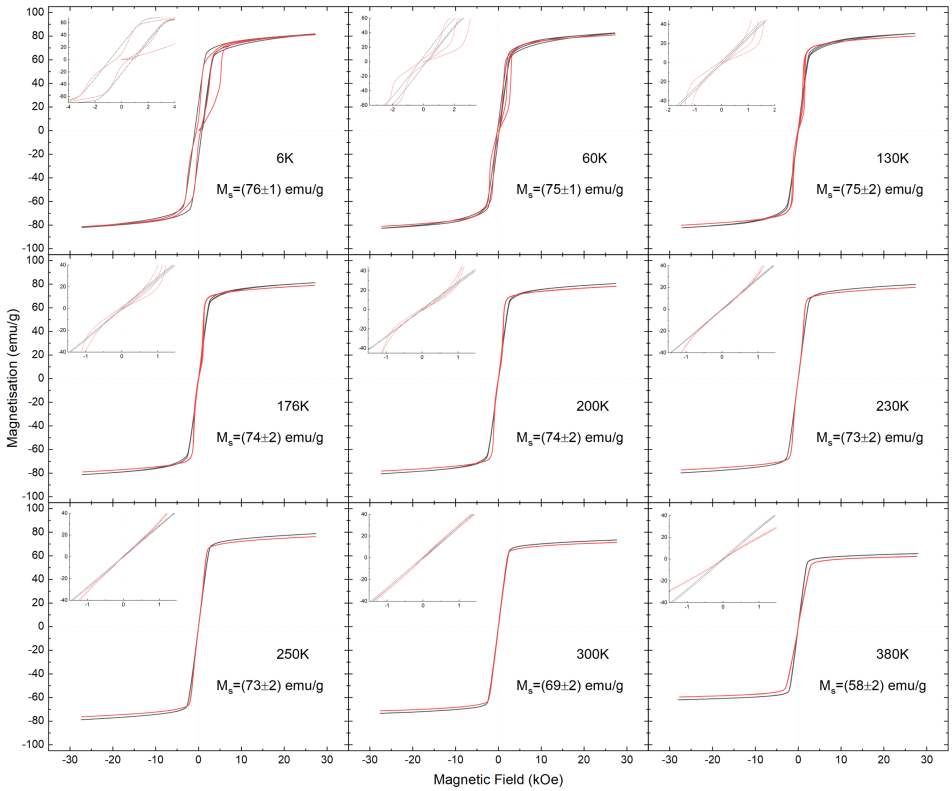

Figure 5.7: M-H loop for $SrCo_2Ti_2Fe_8O_{19}$ at various temperatures. The black curves represent the measurement for $H \parallel c-axis$ and the red curves represent the measurement for $H \parallel ab-plane$.

The saturation magnetisation value for both crystals decreases with temperature, see figure (5.8). The saturation magnetisation for $SrFe_{12}O_{19}$ and $SrCo_2Ti_2Fe_8O_{19}$ was (93 ± 7) emu/g, (76 ± 1) emu/g at 6 K, and decreased to (61 ± 4) emu/g, (58 ± 2) emu/g at 380 K, respectively. At room temperature, the saturation magnetisation for $SrFe_{12}O_{19}$ was (69 ± 3) emu/g, which is consistent with ref [128], (74.3) emu/g, whereas for $SrCo_2Ti_2Fe_8O_{19}$ the saturation magnetisation was (69±2) emu/g which is much higher than reported ($\sim$ 28) emu/g for x=2 [53]. Comparing this result with the $SrCo_xTi_xFe_{12-x}O_{19}$ samples in the previous chapter, the large difference in the saturation magnetisation may imply that there is a difference between the nominal and actual Co-Ti substitution for the $SrCo_xTi_xFe_{12-x}O_{19}$ crystal.

In order to determine the composition of the crystal, EDS measurements were performed on several sites, with a beam energy of 25 keV and 7 nA probe current. The measured composition was $Sr_{1.2}Co_{1.2}Ti_{1.6}Fe_{9.2}O_{19}$ with an error of (±0.03) implying Co-Ti deficiency, which could explain the high value of M_s. The saturation magnetisation of the measured composition is close to the one reported for x=1.1 [53][8], and x=1.1 polycrystalline sample in the previous chapter. Interestingly, the initial M-H curve lies outside of the subsequent hysteresis loop, for T <250 K, providing further evidence that the crystal could have a non-collinear magnetic structure [127].

Considering that magnetic anisotropy affects the shape of the loop, further analysis was performed on magnetisation curves to evaluate the MCA constants using

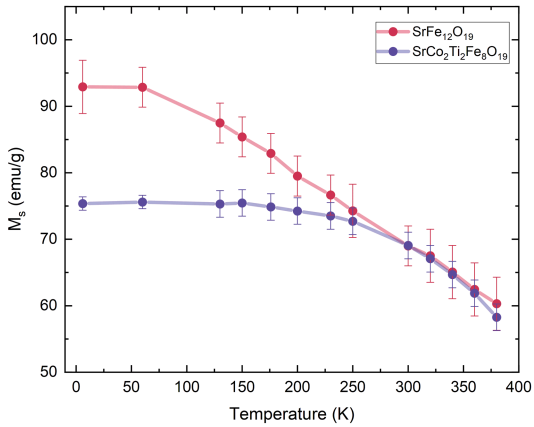

Figure 5.8: The saturation magnetisation for $SrCo_2Ti_2Fe_8O_{19}$ and $SrFe_{12}O_{19}$ at various temperatures.

Sucksmith-Thompson method [129], which is valid for the magnetisation curve of uni-axial single crystal obtained in comparatively small fields applied perpendicular to the easy magnetisation direction [125]. In this method, the total magnetic free energy is the sum of MCA energy and external field energy (Zeeman energy) with H applied along ab-plane, given by:

$$E_{total} = E_a + E_{ext.field} \tag{5.1}$$

For a hexagonal system, the MCA energy is given in equation (2.11).

$$E_a = K_0 + K_1 \sin^2\theta + K_2 \sin^4\theta + K_3 \sin^6\theta + \dots$$

where K_0 is the isotropic and K_1, K_2 and K_3 are anisotropy constants, θ is the angle between magnetisation and the c-axis. K_0 is independent of angle, and is usually ignored. The total magnetic free energy can be presented as:

$$E_{total} = K_1 \sin^2\theta + K_2 \sin^4\theta + K_3 \sin^6\theta - M_s H_{app} \sin\theta \tag{5.2}$$

Minimising E_{total} with respect of the angle (θ), and rearranging, gives:

$$\frac{H_{app}}{M} = \frac{2K_1}{{M_s}^2} + \frac{4K_2}{{M_s}^4} M^2 + \frac{6K_3}{{M_s}^6} M^4 \tag{5.3}$$

Further details can be found in appendix (D). By plotting (H_{app}/M) vs (M^2) and fitting, K_1, K_2 and K_3 constants can be obtained. The values of K_1 and K_2 are taken from the intercept in the y-axis and the slope, respectively [130]. K_3 is usually very small compared with K_1 and K_2, and is often negligible[130][23][19][126].

The values of anisotropy constants K_1 and K_2 for the crystals were obtained using equation (5.3). The fitting was performed in the field region between 400 Oe and 8600 Oe and plotted as a function of temperature, see figure (5.9). For $SrFe_{12}O_{19}$, the values of K_1 and K_2 at room temperature were $(5.71 \pm 0.03) \times 10^5\ erg/g$ and $(0.26 \pm 0.02) \times 10^5\ erg/g$, respectively, indicating a very high anisotropy along the c-axis. This value is close to that of [8] which was K_1 of $(3.5 \times 10^6)\ erg/cm^3 \approx (6.8 \times 10^5)\ erg/g$. As the temperature increases, the value of K_1 decreases, similar

to the behaviour in ref [131] with K_2 nearly constant. Whereas for $SrCo_2Ti_2Fe_8O_{19}$, the value of K_1 and K_2 at room temperature were $(0.25 \pm 0.02) \times 10^5\ erg/g$ and $(0.05 \pm 0.04) \times 10^5\ erg/g$, respectively, suggesting that the axial anisotropy reduced with Co-Ti substitution. This value is larger than the one reported for $BaCo_{1.1}Ti_{1.1}Fe_{9.8}O_{19}$ [132], which is expected as $SrFe_{12}O_{19}$ has slightly higher magnetic properties than $BaFe_{12}O_{19}$ [131][8].

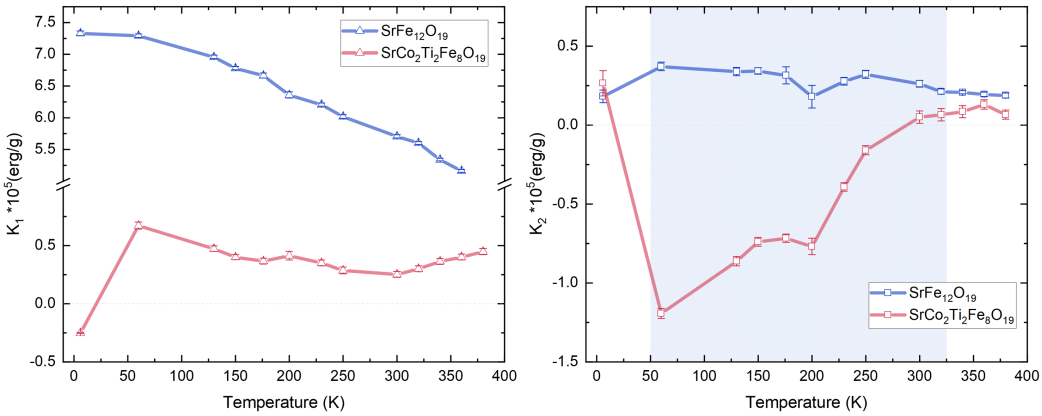

Figure 5.9: The anisotropy constants for $SrFe_{12}O_{19}$ and $SrCo_2Ti_2Fe_8O_{19}$ at various temperatures.

To understand the effect of the signs K_1 and K_2 to the anisotropy energy, $E_a = K_1 \sin^2\theta + K_2 \sin^4\theta$, was plotted, from 0 to 2π, see figure (5.10). As can be seen, when both K_1 and K_2 are positive, the energy is minimised at $\theta = 0,\ \pi$ implying that the c-axis is the easy magnetisation direction, see (5.10-a). If both K_1 and K_2 are negative, E_a is minimised at $(\theta = \frac{\pi}{2})$, implying that the ab-plane is the easy magnetisation direction, see (5.10-b). The energy is also minimised at $(\theta = \sin^{-1}(\frac{-K_1}{2K_2})^{0.5})$. This solution is only possible when $(0 < \frac{-K_1}{(2K_2)} < 1)$, which corresponds to an easy cone magnetisation, see (5.10-c) [133][126]. As can be seen, K_1 and K_2 are positive for $SrFe_{12}O_{19}$. Since, $(K_1 + K_2 > 0)$, the energy is minimised at $\theta = 0,\ \pi$, therefore, the preferred magnetisation direction will be along the c-axis, i.e uniaxial anisotropy, as reported [131][21].

However, (Co-Ti) substitution reduces the anisotropy constants. This could be due to the tendency of Ti^{4+} (non-magnetic) ions to occupy (12k) octahedral sites which interrupts the magnetic interactions in a such way that the two blocks RS and R^*S^* become magnetically decoupled. In addition, the tendency of Co^{2+} ions to occupy $(4f_1)$ tetrahedral sites, and trigonal bi-pyramidal sites for (x≥0.8), which is thought to lead to a reduction of an uniaxial anisotropy becoming planar anisotropy. As a result of the two sources a conical non-collinear magnetic structure may form [132][16][134]. For $SrCo_2Ti_2Fe_8O_{19}$ crystal, the sign of K_1 is negative and K_2 is positive at 6 K, indicating the magnetisation direction forms an easy cone with half angle θ of $(44 \pm 7)°$, which is close to the one determined from neutron diffraction for $BaCo_{1.1}Ti_{1.1}Fe_{9.8}O_{19}$ [132]. Interestingly, as the temperature increases, the sign for K_1 changes from negative to positive and the sign for K_2 changes from positive to negative between 50 K and 250 K, before turning back to positive above 250 K. The anisotropy energy was plotted for data taken at 150 K, see (5.10-d). As can be seen, as temperature increases, the system has a more complicated state, than

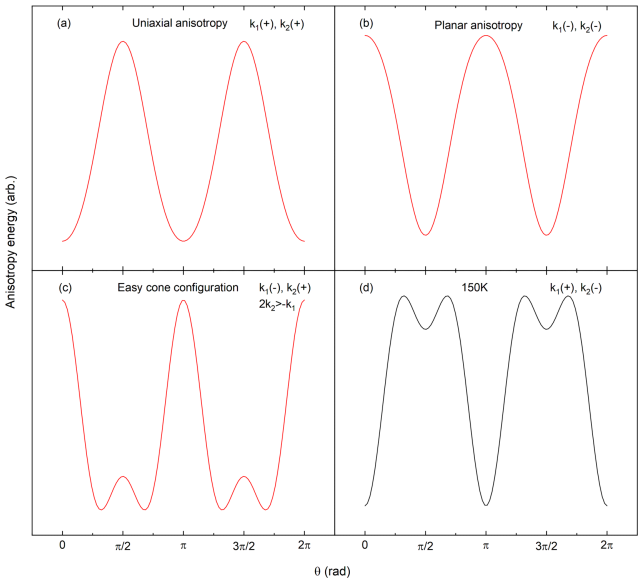

Figure 5.10: Variation of anisotropy energy as a function of the angle (θ). (a) Uniaxial anisotropy, (b) Planar anisotropy, (c) Easy cone configuration and (d) The value of K_1 and K_2 for $SrCo_2Ti_2Fe_8O_{19}$ at 150 K.

just uniaxial and planar anisotropy. Despite, ($K_1 > 0$), the ratio ($|\frac{K_1}{K_2}|<2$), and ($0 < \frac{-K_1}{(2K_2)} < 1$) between 60 K and 230 K, suggesting that the system could develop an easy cone magnetisation at this range of temperatures. The value of anisotropy constants K_1 and K_2, along with their corresponding half angle of easy cone, θ are given in table (5.1).

Table 5.1: The calculated anisotropy values for $SrCo_2Ti_2Fe_8O_{19}$ single crystal extracted from fitting of the magnetisation curves using Sucksmith and Thompson method.

Temperature (K)	K_1 ($10^5\ erg.g^{-1}$)	K_2 ($10^5\ erg.g^{-1}$)	Angle (°)
6	-0.25 ± 0.01	0.26 ± 0.08	44 ± 7
60	0.67 ± 0.03	-1.19 ± 0.03	32 ± 2
130	0.47 ± 0.02	-0.86 ± 0.03	32 ± 2
150	0.4 ± 0.02	-0.74 ± 0.03	31 ± 2
176	0.37 ± 0.02	-0.72 ± 0.03	30 ± 3
200	0.41 ± 0.04	-0.77 ± 0.05	31 ± 3
230	0.35 ± 0.03	-0.4 ± 0.03	42 ± 5
250	0.29 ± 0.03	-0.16 ± 0.03	71 ± 15

These results agree with the torque measurement on $BaCo_1Ti_1Fe_{10}O_{19}$ at room temperature, the cone angle was 61° from the c-axis [135]. In addition, Kreisel *et al.* performed neutron diffraction and magnetisation curve measurements on $BaCo_xTi_xFe_{12-2x}O_{19}$ single crystals with (x=0, 0.4, 0.8 and 1.1), and found that for crystals with (x>0.8) a conical magnetic structure is observed at room temperature. For x=0.8, the cone angle was 25°, with ($K_1 = 0.65 \times 10^5$) erg/g, ($K_2 = 0.32 \times 10^5$) erg/g, and ($K_3 = 0.51 \times 10^5$) erg/g, whereas for x=1.1, the cone angle was 40°, with

($K_1 = -1.02\times10^5$) erg/g, ($K_2 = 0.69\times10^5$) erg/g, and ($K_3 = -23\times10^5$) erg/g [132].

Moreover, the shape anisotropy is temperature dependant [136]. Bottoni. (1997) investigated the magnetic ansitropy for $BaFe_{12}O_{19}$ and $BaCo_{0.85}Ti_{0.85}Fe_{10.3}O_{19}$ at low temperature. This study points out the conflict between the magnetocrystalline and the shape anisotropies, in which the easy axis of shape anisotropy (ab-plane) is a hard axis for the magnetocrystalline anisotropy and vice versa. The total anisotropy energy is defined as:

$$E_{total} = E_k + E_s = (K_1 - K_s)\sin^2\theta + K_2\sin^4\theta + const. \tag{5.4}$$

where $E_s = K_s\sin^2(\pi/2-\theta)$ is the shape anisotropy energy and ($K_s = \frac{1}{2}NM^2$) is the shape anisotropy constant. M is magnetisation, and N is the difference between the demagnetising factors in the hard (c-axis) and easy (ab-plane) directions. Hence, K_s varies with the temperature due to the variation of magnetisation with temperature. The author found out that for $BaFe_{12}O_{19}$, K_1 is positive and larger than K_s at all temperatures, implying the magnetic anisotropy is along the c-axis and perpendicular to ab-plane. Whilst, for $BaCo_{0.85}Ti_{0.85}Fe_{10.3}O_{19}$, $(K_1 - K_2)$ is positive at room temperature and negative at low temperature, 90 K, indicating that the magnetic anisotropy is not uniaxial and forms a cone angle of 24.5°to the c-axis [137].

Therefore, based on Kreisel *et al.* work, there is the possibility of having a conical non-collinear magnetic structure where K_1 is positive. However, it is worth noting that there are limitations in the Sucksmith and Thompson method, firstly it assumes the value of M_s is constant in an increasing magnetic field [138]. Secondly, that the K_1 value is sensitive across the range of fitting field [139]. In addition, substantial errors may arise from not taken into account K_3, which may affect the results. Thus, magnetisation curve analysis show a signature of non-collinear magnetic structure at low temperature. Torque measurements may give a better accuracy to estimate the anisotropy constants.

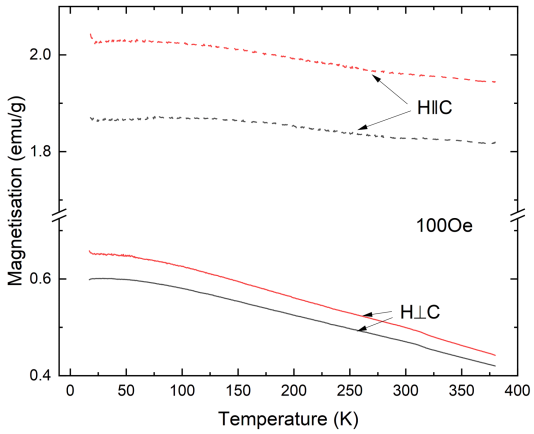

Figure 5.11: FC (red) and ZFC (black) measurements for $SrFe_{12}O_{19}$ single crystal measured with 100 Oe along (dash line) and perpendicular (solid line) to the c-axis.

To investigate the temperature dependent magnetic properties of the crystals further, field cooled (FC) and zero field cooled (ZFC) measurements have been performed. Figure (5.11) shows ZFC and FC curves for $SrFe_{12}O_{19}$ single crystal measured in a 100 Oe applied field and cooled in a 30 kOe field, applied along

and perpendicular to the c-axis. As can be seen, the crystal exhibits typical behaviour of a ferrimagnetic M-type hexaferrite, in which the magnetisation decreases linearly with the temperature, similar to the observed polycrystalline sample, x=0. The magnetisation along the c-axis is higher than the ab-plane implying that the c-axis is the easy magnetisation axis. Whereas the situation is different for the $SrCo_2Ti_2Fe_8O_{19}$ crystal, see figure (5.12). For FC measurements, with H_c, the magnetisation decreases as the temperature increases, and no anomalous behaviour was observed, for all values of the measuring field. Whereas, with H_{ab}, the magnetisation curves decrease with an increase in temperature up to 100 K, then as the measured field is increased, the magnetisation starts to develop doubled peaks at, (182 ± 4) K and (279 ± 3) K with 400 Oe.

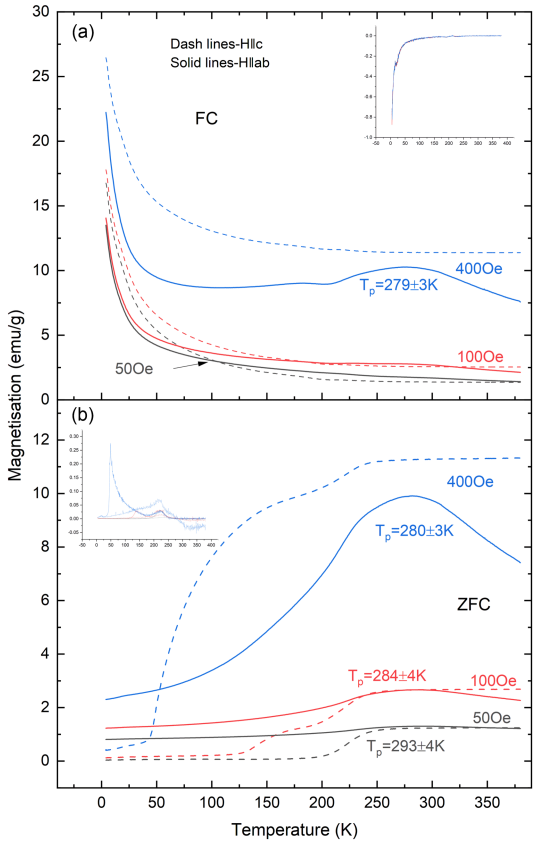

Figure 5.12: M(T) measurements for $SrCo_2Ti_2Fe_8O_{19}$ single crystal, (a) FC and (b) ZFC measurements at various measuring fields applied along H_c (dash line) and H_{ab} (solid line). The derivative of measurements shown as inset.

For ZFC measurements, the magnetisation curves are more complicated and sensitive to the applied field. For H_{ab}, the M_{ZFC} curve, measured with 50 Oe reaches the maximum at (293 ± 4) K then levels off, whereas for 100 Oe and 400 Oe, the maximum was reached at (284 ± 4) K and (280 ± 3) K, before the magnetisation dropped. As the measured field increases, the maximum temperature, T_p, shifts slightly towards a lower temperature. Turning point occurs at (220 ± 3) K, for all values of the measuring field. Whereas with H_c, the magnetisation curves become more complicated with an increase in the measured field. The maximum magnetisation occurs at (310 ± 3) K, (290 ± 3) K and (255 ± 3) K for 50 Oe, 100 Oe and 400 Oe, respectively, after which the magnetisation levels. There are two additional

turning points that occur as the measuring field increases. The first point occurs at (17 ± 2) K for both 100 Oe and 400 Oe. The second point occurs at (140 ± 3) K and (50 ± 2) K for 100 Oe and 400 Oe, respectively. Clearly the phase between 50 K and 250 K is dependent on the applied field, as the applied field gets stronger the maximum change in magnetisation occurs at a lower temperature and the peak gets broader, see the inset on figure (5.12).

The observation of the T_p could be due to the formation of multi domains configuration in doped crystal as a result of crystalline imperfections and dislocations. These imperfections and defects (substitution of Co-Ti) interact with domain walls causing pinning and impedance to domain walls motion. The wall can be unpinned if the activation energy is supplied magnetically or thermally [121]. In ZFC, at very low temperature within each domain, the moments are locked into a particular direction due to the balance between exchange and anisotropy energies. By applying a weak magnetic field that is insufficient to unpin domains, the balance between energies will be disturbed and cause the moments to rotate slightly in favour of the field direction. By increasing the temperature, the thermal energy of the magnetic moments increase causing them to precess about the field direction, hence the magnetisation reduces. However, since the applied field is fixed as the temperature increases, the thermal energy can unpin the domain walls causing a growth of the domains that are in the direction of the applied field, leading to an increase in magnetisation [84][117]. Hence, we observed the distribution of pinning fields, due to the competition between the effect of thermal activation of the domain walls and thermal agitation in the presence of a weak field.

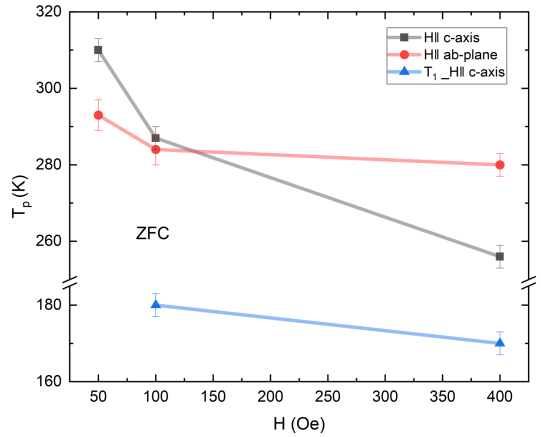

Figure 5.13: The peak position of $SrCo_2Ti_2Fe_8O_{19}$ single crystal as a function of the applied fields along H_c (black line) and H_{ab} (red line).

The temperature at which the magnetisation is maximum, T_p, was plotted as a function of the applied field, see figure (5.13). As can be seen, T_p as well as T_1 decrease with an increase in the applied field, which is consistent with the results in the previous chapter. This temperature, T_p, is considered as the magnetic phase transition point from a non-collinear to a collinear magnetic structure as the temperature increases [140][14]. Zhang.(2018) observed a similar trend for $SrSc_{1.8}Fe_{10.2}O_{19}$ with a wider range of fields suggesting that the reduction of T_p could be due to the change of the Fe-O-Fe bond angle with the applied field effecting the stability of the conical magnetic structure, therefore T_p decreases [141]. Unfortunately, due to

the limited range of fields and measurements, it is impossible to verify with Zhang therefore more work needs to be carried out in order to investigate how the strength of the magnetic field alters the crystal structure.

5.4 Summary and Conclusions

A successful growth of high quality single crystals of M-type hexaferrite $SrFe_{12}O_{19}$ and $SrCo_2Ti_2Fe_8O_{19}$ have been achieved using the float zone method. The XRD analysis confirmed the presence of M-type hexaferrite crystal structure. The magnetic properties of the crystals were obtained using VSM magnetometer. The magnetisation curve analysis show that $SrFe_{12}O_{19}$ single crystal displays typical behaviour of uniaxial crystal anisotropy, in which the hexagonal c-axis is the easy magnetisation axis and the ab-plane is the hard magnetisation axis. However, the situation is somewhat different for $SrCo_2Ti_2Fe_8O_{19}$ single crystal which shows wasp-waisted hysteresis loop only at low temperatures H_{ab} measurements up to 250 K, implying a complex non-collinear structure. The values of anisotropy constants K_1 and K_2 for the crystals were evaluated from magnetisation curves. At room temperature, the anisotropy constants of $SrFe_{12}O_{19}$ were high and positive, which agrees with the ref [8], suggesting a very high anisotropy along the c-axis. As Co-Ti substitution is introduced, the values of K_1 and K_2 are reduced, implying that the uniaxial anisotropy becomes planar anisotropy. This could be due to the tendency of Ti^{4+} (non-magnetic) ions to occupy (12k) octahedral sites which interrupts the magnetic interactions in such a way that the two blocks R S and R*S* become magnetically decoupled, as well as the tendency of Co^{2+} ions to occupy ($4f_1$) tetrahedral sites, and trigonal bi-pyramidal sites for ($x \geq 0.8$).

Temperature dependence of anisotropy constant of $SrCo_2Ti_2Fe_8O_{19}$ single crystal reveal that at 6 K, the magnetisation direction may form an easy cone with half angle θ of ($44 \pm 7°$), and the system could maintain this structure up to 250 K. Temperature dependence of magnetisation measurements for $SrCo_2Ti_2Fe_8O_{19}$ single crystal confirmed the presence of T_p which is likely to correspond to the transition temperature from the collinear ferrimagnetic phase to a conical structure [14][15]. The ZFC magnetisation curves are more complicated and sensitive to the applied field along H_{c-axis}. Additional turning points were observed as the measuring field increased. Clearly the phase between 50 K and 250 K is dependent on the applied field, as the applied field gets stronger the maximum change in magnetisation occurs at a lower temperature and the peak becomes broader. More measurements are required to investigate how this transition phase develops. To conclude, the results revealed clear evidence of a non-collinear magnetic structure at low temperature, which plays a key role for magnetoelectric properties.

Chapter 6

$SrCo_2Ti_2Fe_8O_{19}$ Thin Films

In this project, two M-type hexferrite $SrCo_2Ti_2Fe_8O_{19}$ thin films were grown using the Pulse Laser Deposition (PLD) system, at the University of York. The thin films were grown with different thicknesses in order to understand the effect of substrate-induced lattice strains on magnetic properties. The structure of the films were characterised using XRD, AFM and the magnetic properties using VSM, XMCD.

6.1 Growth of $SrCo_2Ti_2Fe_8O_{19}$ thin films by (PLD)

The thin films were grown on (0001) sapphire substrates with a dimension of 5x5x1 mm, using a wavelength of 266 nm, power of (1±0.09) W, repetition frequency of 10 Hz and pulses of 2 ns duration. The growth partial pressure of oxygen was $(2.0 \pm 0.5) \times 10^{-1}$ mbar and the substrates were heated to $(650 \pm 50)^{\circ}C$, for 20 min before the growth and maintained at temperature until 20 min after the growth under the same oxygen base pressure. These films were grown under the same growth conditions with the only difference being the deposition time of 10 and 45 min respectively. For clarity, the samples will be given name M_{10} and M_{45} as the thin films were deposited for 10 and 45 min, respectively. The average film thickness were estimated using cross-sectional transmission electron microscopy (TEM) of (15 ± 2) nm and (44 ± 3) nm, for M_{10} and M_{45}, respectively.

6.2 Structural characterisation

$(2\theta - \omega)$ scans were performed from 15° to 90°, with a 2 mm length limitation slit and 1 mm receiving slits. The step size was 0.01° and scan speed $0.3^{\circ}/min$. Before running the measurements, the samples alignment were optimised with respect to substrate peak by running a rock curve measurement on (0 0 6) reflection, 2θ of 41.684°. If the peak of ω scan occurred at 20.842° which corresponds to $\omega = \theta$, then the sample was well aligned. In the case of an offset, ω angle had to be corrected, and checked by running $(2\theta - \omega)$ scan to improve the alignment. In addition, any sample tilts, due to miscuts, were corrected by adjusting R_x and R_y axes on the sample stage so that the peak in $(2\theta - \omega)$ occurred at the centre 2θ for the bulk Al_2O_3. The diffraction pattern of the films are given in figure (6.1). All XRD patterns show M-type phase (0 0 2n) reflections, where n=1,2,3, ... , suggesting that these films are epitaxial in nature. A small amount of secondary phase was detected

(peaks labeled with the green asterisks), which can be assigned to cobalt ferrite. A rocking curve measurement was performed on the (0 0 8) reflection, see inset figure (6.1). A FWHM was determined using Voigt function of $(0.21 \pm 0.01)^\circ$ and

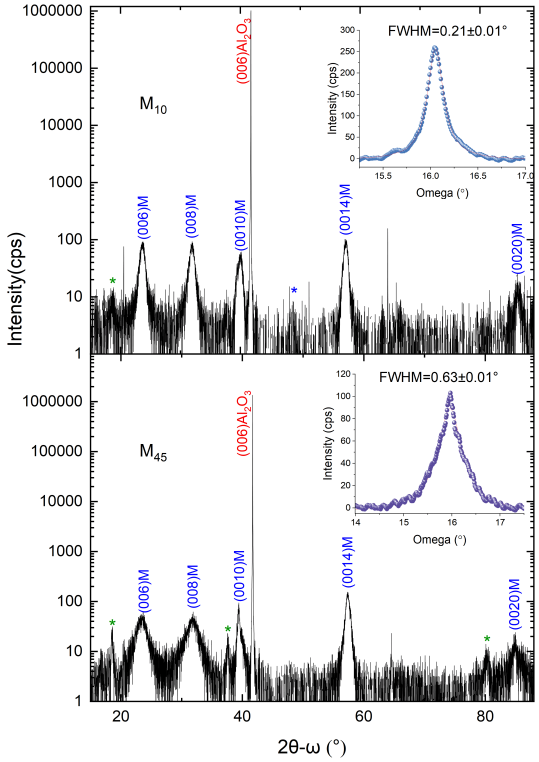

Figure 6.1: $(2\theta - \omega)$ scans for $SrCo_2Ti_2Fe_8O_{19}$ thin films deposited at 10 and 45 min with Miller indices labeled for observed hexaferrite and sapphire substrate diffraction peaks. The blue and green asterisks shows very weak reflections of the hexaferrite phase and impurity, respectively. ω- scan of (0 0 8) reflection shown as inset.

$(0.63 \pm 0.01)^\circ$ for M_{10} and M_{45}, respectively. The Lorentzian and Gaussian widths for M_{10} were $(0.21 \pm 0.005)^\circ$ and $(0.11 \pm 0.01)^\circ$, and for M_{45} these were $(0.621 \pm 0.003)^\circ$ and $(0.14 \pm 0.03)^\circ$. Since the instrumental broadening is small compared with the Lorentzian broadening, the value of FWHM is mainly intrinsic broadening in the material. These results are slightly smaller than those reported for 70 nm thickness of $SrCo_2Ti_2Fe_8O_{19}$ thin film, where FWHM was $(1.2 \pm 0.1)^\circ$ [31]. Study of epitaxial $BaFe_{12}O_{19}$ thin films grown by PLD showed that the FWHM increased as a function of film thickness ranging from 0.25° to 1.5° which agrees with our results [142]. This is likely to happen due to a loss of the c-axis orientation and film adhesion as the thickness increases [143].

Reciprocal space maps (RSM) were performed on reflections (1 1 3) and (2 0 5) for Al_2O_3 substrate and $SrCo_2Ti_2Fe_8O_{19}$ thin films, respectively, see figure (6.2). As shown, the thin film peak is broad which could be due to a finite crytallite size or due to the tilt of crytallites (mosaicity), and finite layer thickness [67]. Lattice parameters a and c were calculated using equation (3.18). For M_{10}, the a-lattice parameter was (5.83 ± 0.01) Å and the c-lattice parameter was (22.88 ± 0.01) Å. For M_{45}, the a-lattice constant was (5.81 ± 0.01) Å and the c-lattice constant was (22.92 ± 0.01) Å. These results are close to those for the 50 nm thickness grown by PLD [31] and are smaller than those reported earlier in chapters two and three

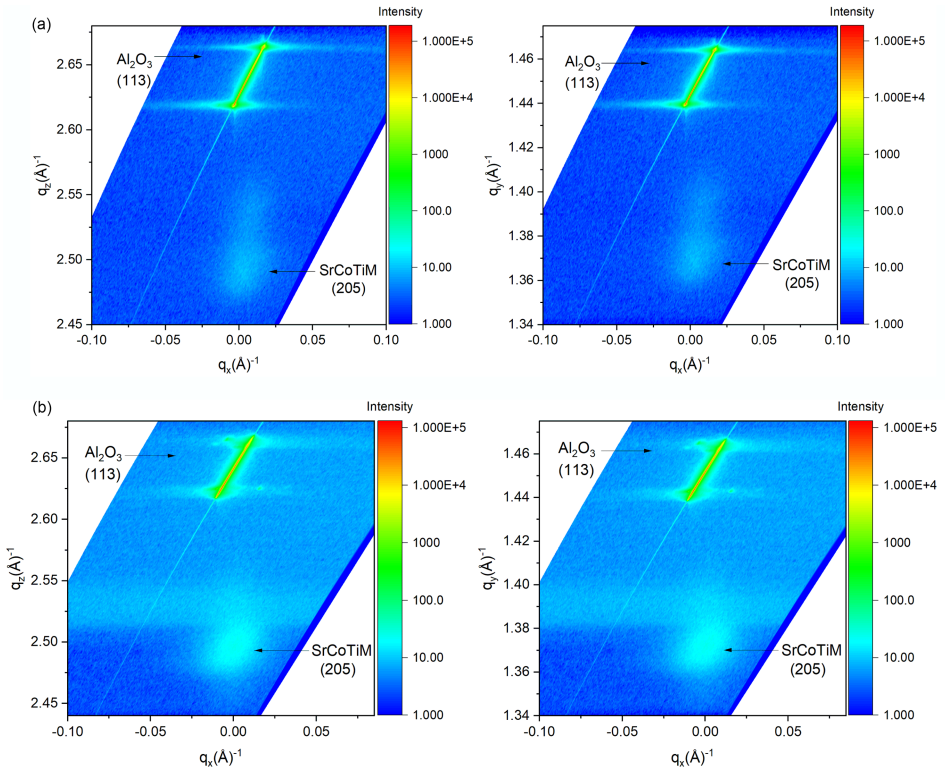

Figure 6.2: Reciprocal space maps of $SrCo_2Ti_2Fe_8O_{19}$ around (2 0 5) and (1 1 3) reflections of the thin film and substrate, respectively. (a) M_{10} thin film. (b) M_{45} thin film.

for the bulk single crystal (c=23.09 Å) and polycrystalline sample (c=23.11 Å and a=5.882 Å), implying that these films are under compressive strain with -0.91% and -0.74% for M_{10} and M_{45}, respectively. The c-lattice parameter increases with the thickness of the film, suggesting that these films are stressed due to a large lattice mismatch with the substrate and undergo relaxation with thickness. The lattice mismatch between the thin film and the substrate can be calculated as follow: mismatch $= (a_{sub} - a_{film})/a_{sub}$, where a_{sub} and a_{film} are the a lattice parameters of the substrate and film, respectively [80]. The lattice mismatch between thin films and substrate was 22.53% and 22.1% for M_{10} and M_{45}, respectively, which is close to the one grown by PLD which was around 23% [34].

Pole figure measurements were performed on (0 0 8) reflection, $2\theta \approx 31.2°$ to analyse the crystallographic texture of M_{10} and M_{45} thin films, see figure (6.3- a and d). The figure shows a spot at the centre corresponding to the (0 0 8) reflection itself indicating that the c-axis alignment is normal to the film. The six-fold symmetry spots correspond to closely spaced (1 0 7) reflections suggesting that the films possess a high degree of in-plane orientation.

Phi scans were performed to establish the epitaxial relationship between the thin film and the substrate. The measurements were on asymmetrical (1 0 7) and (1 0 4) reflections of the thin film and the substrate, respectively, see figure (6.3- b and e). The scans show six-fold and three-fold symmetry that corresponds to the thin film and the substrate, respectively. The peak positions show a 30° rotation of the $SrCo_2Ti_2Fe_8O_{19}$ unit cell with respect to the substrate, which is in agreement with

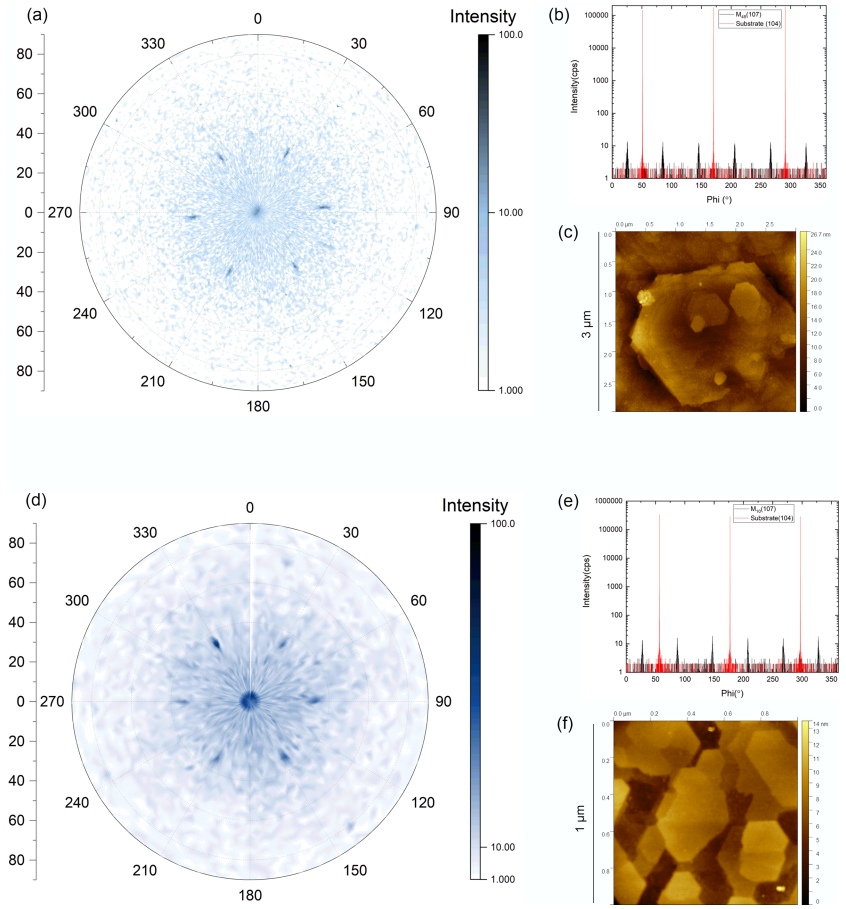

Figure 6.3: Pole figure measurement on (0 0 8) reflection for (a) M_{45} film and (d) M_{10} film. Phi scan at (1 0 7) and (1 0 4) reflections of the thin film and substrate, respectively, for (b) M_{45} film and (e) M_{10} film. AFM image for (c) M_{45} film and (f) M_{10} film.

ref [144]. This can be explained as the thin films starting its growth on the close-packed sub-lattice of O^{-2} ions in sapphire which are 30° rotation with respect to the main sapphire unit cell [144] see figure (6.4).

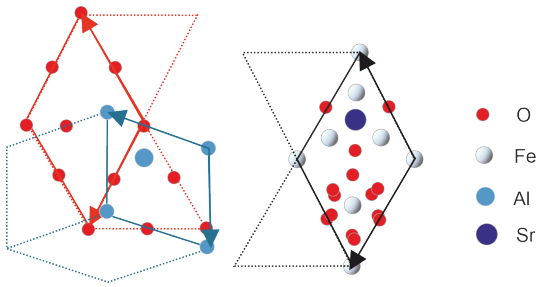

Figure 6.4: Perspective view of an Al_2O_3 single layer along with M-type hexaferrite structure. The oxygen sublattice in Al_2O_3 (red line), in plane Al_2O_3 lattice (blue line) and M-type hexaferrite (black line).

The topography of the thin films were characterised by Atomic Force Microscopy (AFM), see figure (6.3-c and f). The AFM images show hexagonal features that have a max roughness of (2.0 ± 0.5) nm and (4 ± 1) nm for M_{10} and M_{45}, respectively. The root mean square roughness, R_q, was (0.2 ± 0.05) nm and (0.73 ± 0.5) nm

for M_{10} and M_{45}, respectively, explaining the absences of Kiessig fringes in X-ray Reflectivity (XRR) measurement. Since, the reflected X-rays decay rapidly with a large surface roughness [145].

6.3 Magnetic characterisation

6.3.1 VSM analysis

The magnetic properties of these films were investigated by VSM. In-plane M-H measurements were performed at various temperatures ranging 10 K - 350 K, with the application of a magnetic field up to 50 kOe. The measurements were corrected for diamagnetic background contribution due to the sample holder and substrate by subtracting the slope obtained by linear fitting of the raw data at high field, assuming the magnetisation is fully saturated at this field. The hysteresis loop at various temperatures for M_{10} and M_{45} thin films are given in figures (6.5) and (6.6), respectively.

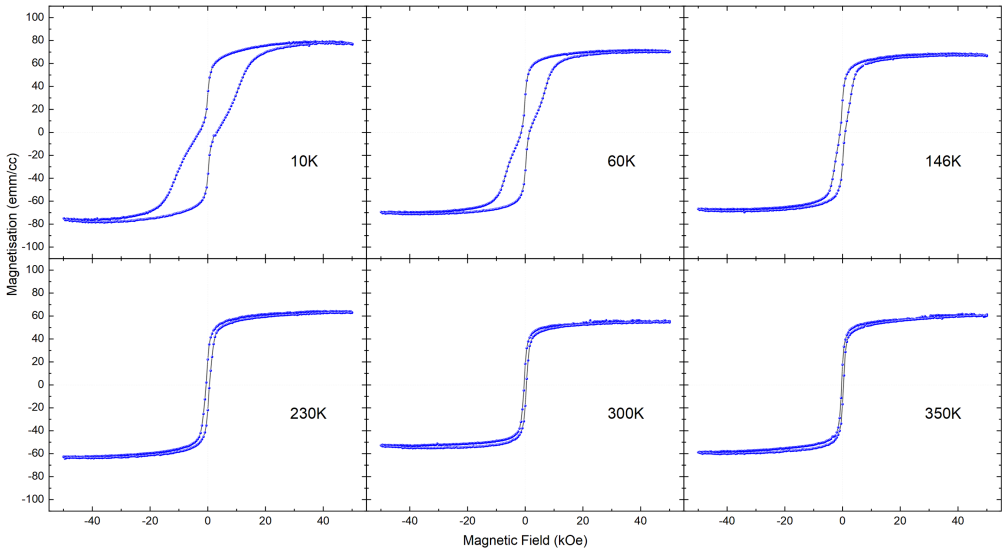

Figure 6.5: In plane M-H loop for the M_{10} thin film at various temperatures.

The M_{10} thin film shows wasp-waisted hysteresis loop at low temperature below 230 K, while this disappears as the temperature is increased above this level. Both saturation magnetisation and coercivity were reduced as the temperature increased. The saturation magnetisation at room temperature was (59 ± 3) emu/cc, which is slightly lower than the one reported, (80 ± 10) emu/cc [31]. The coercivity at room temperature was (392 ± 11) Oe, which is lower than the one reported, (760 ± 20) Oe [31]. The M_{45} thin film also shows wasp-waisted hysteresis loop at low temperature below 200 K, then disappears as the temperature is increased.

This behaviour is less pronounced when compared with the sample M_{10}. The saturation magnetisation at room temperature and coercivity were (110 ± 5) emu/cc, and (320 ± 80) Oe, respectively. These results are close to the 50 nm thin film grown by Beevers (2018) with a saturation magnetisation of (150 ± 20) emu/cc and coercivity of (520 ± 20) Oe at room temperature [31]. The low temperature M-H measurements for the 50 nm thin film observed wasp-waisted behaviour up to room

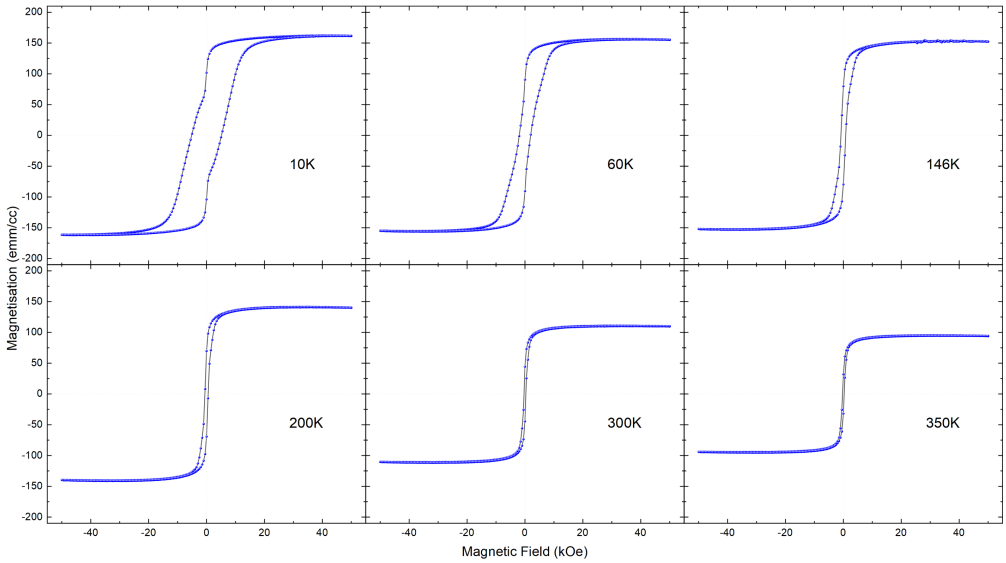

Figure 6.6: In plane M-H loop for the M_{45} thin film at various temperatures.

temperature. This behaviour may be attributed to a tendency of (Co-Ti) ions to occupy different sites within the lattice for different grains causing different coercivities within the sample.

Moreover, Beevers grew a 900 nm polycrystalline thin film under the same growth conditions with a saturation magnetisation of (170 ± 20) emu/cc and coercivity of (20 ± 5) Oe at room temperature. The coercivity is considerably smaller when compared with M_{10}, M_{45} and 50 nm thin films. However, this coercivity value was reported in 700 nm thin film grown by PLD [12]. Interestingly, the 900 nm thin film exhibits a typical hysteresis loop at low and room temperatures i.e. no wasp-waisted behaviour [31], suggesting that the magnetic properties of $SrCo_2Ti_2Fe_8O_{19}$ thin film changes significantly as a function of the thickness, such as a loss of the c-axis orientation and the development of non-oriented polycrystallines [143].

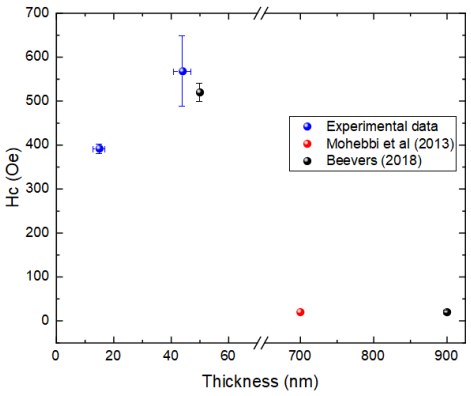

Figure 6.7: Coercivity for $SrCo_2Ti_2Fe_8O_{19}$ thin films grown by PLD at room temperature. The blue balls are the value of M_{10} and M_{45} thin films. The red and black balls are value from [12] and [31], respectively.

The coercivity value as a function of thickness for $SrCo_2Ti_2Fe_8O_{19}$ thin films grown by PLD, are given in figure (6.7). As can be seen, the coercivity is increasing for <40 nm thin films then starts to decrease as the thickness of the thin films

increases. Unfortunately, there is insufficient data to establish a trend of coercivity. In order to establish whether there is a gradual decrease or if there is a threshold thickness value more work needs to be carried out to establish how the coercivity changes with thickness.

The saturation magnetisation and coercivity of M_{10} and M_{45} thin films were plotted as a function of temperature, see figure (6.8). It can be seen that the temperature dependence of the magnetisation does not follow Bloch's $T^{3/2}$ law and the magnetisation of M_{45} thin film is nearly twice the magnetisation of M_{10}, which could be due to the presence of a magnetic dead layer on the thin film. Unfortunately, the lack of samples made it impossible to confirm the presence of a dead layer as the results fall within a 5 nm error.

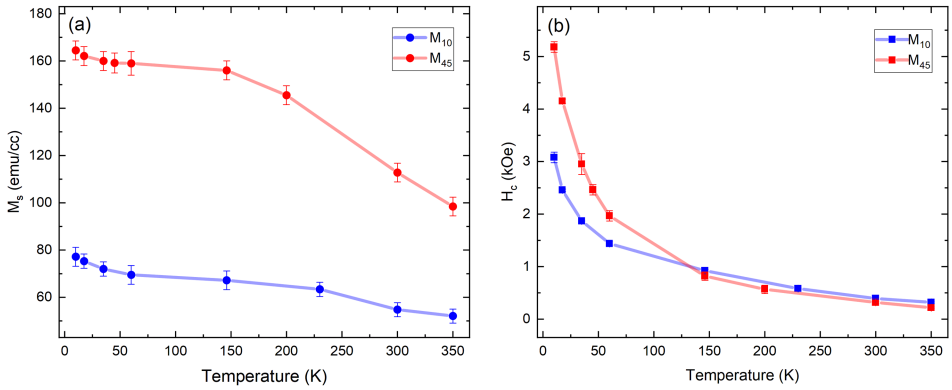

Figure 6.8: Magnetic properties for M_{10} and M_{45} thin films. (a) The saturation magnetisation, (b) The coercivity.

The saturation magnetisation for both films decreased with an increase in temperature, which is expected due to the thermal agitation. The temperature dependent M-H measurements show the coercivity for both films decreases gradually as the temperature increases. At low temperature, up to 100 K the difference in value of coercivity between the thin films is quite noticeable. At higher temperatures, the coercivity becomes less temperature sensitive which is similar to the observed trend for polycrystalline samples. If the magnetic properties are affected by the occupancy of (Co-Ti) ions into different sites, XMCD measurements may help provide more information about the valency, coordination and site occupancies of Co, Ti and Fe ions.

6.3.2 XMCD analysis

XAS experiments were performed on M_{10} and M_{45} thin films using the I06-beamline at Diamond Light Source. The XAS spectra at the Fe, Co and Ti $L_{2,3}$ absorption edges were obtained in the total electron yield mode (TEY) under UHV conditions. The measurements were carried out at room temperature with a 2 T applied magnetic field along the direction of the X-ray beam. All thin films were capped with (2.0 ± 0.5) nm of Al, to allow measurement of the drain current. The XMCD data was obtained by changing between two opposite directions of applied field at each photon energy. Each spectrum was normalised to unity just below the L_3 threshold. Figure (6.9) shows the right circular polarised, (μ^+) and left circular polarised, (μ^-) XAS and corresponding XMCD at the Fe $L_{2,3}$ edges for

M_{45} thin film. In M-type hexaferrite, there are three different environments where transitional metals can reside; octahedrally coordinated for 2a, 12k (with spin up) and $4f_2$ (with spin down) sites. Tetrahedrally coordinated for $4f_1$ site (with spin down) and trigonally bi-pyramidal coordinated for 2b site (with spin up). The XAS spectra for M_{45} thin film shows a typical iron oxide in which spectra are roughly divided into two regions; the L_3 edge around (708-714) eV and L_2 edges around (715-727) eV. Both these edges are split into two peaks. The XMCD spectra shows three distinct peaks at L_3 edge. The first negative peak corresponds to octahedrally coordinated Fe^{2+}, the second positive peak corresponds to tetrahedrally coordinated Fe^{3+} and the third negative peak corresponds to octahedrally coordinated Fe^{3+} [91]. These three peaks are also seen for XMCD of hexaferrites and Fe_3O_4 [146][147][32]. The Fe XMCD spectrum was fitted using multiplet calculations [96], red line in figure (6.9).

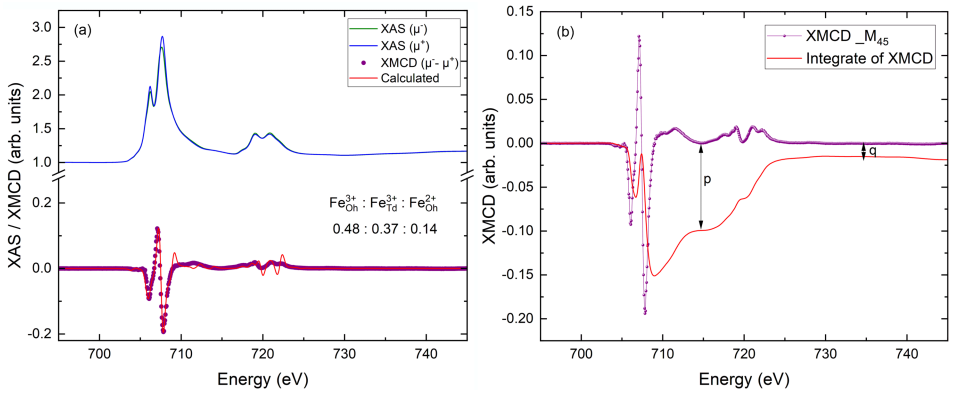

Figure 6.9: (a) The Fe XAS, XMCD and simulated spectrum at the $L_{2,3}$ edges for M_{45} thin film. (b) XMCD and integrated XMCD spectrum for the M_{45} thin film.

The simulated spectra were generated with the following parameters; $10D_q$ of 1.2 eV and -0.7 eV for octahedral and tetrahedral sites, respectively, following ref [31][147]. The Slater parameters reduced to 72% of Hartree-Fock values. The Lorentzian broadening values were 0.3-0.5 eV at the L_3 and L_2 respectively and the Gaussian broadening was 0.2 eV, see figure (6.10-a). By fitting experimental data and calculated spectra, the relative proportions of $Fe^{3+}_{O_h}$:$Fe^{3+}_{T_d}$: $Fe^{2+}_{O_h}$ were 0.49: 0.37 : 0.14 with an uncertainty of 10%. It should highlighted that these proportions represent the total magnetic contribution and does not mean the relative occupancy of the sites, since some contributions of spins cancel each other out due to opposite spin alignment [31].

The results show that most spin contributions come from Fe^{3+} octahedral and then tetrahedral, with around 49% and 37%, respectively. In addition, there was a non negligible amount of Fe^{2+} around 14%. The formation of Fe^{2+} is most likely due to oxygen deficiency during growth [8]. The presence of Fe^{2+} in the sample may affect the magnetic and electric properties, such as lowering the electrical resistivity and suppressing electric polarisation and ME effect [8][31]. The XMCD lineshape for M_{45} thin film is similar to the 50 nm thin film [31] with slightly higher tetrahedral ratio and lower Fe^{2+} content. The reduction of Fe^{2+} could be due to performing the growth with a higher oxygen pressure. According to the XMCD sum rules see equations (3.52 and 3.54), the ratio between the integral at the L_3 and L_2 edges (p

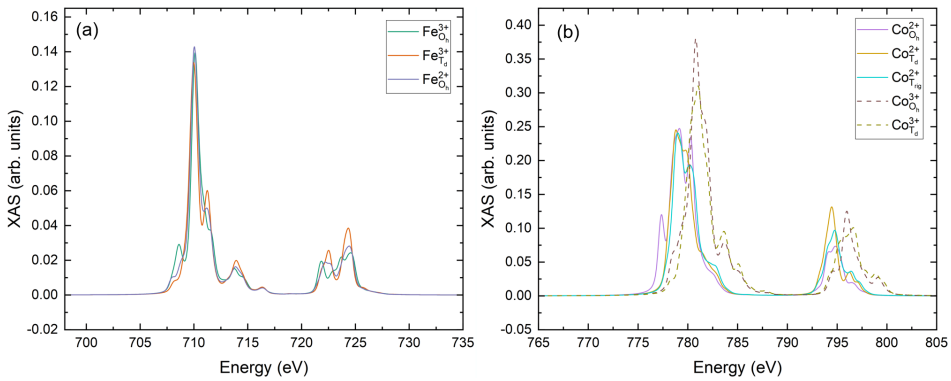

Figure 6.10: Calculated XAS spectra at the $L_{2,3}$ edges for (a) Fe^{3+} in octrahadral and tetrahedral coordinations, and Fe^{2+} in octrahadral coordination. (b) Co^{2+} in octrahadral, tetrahedral and trigonal bi-pyramidal coordinations, and Co^{3+} in octrahadral and tetrahedral coordinations.

and q) in figure (6.9), provide information of the orbital and spin ratio. As can be seen, both p and q are non zero and the value of q is smaller than p, implying a partially quenched orbital moment [31]. The μ_{orb} to μ_{spin} ratio was 0.0401, which is larger than the one reported for the 50 nm thin film at 0.016 [31].

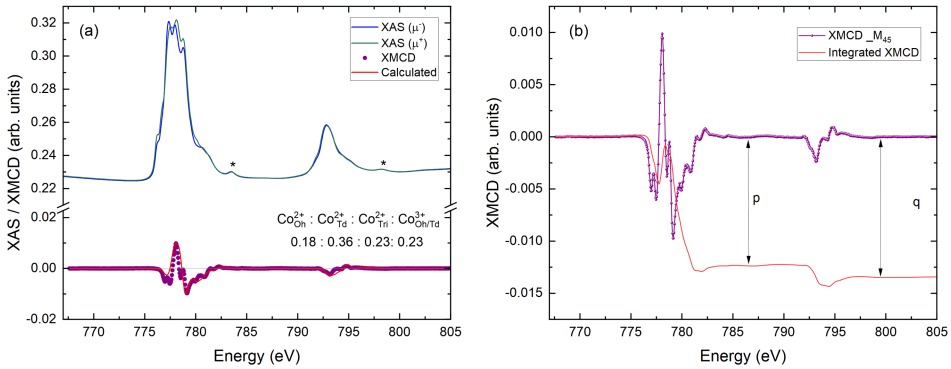

Figure 6.11: (a) The Co XAS, XMCD and simulated spectra at the $L_{2,3}$ edges for the M_{45} thin film. (b) The Co XMCD and integrated XMCD spectrum for the M_{45} thin film.

The Co XAS and XMCD spectra at the $L_{2,3}$ edges are shown in figure (6.11). The XAS spectra display two peaks around 778 eV and 793 eV these correspond to the Co L_3 and L_2 edges, respectively. In addition, two broad weak peaks appear around 783.5 eV and 798.1 eV (marked with an asterisk) these could be attributed to Co^{3+}, (if during the fitting process we include the Co^{3+} in both the octrahadral and tetrahedral sites, the fit is improved [148]), alternatively this could be attributed to the Ba M_5 and M_4 edges, since Ba was not one of the chemical stoichiometry, the presence of Ba could be due to contamination of the sample holder during the measurement or on the sample surface, as the peaks observed in ref [149][31][89]. However, EDS measurement is needed to confirm the absence of Ba within the sample. The Co XMCD spectrum was fitted using multiplet calculations [96], red line in figure (6.11). The simulated spectra for both Co^{2+} and Co^{3+} were generated with the following parameters; $10D_q$ of 1.2 eV and -0.7 eV for octahedral and tetrahedral sites, respectively. For the trigonal bi-pyramidal site, the C3i symmetry was used $10D_q$ of 0.8 eV, D_τ of -0.08 eV and D_σ of 0.01 eV, following ref [31]. The Slater parameters reduced to 72% of the Hartree-Fock values. The Lorentzian broadening

values were 0.3-0.5 eV at the L_3 and L_3 respectively and the Gaussian broadening was 0.2 eV, see figure (6.10-b). By fitting experimental data and calculated spectra, the relative proportions of $Co^{2+}_{O_h}$:$Co^{2+}_{T_d}$:$Co^{2+}_{T_{rig}}$:$Co^{3+}_{O_h/T_d}$ were 0.18: 0.36 : 0.23 : 0.23 with an uncertainty of 8%. The results indicate that the M_{45} thin film contained Co^{2+} ions around 18% on the octahedral site, a significant proportion up to 36% on the tetrahedral site, 23% on the trigonal bi-pyramidal site and at least 23% of Co^{3+} in the octahedral and the tetrahedral sites, suggesting that Co^{2+} has a slight preference to occupy the tetrahedral site. This could be due to the fact that the radius of Co^{2+}, 0.58 Å is larger than Fe^{3+}, 0.49 Å which has the effect of stabilising the spinel block structure [132][31]. This result is in agreement with the previous works based on neutron diffraction which established that Co^{2+} ions enter all five Fe^{3+} sites and have a strong preference to occupy the tetrahedral, trigonal bi-pyramidal (2b) and octahedral sites, successively [132][115]. The integrated Co XMCD spectrum is shown in figure (6.11). As can be seen, the value of q is slightly higher than p. The μ_{orb} to μ_{spin} ratio was 0.738 , which is higher than reported for the 50 nm thin film, this can be explained by the difference in the relative occupation of different Co^{2+} sites, since each of the sites has a different orbital moment quenching [31].

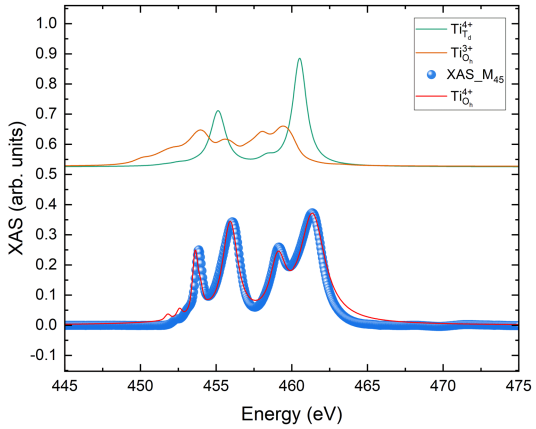

Figure 6.12: The Ti XAS and simulated spectra at the $L_{2,3}$ edges for the M_{45} thin film.

Figure (6.12) shows the Ti XAS at $L_{2,3}$ edges for the M_{45} thin film along with three simulated spectra of Ti^{4+}, Ti^{3+} in octahedral and Ti^{4+} in tetrahedral coordination. The simulated spectra were calculated with $10D_q$ of 1.9 eV and -0.9 eV for octahedral and tetrahedral symmetries, respectively. The Slater parameters also reduced to 72% of the HF values. The Lorentzian broadening values for each of the four peaks were 0.1 eV, 0.6 eV, 0.5 eV and 1.0 eV, respectively in order to best match the experimental data [150][31]. The Gaussian broadening was 0.2 eV. The XAS spectrum for M_{45} displays four distinct peaks that fit nicely with octahedral symmetry. The presence of the peaks can be explained as the spin orbit coupling splits the spectrum into two peaks $2p_{3/2}$ (L_3) and $2p_{1/2}$ (L_2) edges. Both of the L_3 and L_2 edges are split into (two more peaks) t_{2g} and e_g configuration due to crystal field splitting energy [88]. This result agrees with the one reported for the 50 nm thin film [31] and is consistent with neutron diffraction work on polycrystalline (Co-Ti) substituted barium hexaferrite, which suggests Ti^{4+} ions have a preference to occupy octahedral sites, 12k and $4f_2$ [86][115][151].

Figure (6.13) shows XAS and corresponding XMCD at the Fe $L_{2,3}$ edges for M_{10} thin film. The XAS for M_{10} thin film exhibits the same peaks that were observed for

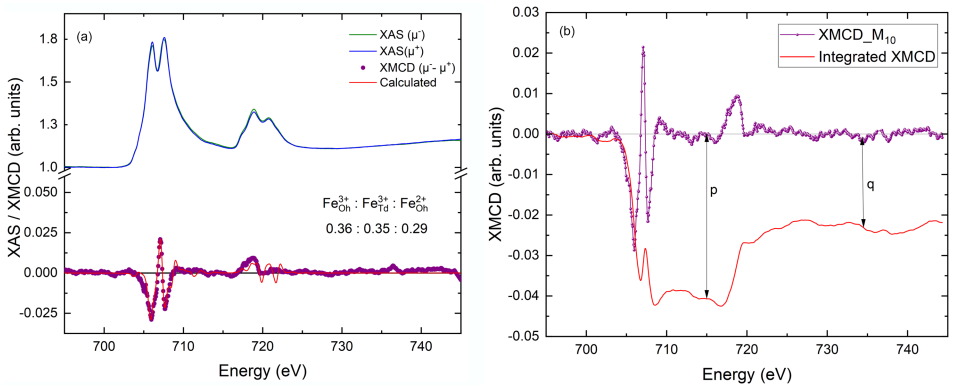

Figure 6.13: (a) The Fe XAS, XMCD and simulated spectra at the $L_{2,3}$ edges for M_{10} thin film. (b) The XMCD and integrated XMCD spectrum for M_{10} thin film.

the thicker film, M_{45}, but with a difference in the relative peak intensities. The Fe XMCD lineshape for M_{10} thin film shows the three main peaks (negative, positive, negative) at the L_3 edge that are proportional to the site occupancy of the $Fe^{2+}_{O_h}$, $Fe^{3+}_{T_d}$ and $Fe^{3+}_{O_h}$ cations, respectively. Comparing the Fe XMCD spectra of M_{10} to M_{45} thin films, it is obvious that there is a difference in the relative occupation of different Fe sites. The relative proportions of $Fe^{3+}_{O_h}$:$Fe^{3+}_{T_d/}$: $Fe^{2+}_{O_h}$ for M_{10} thin film were 0.36: 0.35 : 0.29, respectively, with uncertainty of 10%. The integrated XMCD spectra for M_{10} thin film is shown in figure (6.13). The μ_{orb} to μ_{spin} ratio was 0.0524, which is larger than that of the M_{45} thin film. As can be seen, the magnetic contribution from $Fe^{3+}_{O_h}$ and $Fe^{3+}_{T_d/}$ sites are similar, implying that the site occupancy of Fe cations are different from that of the thicker film, suggesting that film thickness plays a role in determining the magnetic properties. Unfortunately, this work presents only two samples, which is insufficient to establish a trend. More work needs to be carried out to investigate the variation of magnetic properties as a function of film thickness.

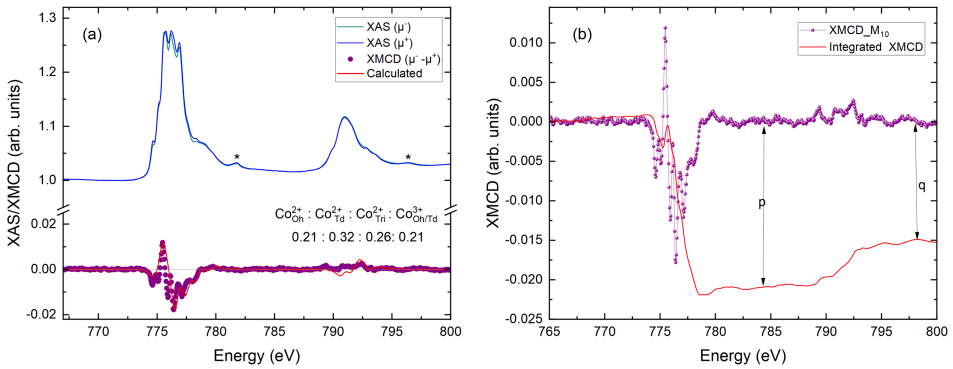

Figure 6.14: (a) The Co XAS, XMCD and simulated spectra at the $L_{2,3}$ edges for M_{10} thin film. (b) The Co XMCD and integrated XMCD spectrum for the M_{10} thin film.

Figure (6.14) shows XAS and corresponding XMCD at the Co $L_{2,3}$ edges for M_{10} thin film. The XAS displays the same peaks that are observed in the thicker film, M_{45}, but with a slight difference in the relative peak intensities, at L_3 edge. Two additional broad weak peaks are also observed (marked with an asterisk), that may be attributed to Co^{3+} or may be due to contamination of the sample holder during the measurement. The Co XMCD lineshape for M_{10} thin film was fitted using

multiplet calculations with the same parameters mentioned above [96]. The relative proportions of $Co^{2+}_{O_h}$:$Co^{2+}_{T_d}$:$Co^{2+}_{T_{rig}}$:$Co^{3+}_{O_h/T_d}$ were 0.21 : 0.32 : 0.26 : 0.21, with an uncertainty of 8%. Comparing the Co XMCD spectra of M_{10} to M_{45} thin films, it is obvious that there is little difference in the relative occupation of different Co sites. The result shows that the M_{10} thin film contained Co^{2+} ions around 21% on the octahedral site, a 32% on the tetrahedral site, a 26% on the trigonal bi-pyramidal site and at least 21% of Co^{3+} in the octahedral and the tetrahedral sites. These results agree with the observed hierarchy above in which the Co^{2+} tend to occupy the tetrahedral, trigonal bi-pyramidal (2b) and octahedral sites, successively. The integrated XMCD spectra for M_{10} thin film is shown in figure (6.14). The μ_{orb} to μ_{spin} ratio was 1.31, which is higher than that of the M_{45} thin film.

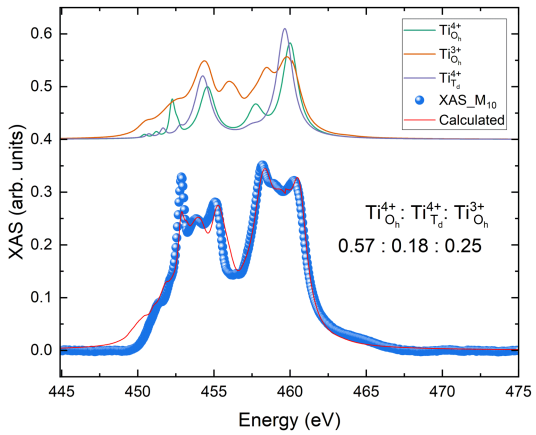

Figure 6.15: The Ti XAS for M_{10} thin film and simulated spectra at the $L_{2,3}$ edges.

The Ti XAS for M_{10} is shown in figure (6.15). As can be seen, the spectrum is different and more complicated than that observed for M_{45} thin film. The two main peaks (the L_3 and L_2 edges around 454 eV and 460 eV , respectively) split into several peaks, implying that the spectrum is not purely octahedrally coordinated, instead it is combination of $Ti^{4+}_{O_h}$, $Ti^{4+}_{T_d}$ and $Ti^{3+}_{O_h}$ symmetries. The fitting result shows that the Ti^{4+} ions were mostly octahedral coordinated with around 57.5%, tetrahedral coordinated with 17.5% and there was around 25% of Ti^{3+}, with an uncertainty of 6%. This is an interesting result which is consistent with the argument that Ti ions have a strong preference to occupy octahedral sites, 12k and $4f_2$ and is in agreement with the idea that Ti^{4+} ions occupy tetrahedral sites when x>0.6 [152].

6.4 Summary and Conclusions

In this chapter, two $SrCo_2Ti_2Fe_8O_{19}$ thin films were grown on sapphire substrates by PLD. The growth conditions only varied in the deposition time, 10 min and 45 min, respectively, which accounts for the difference in thickness. The crystal structure of the thin films were confirmed, using XRD, by the presence of (0 0 2n) reflections. The lattice parameters and quality of the thin films were assessed through various scans suggesting these films are epitaxial in nature. The results demonstrate that the c-lattice parameter and FWHM increase as thickness increases, suggesting that these films accommodate the stresses due to a large lattice mismatch with the substrate about 23%, and as the thickness increases the films undergo relaxation into polycrystalline growth [143][31]. Furthermore, the magnetisation measurements at

various temperatures show both samples exhibit wasp-waisted hysteresis loops at temperatures below 200 K, which is similar to the 50 nm thin film grown by PLD [31] this could be attributed to a tendency of (Co-Ti) ions to occupy different sites within the lattice for different grains causing different coercivities within the sample. In addition, M_s and H_c increase with an increase in the film thickness. However, the limited number of samples available, (15 ± 2) nm and (44 ± 3) nm, and comparison of 50 nm [9], means we cannot establish this as a trend and it has been reported that H_c decreases with thickness [34]. In order to establish whether there is a gradual decrease or if there is a threshold thickness value more work needs to be carried out to establish how the coercivity changes with thickness. XAS and XMCD were performed at the Fe, Co and Ti L-edges and fitted with atomic multiplet calculations to determine their valence, coordination and relative occupation of each site in the structure. The Fe XMCD analysis show that both samples have Fe^{3+} and a non negligible amount of Fe^{2+}, which may reduce the electrical resistivity and suppress electric polarisation and ME effect. The Fe XMCD spectrum for M_{45} is slightly different in the relative peak intensities from that of M_{10}. For M_{45}, most spin contributions come from the octahedral and then the tetrahedral sites, respectively. Whereas for M_{10} the spin contributions were similar across all sites, suggesting that the site occupancy of Fe cations are different in both samples. The Co XMCD spectrum for both samples reveals that Co has a 2+ valence, and enters all sites with a significant proportion on the tetrahedral site and then the trigonal bi-pyramidal site. In addition, both samples may contain around 22% of Co^{3+} ion in the octahedral and the tetrahedral sites. These results agree with the observed hierarchy above in which the Co^{2+} tend to occupy the tetrahedral, trigonal bi-pyramidal (2b) and octahedral sites, successively [132]. The Ti XAS for M_{45} is purely octahedrally coordinated, whereas the Ti XAS for M_{10} is more complicated, it is a combination of $Ti^{4+}_{O_h}$, $Ti^{4+}_{T_d}$ and $Ti^{3+}_{O_h}$ symmetries with a majority of Ti^{4+} occupying the octahedral sites. Clearly there is a large difference in the relative occupancy of Fe, Ti and Co into different sites, as the thickness increases. More work needs to be carried out to investigate the variation of magnetic properties as a function of film thickness.

Chapter 7

Conclusions and Future Work

7.1 Conclusions

The presented work was undertaken with two main objectives. The first objective was to synthesise single crystals and polycrystalline of $SrCo_xTi_xFe_{12-x}O_{19}$ M-type hexaferrite, with different Co-Ti substitution rates. The second objective was to study the magnetic properties and their temperature dependency in doped M-type hexaferrite. Doped M-type hexaferrite may have a non-collinear magnetic structure, such features are usually associated with electric polarisation of the material, inducing ME effect, via the inverse Dzyaloshinskii-Moriya model.

A series of $SrCo_xTi_xFe_{12-x}O_{19}$ polycrystalline samples with x= 0, 0.7, 1.1, 1.5 and 2, were prepared using the solid state method to investigate the role of Co-Ti substitution in both structure and magnetic properties as the rate of substitution alters. XRD analysis confirmed the presence of both M-type hexaferrite phase as the majority and hematite phase as the minority with a similar percentage in all the samples, less than 13%. The c-lattice constant increases slightly and the a-lattice constant decreases marginally as the Co-Ti substitution increases, which is in agreement with the literature [8][106]. The unit cell volume increased with an increase in the (Co-Ti) substitution, due to the average ionic radius of the (Co-Ti) ions being larger than Fe ion [106]. VSM analysis show that $SrFe_{12}O_{19}$ exhibits typical behaviour of ferrimagnetic M-type hexaferrite, and as the Co-Ti substitution was introduced, the saturation magnetisation and remanent magnetisation decreased gradually. The reduction in the magnetisation can be attributed to replacing Fe^{3+} ions with non magnetic Ti^{4+} ions and Co^{2+} ions, which have a smaller moment [106]. The coercive field decreases dramatically with Co-Ti substitution, which can be explained by the tendency of Co^{2+} ions to occupy the tetrahedral $4f_2$ and trigonal bipyramid (2b) sites, leading to a non collinear magnetic structure and the development of cone magnetisation [8]. The magnetocrystalline anisotropy constant, K_1 reduces with substitution, suggesting that the magnetocrystalline anisotropy gradually changes from uniaxial to planar anisotropy as a result of Ti^{4+} ions occupying the octahedral (12k) sites and Co^{2+} ions occupying the tetrahedral $4f_2$ sites and the trigonal bipyramid (2b) sites [85][106][8]. Temperature dependence of the magnetisation measurements reveal that when the Co-Ti substitution was introduced, a broad peak was developed in M_{ZFC} curve, this is likely to be associated to the transition from a collinear ferrimagnetic phase to a non collinear (conical) magnetic phase, T_{cone} [14][45][16].

Two single crystals of $SrFe_{12}O_{19}$ and $SrCo_2Ti_2Fe_8O_{19}$ were grown by FZ to investigate the anisotropy and magnetic properties on bulk M-type hexaferrite. The XRD analysis confirmed the presence of M-type hexaferrite crystal structure. The magnetisation curve analysis show that $SrFe_{12}O_{19}$ single crystal displays a typical behaviour of uniaxial crystal anisotropy, in which the hexagonal c-axis is the easy magnetisation axis and the ab-plane is the hard magnetisation axis. Whereas, $SrCo_2Ti_2Fe_8O_{19}$ single crystal shows a wasp-waisted hysteresis loop only for low temperature H_{ab} measurements up to 250 K, implying a complex non-collinear structure. The anisotropy constants K_1 and K_2 for the crystals were evaluated from magnetisation curves. The anisotropy constants of the $SrFe_{12}O_{19}$ were high and positive as expected, implying a very high anisotropy along the c-axis. For the $SrCo_2Ti_2Fe_8O_{19}$, the value of K_1 and K_2 reduced, implying that the uniaxial anisotropy becomes planar anisotropy. This could be due to the tendency of Ti^{4+} (non-magnetic) ions to occupy (12k) octahedral sites which interrupts the magnetic interactions in a such way that the two blocks R S and R*S* become magnetically decoupled, as well as the tendency of Co^{2+} ions to occupy ($4f_1$) tetrahedral sites, and trigonal bi-pyramidal sites for ($x \geq 0.8$). Temperature dependence of the anisotropy constant of the $SrCo_2Ti_2Fe_8O_{19}$ single crystal reveals that at 6 K, the magnetisation direction may form an easy cone with half angle θ of ($44 \pm 7°$), and the system could maintain this structure up to 250 K. M(T) measurements for $SrCo_2Ti_2Fe_8O_{19}$ single crystal confirmed the presence of T_p which is likely to correspond to the transition temperature were the collinear ferrimagnetic phase changes to a conical structure [14][15]. The ZFC magnetisation curves are more complicated and sensitive to the applied field along H_{c-axis}. The results show step like anomalies in the M-H loops which could be indicative of a metamagnetic transition of the spin cone to either a fanlike structure or collinear order as discussed in [14]. Such features are usually associated with electrical polarisation of the material.

Two thin films of $SrCo_2Ti_2Fe_8O_{19}$ M-type hexaferrite were grown on a sapphire substrate by PLD technique to investigate the strain effect on structural and magnetic properties. Their epitaxial crystal structures were confirmed using XRD. The results show that the unit cell increased with thickness suggesting that the samples undergo relaxation of stresses as the thickness increases. The magnetic properties M_s and H_c also improved with an increase in the thickness. XMCD analysis reveals that there is a significant difference in the site occupancy of the Fe and Ti ion between the samples. For the M_{45} sample, most of magnetic contribution of the Fe comes from octahedral and then tetrahedral sites with a small amount of Fe^{2+}. Whereas, for the M_{10} sample there is no clear occupancy site preference, with a higher amount of Fe^{2+}. The Ti XAS fitting shows that the M_{45} sample has Ti^{4+} and is purely octahedrally coordinated, as reported in previous work [31]. Meanwhile, the M_{10} sample has a combination of $Ti^{4+}_{O_h}$, $Ti^{4+}_{T_d}$ and $Ti^{3+}_{O_h}$ symmetries with a majority of Ti^{4+} occupying the octahedral sites. The Co XMCD spectrum for both samples reveals that Co has a 2+ valence and enters all sites following the observed hierarchy, in which the Co^{2+} tend to occupy the tetrahedral, trigonal bi-pyramidal (2b) and octahedral sites, successively [132]. In addition, both samples may contain around 22% of Co^{3+} ion in the octahedral and the tetrahedral sites. Hence, clearly there is a large difference in the relative occupation of Fe, Ti and Co into different sites, as the thickness increases. More work needs to be done to investigate the variation of magnetic properties as a function of film thickness.

7.2 Future work

This work presents some evidence that could support the existence of a non-collinear magnetic structure in $SrCo_2Ti_2Fe_8O_{19}$ M-type hexaferrite at low temperature, which is promising for ME coupling. However, thus far the dielectric properties for these samples have yet to be characterised. Further measurements are required to investigate the ferroelectric properties, electrical polarisation measurements are essential, ME coupling measurements for all samples would also be highly advantageous. Investigation into the mechanisms involved in magnetoelectric coupling in M-type hexaferrite is also required, since the origin of ferroelectricity and how it enhances the ME properties in M-type hexaferrite is still not fully understood.

7.2.1 $SrCo_xTi_xFe_{12-x}O_{19}$ polycrystalline samples

It would be highly beneficial to combine the high resolution XRD data with neutron diffraction measurements to enable study of the fractional occupancy of the different cation sites and to correlate the Co occupancy of the bi-pyramidal site to the electrical polarisation and ME measurements. Investigation into the evolution of magnetic structure as the substitution and temperature rates increase would help to improve our understanding of temperature dependence on magnetisation. Moreover, improvements in the synthesis recipe may help to form a single phase M-type hexaferrite.

7.2.2 $SrCo_2Ti_2Fe_8O_{19}$ single crystals

Investigation of the magnetic ground state of $SrCo_2Ti_2Fe_8O_{19}$ using X-ray absorption spectra (XAS), X-ray magnetic circular dichroism (XMCD), and neutron diffraction measurements could help to confirm the presence of the longitudinal conical magnetic structure and this could be used to explain the anomalies seen in (M-H) loops and the temperature dependence of magnetisation measurements. In addition, torque measurements would give an accurate value of the anisotropy constants, removing the need for the fitting and thus reducing the associated error. Investigation into the dynamics of magnetoelectric hexaferrites using a variety of techniques such as Ferromagnetic Resonance Magnetometer(FMR) and Time-resolved magneto-optical Kerr effect (TR-MOKE) may help to gain a critical understanding of their high frequency electromagnetic response.

7.2.3 $SrCo_2Ti_2Fe_8O_{19}$ thin films

To help further understand the role of film thickness in magnetic, ferroelectric and ME properties, it would greatly help to grow a series of varying thickness films between 15-700 nm in order to investigate at which film thickness polycrystalline growth is first evident.

Growth conditions could be further optimised to remove the presence of Fe^{2+}. It is generally understood that oxygen deficiency plays a major role in the formation of Fe^{2+}. The presence of Fe^{2+} has a detrimental effect on the magnetoelectric effect as it provides a conductive pathway leading to a suppressing of electric polarisation. Therefore, optimisation of the growth by the removal of oxygen deficiency would only have a beneficial effect.

Appendix A

Supporting materials: (Bragg equation)

$$d_{hkl} = \frac{2\pi}{q} \tag{A.1}$$

For a hexagonal system:

$$\frac{1}{d^2} = \frac{4(h^2 + hk + k^2)}{3a^2} + \frac{l^2}{c^2} \tag{A.2}$$

by taking the squared root :

$$\frac{1}{d} = \frac{2\sqrt{(h^2 + hk + k^2)}}{\sqrt{3}a} + \frac{l}{c} \tag{A.3}$$

rearranging the equation:

$$d = \frac{\sqrt{3}a}{2\sqrt{h^2 + hk + k^2}} + \frac{c}{l} \tag{A.4}$$

substituting the value of d using equation (A.1):

$$\frac{2\pi}{q} = \frac{\sqrt{3}a}{2\sqrt{h^2 + hk + k^2}} + \frac{c}{l} \tag{A.5}$$

where q_x and q_z are the scattering vector parallel and perpendicular to the sample surface, respectively. Therefore, a and c -lattice constants can be calculated from the equation (A.5).

$$a = \frac{2\sqrt{h^2 + hk + k^2}}{\sqrt{3}} \frac{2\pi}{q_x} = \frac{4\pi h}{\sqrt{3}q_x} \tag{A.6}$$

$$c = \frac{2\pi}{q_z} l \tag{A.7}$$

Appendix B

Supporting materials (XRD)

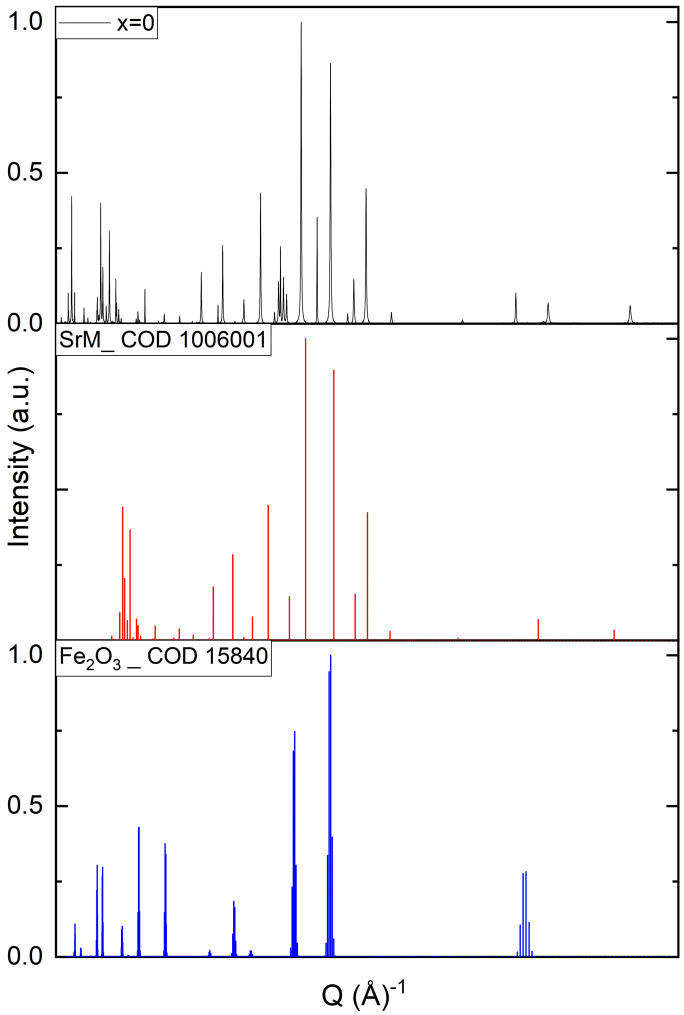

Figure B.1: XRD pattern for x=0 sample, and the standard patterns of $SrFe_{12}O_{19}$ (COD 1006001) and Hematite (COD 15840).

B.1 The calculated patterns (models) that were used in the refinement:

- The calculated pattern of Fe_2O_3, belongs to ($R\bar{3}c$) space group (164) and has lattice parameters: $a = b = 5.03800$ Å, $c = 13.772$ Å, and unit cell volume $= 302.722$ Å^3.

Table B.1: The structure parameters of Fe_2O_3 calculated pattern.

Structure parameters	x	y	z	Occ.	B	Site	Sym.
Fe1	0.00000	0.00000	0.35530	1	1	12c	3
O1	0.30590	0.00000	0.2500	1	0.468	18e	2

- The calculated pattern of $SrFe_{12}O_{19}$, (model-1) belongs to ($P6_3/mmc$) space group and has lattice parameters: $a = b = 5.883$ Å, $c = 23.037$ Å, and unit cell volume$= 690.643$Å^3.

Table B.2: The structure parameters of $SrFe_{12}O_{19}$ (model-1).

Structure parameters	x	y	z	Occ.	B	Site	Sym.
Sr1	0.66667	0.33333	0.25000	1	0.895	2d	-6m2
Fe1	0.00000	0.00000	0.00000	1	0.372	2a	-3m
Fe2	0.00000	0.00000	0.25490	0.50	0.521	4e	3m
Fe3	0.33333	0.66667	0.02718	1	0.345	4f	3m
Fe4	0.33333	0.66667	0.19091	1	0.388	4f	3m
Fe5	0.16886	0.33772	0.89083	1	0.399	12k	m
O1	0.00000	0.00000	0.15140	1	0.468	4e	3m
O2	0.66667	0.33333	0.05540	1	0.490	4f	3m
O3	0.18190	0.36380	0.25000	1	0.719	6h	mm2
O4	0.15640	0.31280	0.05252	1	0.416	12k	m
O5	0.50390	0.00780	0.15093	1	0.508	12k	m

- The calculated pattern of $BaCo_{0.85}Ti_{0.85}Fe_{10.3}O_{19}$, (model-2) belongs to the space group of ($P6_3/mmc$) and has lattice parameters: $a = b = 5.884$ Å, $c = 23.175$ Å, and unit cell volume= 694.999Å^3. Adjustment was applied, before the refinement procedure, to replace Ba cation ion with Sr ion. In addition, the occupancy sites of Co(1,2) and Ti(1,2) reduced to (0.0900), and Fe(3,4) increased to 0.91, Fe(5) to (0.8200) to match the chemical formal.

Table B.3: The structure parameters of $BaCo_{0.85}Ti_{0.85}Fe_{10.3}O_{19}$ (model-2).

Structure parameters	x	y	z	Occ.	B	Site	Sym.
Ba1	0.66667	0.33333	0.25000	1	0.730	2d	-6m2
Fe1	0.00000	0.00000	0.00000	1	0.660	2a	-3m
Fe2	0.00000	0.00000	0.25960	0.50	0.410	4e	3m
Fe3	0.33333	0.66667	0.02720	0.893	0.250	4f	3m
Co1	0.33333	0.66667	0.02720	0.107	0.250	4f	3m
Fe4	0.33333	0.66667	0.18950	0.83	0.600	4f	3m
Ti1	0.33333	0.66667	0.18950	0.107	0.600	4f	3m
Fe5	0.16820	0.33640	0.89270	0.786	0.480	12k	m
Co2	0.16820	0.33640	0.89270	0.107	0.480	12k	m
Ti2	0.16820	0.33640	0.89270	0.107	0.480	12k	m
O1	0.00000	0.00000	0.15140	1	0.47	4e	3m
O2	0.33333	0.6667	0.94340	1	0.540	4f	3m
O3	0.18360	0.36720	0.25000	1	0.440	6h	mm2
O4	0.15610	0.31220	0.05270	1	0.500	12k	m
O5	0.50020	0.00040	0.15020	1	0.470	12k	m

- The calculated pattern of $BaCo_1Ti_1Fe_{10}O_{19}$, (model-3), belongs to ($P6_3/mmc$) space group and has lattice parameters: $a = b = 5.888$ Å, $c = 23.190$ Å, and unit cell volume= 696.282 Å^3. Adjustment was applied, before the refinement procedure, to replace Ba cation ion with Sr ion. Further adjustment on the occupancy sites of cations were applied to match the chemical formal. For Co and Ti ions were increased to (0.0900) and (0.125) for x=1.1 and x=1.5, respectively. Therefore, Fe ion was reduced to (0.815) and (0.75) for x=1.1 and x=1.5, respectively.

Table B.4: The structure parameters of $BaCo_1Ti_1Fe_{10}O_{19}$ (model-3).

Structure parameters	x	y	z	Occ.	B	Site	Sym.
Ba1	0.33333	0.66667	0.25000	1	1	2c	-6m2
Co1	0.00000	0.00000	0.00000	0.083	1	2a	-3m
Ti1	0.00000	0.00000	0.00000	0.083	1	2a	-3m
Fe1	0.00000	0.00000	0.00000	0.833	1	2a	-3m
Co2	0.00000	0.00000	0.025000	0.083	1	2b	-6m2
Ti2	0.00000	0.00000	0.025000	0.083	1	2b	-6m2
Fe2	0.00000	0.00000	0.025000	0.833	1	2b	-6m2
Co3	0.33333	0.66667	-0.02800	0.083	1	4f	3m
Ti3	0.33333	0.66667	-0.02800	0.083	1	4f	3m
Fe3	0.33333	0.66667	-0.02800	0.833	1	4f	3m
Co4	0.33333	0.66667	-0.19000	0.083	1	4f	3m
Ti4	0.33333	0.66667	-0.19000	0.083	1	4f	3m
Fe4	0.33333	0.66667	-0.19000	0.833	1	4f	3m
Co5	0.17000	0.34000	0.10800	0.083	1	12k	m
Ti5	0.17000	0.34000	0.10800	0.083	1	12k	m
Fe5	0.17000	0.34000	0.10800	0.833	1	12k	m
O1	0.00000	0.00000	0.14200	1	1	4e	3m
O2	0.33333	0.6667	0.06100	1	1	4f	3m
O3	0.82100	0.64200	0.25000	1	1	6h	mm2
O4	0.83100	0.66200	0.05200	1	1	12k	m
O5	0.50400	0.00800	0.14800	1	1	12k	m

- The calculated pattern of $BaCo_2Ti_2Fe_8O_{19}$, (model-4), belongs to ($P6_3/mmc$) space group and has lattice parameters: $a = b = 5.889$ Å, $c = 23.254$ Å, and unit cell volume= 698.441Å^3. Adjustment was applied, before the refinement procedure, the cation type of Ba was replaced with Sr to match the formula.

Table B.5: The structure parameters of $BaCo_2Ti_2Fe_8O_{19}$ (model-4).

Structure parameters	x	y	z	Occ.	B	Site	Sym.
Ba1	0.33333	0.66667	0.25000	1	1	2c	-6m2
Co1	0.00000	0.00000	0.00000	0.167	1	2a	-3m
Ti1	0.00000	0.00000	0.00000	0.167	1	2a	-3m
Fe1	0.00000	0.00000	0.00000	0.667	1	2a	-3m
Co2	0.00000	0.00000	0.025000	0.167	1	2b	-6m2
Ti2	0.00000	0.00000	0.025000	0.167	1	2b	-6m2
Fe2	0.00000	0.00000	0.025000	0.667	1	2b	-6m2
Co3	0.33333	0.66667	-0.02800	0.167	1	4f	3m
Ti3	0.33333	0.66667	-0.02800	0.167	1	4f	3m
Fe3	0.33333	0.66667	-0.02800	0.667	1	4f	3m
Co4	0.33333	0.66667	-0.19000	0.167	1	4f	3m
Ti4	0.33333	0.66667	-0.19000	0.167	1	4f	3m
Fe4	0.33333	0.66667	-0.19000	0.667	1	4f	3m
Co5	0.17000	0.34000	0.10800	0.167	1	12k	m
Ti5	0.17000	0.34000	0.10800	0.167	1	12k	m
Fe5	0.17000	0.34000	0.10800	0.667	1	12k	m
O1	0.00000	0.00000	0.14200	1	1	4e	3m
O2	0.33333	0.6667	0.06100	1	1	4f	3m
O3	0.82100	0.64200	0.25000	1	1	6h	mm2
O4	0.83100	0.66200	0.05200	1	1	12k	m
O5	0.50400	0.00800	0.14800	1	1	12k	m

Appendix C

Supporting materials (SEM)

C.1 Sample mounting on SEM

The morphology and the chemical composition of the $SrCo_xTi_xFe_{12-x}O_{19}$ samples were determined using 7800F SEM at a beam energy of 20 keV and 8 nA probe current. All were mapped using the Oxford Instruments UltiMax-100EDS detector and mapped at a magnification of 1000× (field of view=120.7×90.6 μm^2). The polycrystalline samples were pressed onto sticky carbon tabs (with aluminium cores) mounted onto a 25 mm aluminium stub, see figure (C.1). Excess (loose) powders were removed with compressed air gun blowing from centre outwards after each powder was pressed, starting with x = 0, 0.7,... (marked with •, • •, ...) in a clockwise fashion.

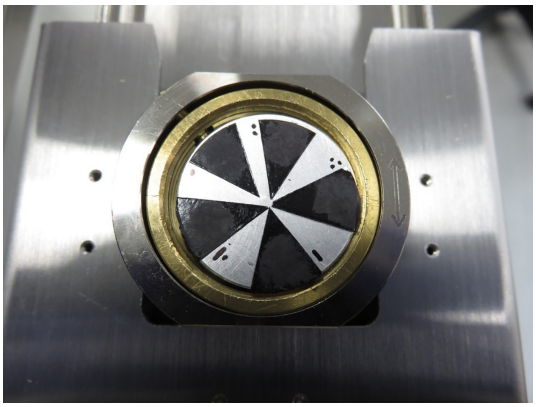

Figure C.1: The polycrystalline samples mounted onto a 25 mm aluminium stub.

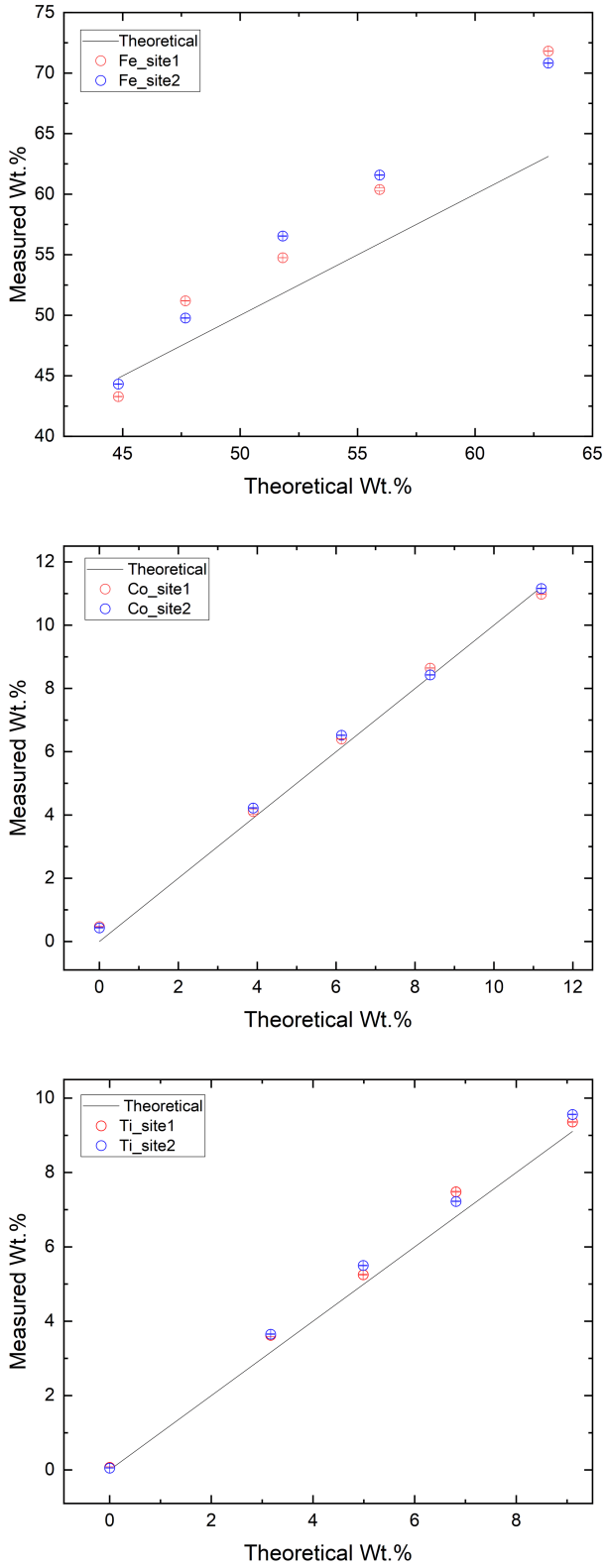

Figure C.2: The measured versus nominal (theoretical) weight percentages for the $SrCo_xTi_xFe_{12-x}O_{19}$ samples, for Fe (on the top), Co (on the middle) and Ti ion (on the bottom).

C.2 Elemental maps (site 1)

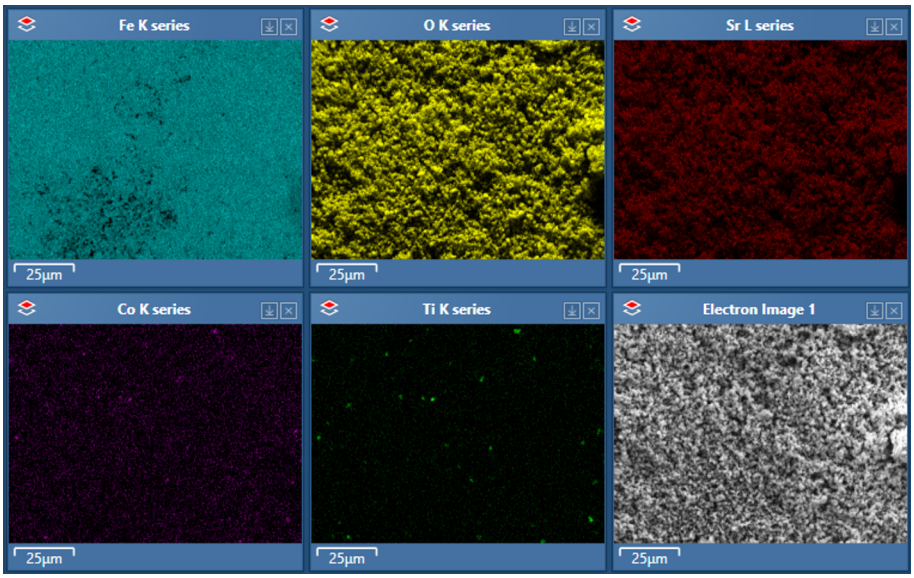

Figure C.3: Sample x = 0. Note the Ti map is spotty, suggesting contamination with high-Ti/Co powders. Shadowing effects are seen for O K and Sr L maps.

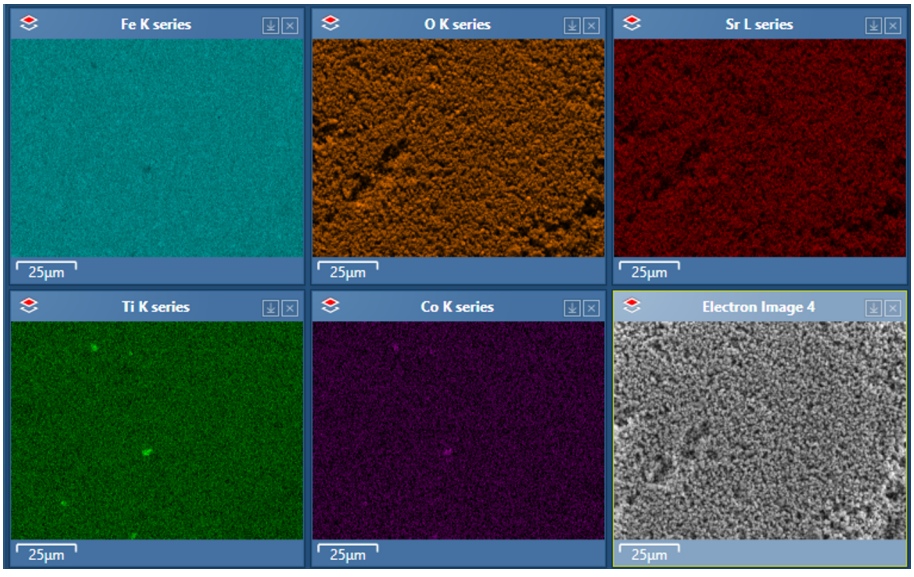

Figure C.4: Sample x = 0.7. Spotty Ti and Co suggest contamination. Shadowing effects are seen for O K and Sr L maps.

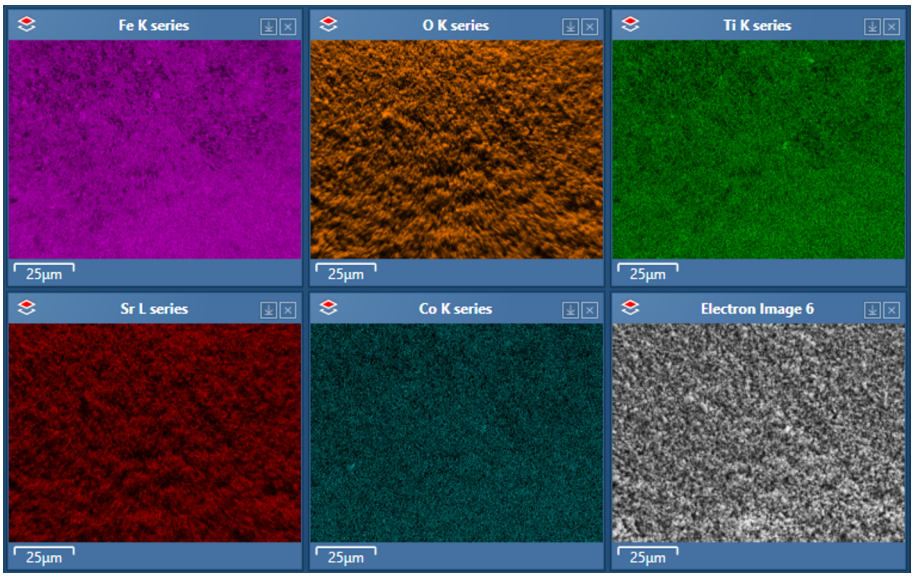

Figure C.5: Sample x = 1.1. Shadowing effects are seen for O K and Sr L maps.

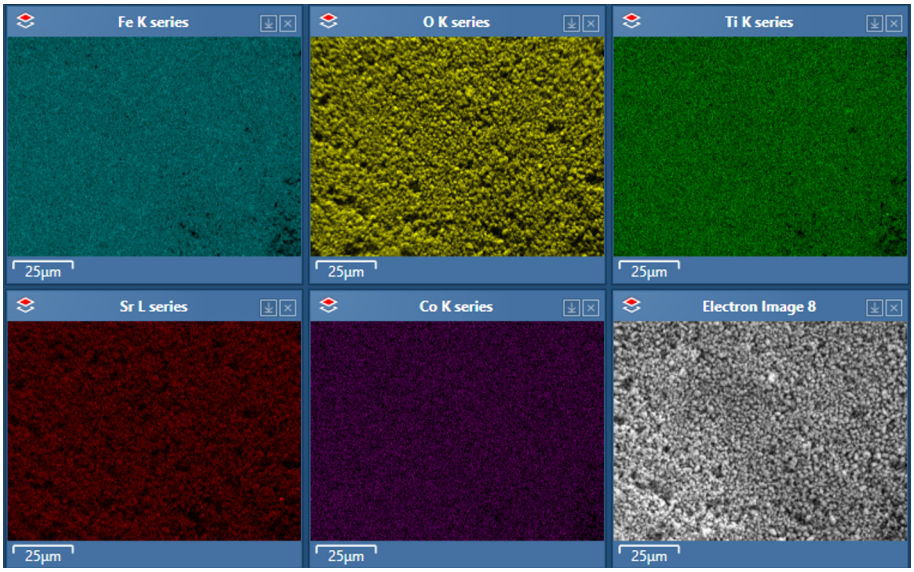

Figure C.6: Sample x = 1.5. Shadowing effects are seen for O K and Sr L maps.

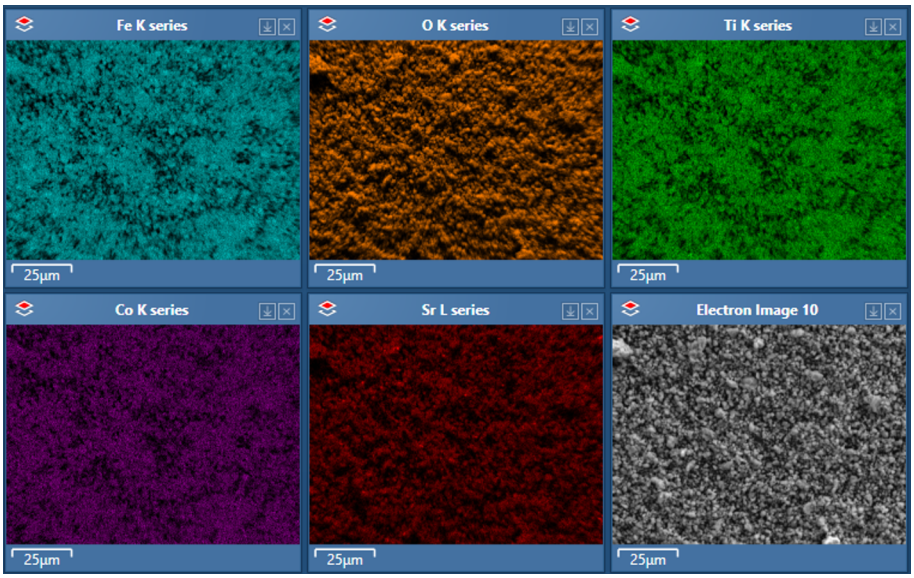

Figure C.7: Sample x = 2. Shadowing effects are seen for O K and Sr L maps.

C.3 Elemental maps (site 2)

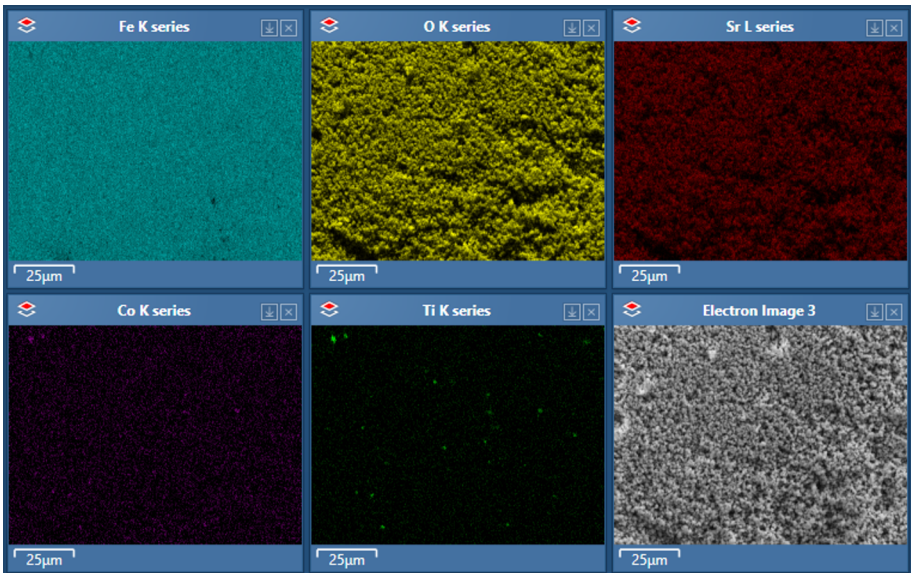

Figure C.8: Sample x = 0. Spotty Ti and Co suggest possible contamination. Shadowing effects are seen for O K and Sr L maps.

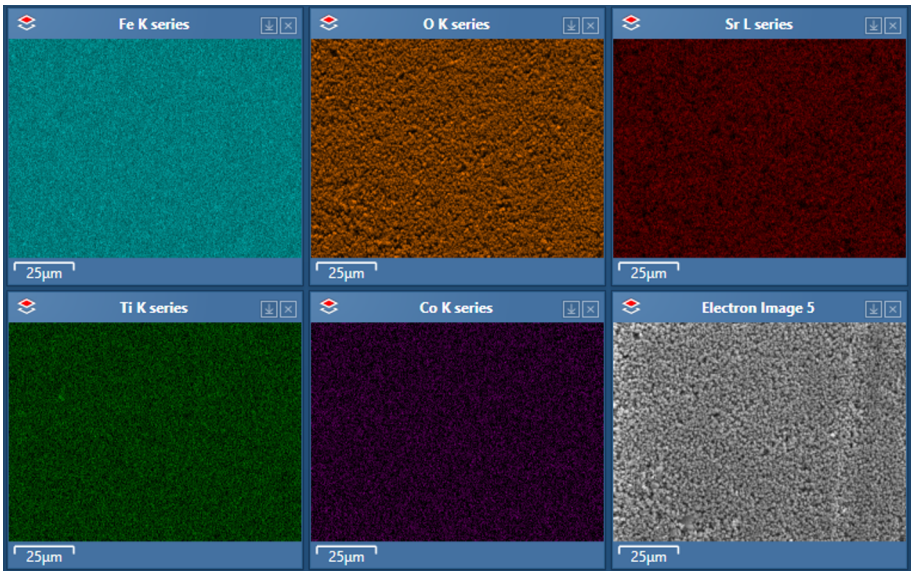

Figure C.9: Sample x = 0.7. Spotty Ti and Co suggest contamination. Shadowing effects are seen for O K and Sr L maps.

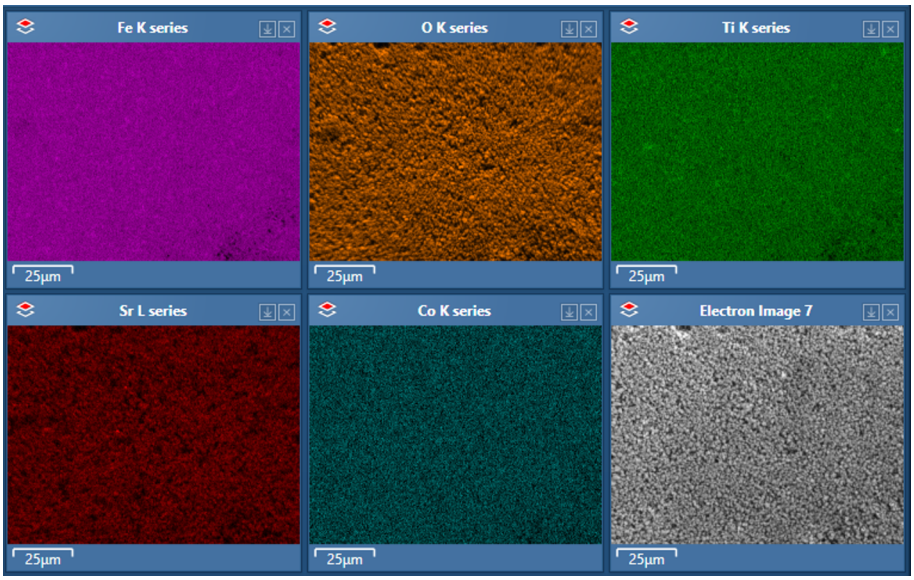

Figure C.10: Sample x = 1.1. Shadowing effects are seen for O K and Sr L maps.

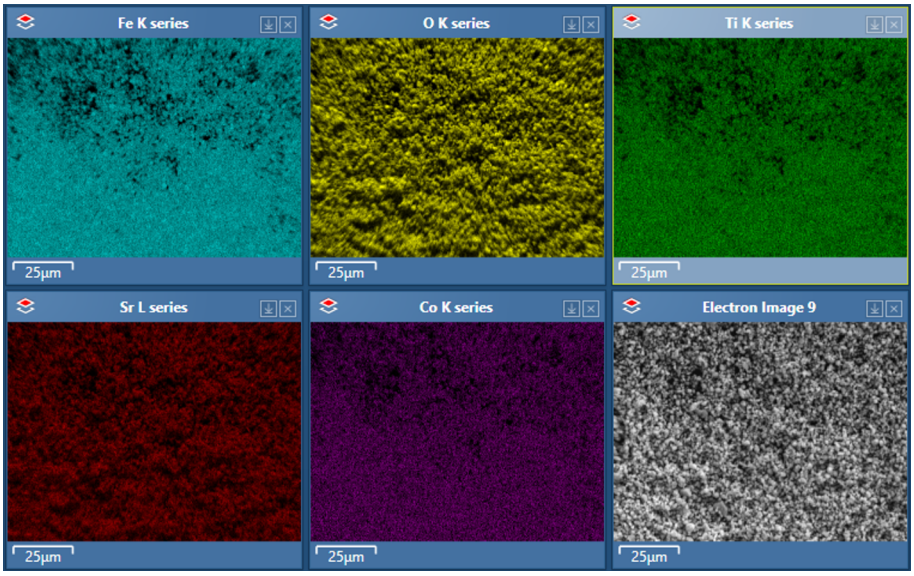

Figure C.11: Sample x = 1.5. Shadowing effects are seen for O K and Sr L maps.

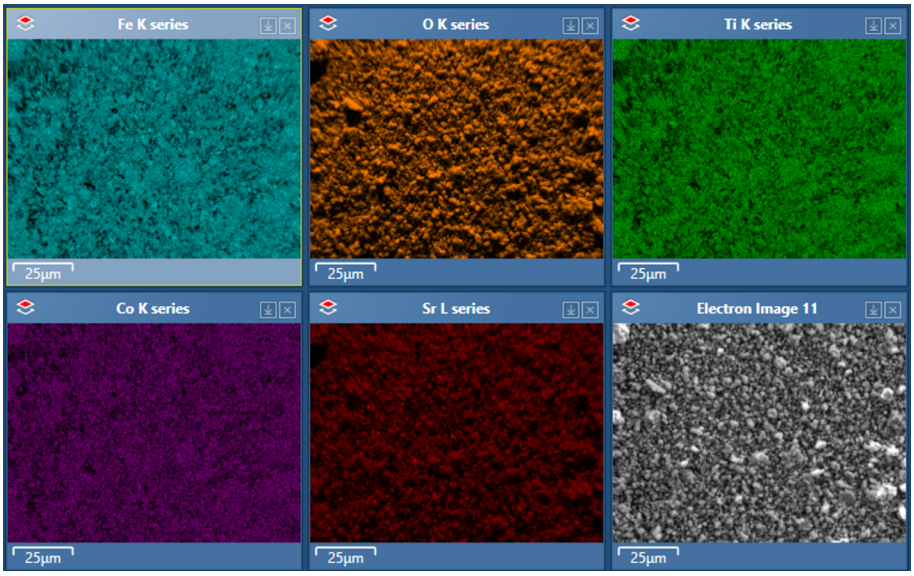

Figure C.12: Sample x = 2. Shadowing effects are seen for O K and Sr L maps.

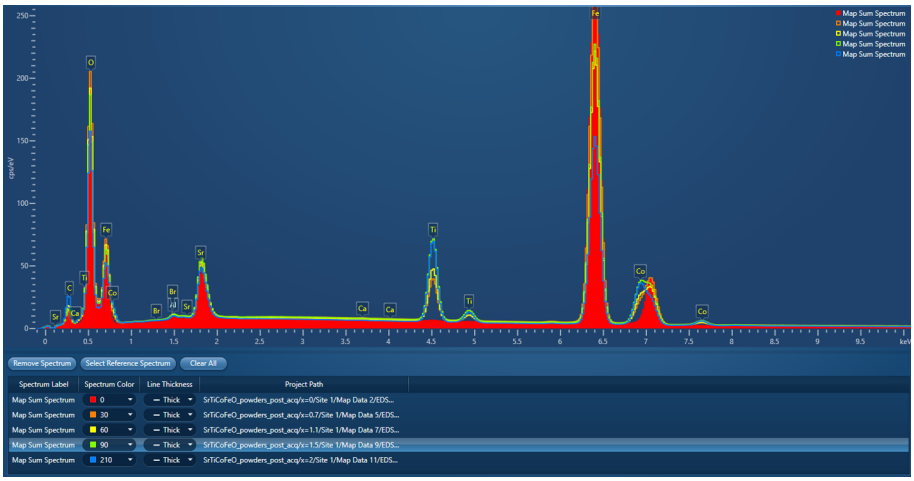

Figure C.13: Spectra taken from the Site 1 of all five powders: Spectrum colours are red (x = 0), orange (x = 0.7), yellow (x = 1.1), green (x = 1.5) and blue (x = 2.0). Energy range 0 to 10 keV.

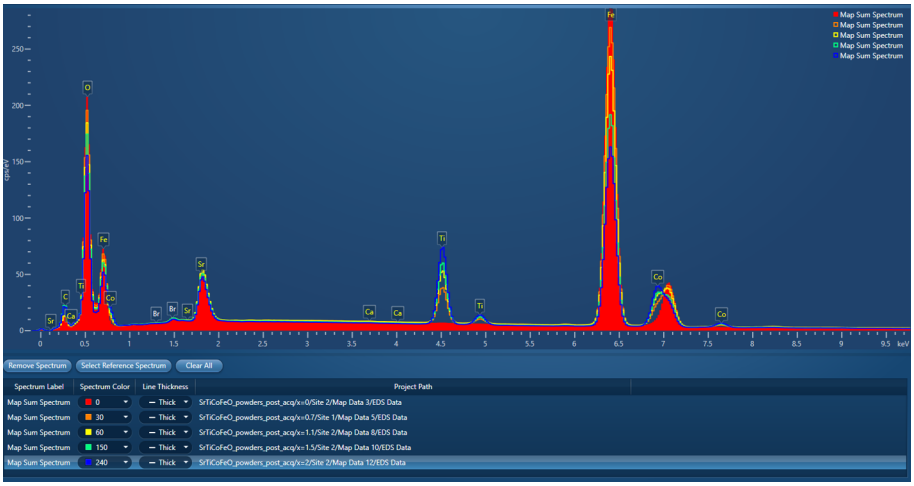

Figure C.14: Spectra taken from the Site 1 of all five powders: Spectrum colours are red (x = 0), orange (x = 0.7), yellow (x = 1.1), green (x = 1.5) and blue (x = 2.0). Energy range 0 to 10 keV.

Table C.1: The average atomic percentage of $SrCo_xTi_xFe_{12-x}O_{19}$ polycrystalline samples with x= 0, 0.7, 1.1, 1.5 and 2.

Element	x=0	x=0.7	x=1.1	x=1.5	x=2
Sr	2.7 ± 0.5	2.7 ± 0.5	2.7 ± 0.5	2.6 ± 0.5	2.6 ± 0.5
Co	0.28 ± 0.02	2.0 ± 0.5	$3. \pm 0.5$	5 ± 0.5	6 ± 0.5
Ti	0.04 ± 0.01	2.0 ± 0.5	3.8 ± 0.3	5 ± 0.3	6 ± 0.3
Fe	46 ± 1	38 ± 1	34 ± 2	30 ± 2	26 ± 1
O	49 ± 2	54 ± 2	55 ± 2	57 ± 2	58 ± 2

Table C.2: The average weight percentage of $SrCo_xTi_xFe_{12-x}O_{19}$ polycrystalline samples with x= 0, 0.7, 1.1, 1.5 and 2.

Element	x=0	x=0.7	x=1.1	x=1.5	x=2
Sr	6 ± 1	6.5 ± 0.5	7 ± 1	7 ± 1	7 ± 1
Co	0.4 ± 0.03	4.16 ± 0.08	6.46 ± 0.09	8.5 ± 0.2	11.1 ± 0.2
Ti	0.06 ± 0.02	3.63 ± 0.02	5.3 ± 0.2	7.3 ± 0.2	9.4 ± 0.2
Fe	71.3 ± 0.8	60 ± 1	55 ± 2	51 ± 1	44 ± 1
O	21 ± 1	24 ± 1	26 ± 2	27 ± 2	28 ± 1

Appendix D

Supporting materials (magnetic analysis)

The anisotropy energy for a hexagonal system, is given by:

$$E_{total} = E_a + E_{ext.field} = K_1 \sin^2\theta + K_2 \sin^4\theta + K_3 \sin^6\theta - M_s H_{app} \sin\theta \quad \text{(D.1)}$$

By minimising E_{total} with respect of the angle (θ):

$$\frac{\partial E_{total}}{\partial \theta} = 2K_1 \sin\theta\cos\theta + 4K_2 \sin^3\theta\cos\theta + 6K_3 \sin^5\theta\cos\theta - M_s H_{app}\cos\theta = 0 \quad \text{(D.2)}$$

Rearranging the equation and dividing both sides of the equation by $\cos\theta$:

$$M_s H_{app} = 2K_1 \sin\theta + 4K_2 \sin^3\theta + 6K_3 \sin^5\theta \quad \text{(D.3)}$$

Assuming the value of M_s does not change with field strength, therefore, the magnetisation component along ab-plane is given by:

$$M = M_s \sin\theta, \qquad \sin\theta = \frac{M}{M_s} \quad \text{(D.4)}$$

By substituting equation (D.4) in equation (D.3), we get:

$$M_s H_{app} = 2K_1\left(\frac{M}{M_s}\right) + 4K_2\left(\frac{M}{M_s}\right)^3 + 6K_3\left(\frac{M}{M_s}\right)^5 \quad \text{(D.5)}$$

By dividing both sides of the equation by M_s, and M, we get:

$$\frac{H_{app}}{M} = \frac{2K_1}{{M_s}^2} + \frac{4K_2}{{M_s}^4}M^2 + \frac{6K_3}{{M_s}^6}M^4 \quad \text{(D.6)}$$

List of Abbreviations

O_h Octahedral

T_d Tetrahedral

T_{rig} Trigonal bipyramidal

1D One dimension

2D Two dimensions

AFM Atomic Force Microscopy

ATLAD Alternating Target Laser Ablation Deposition

BaM Barium Ferrite

CT Crystal Field

DM Dzyaloshinskii-Moriya

EDX Energy Dispersive X-Ray

FC Field Cooled

FE Ferroelectric

FM Ferromagnetic

FMR Ferromagnetic Resonance Spectroscopy

FWHM Full Width at Half Maximum

FY Fluorescence Yield

FZ Float Zone method

LCP Left Circularly Polarized

M(T) Temperature Dependent Magnetisation

M-H Field Dependent Magnetisation

ME Magnetoeclectic

PLD Pulsed Laser Deposition

RCP Right Circularly Polarized

SEM Scanning Electron Microscope

SOC Spin Orbit Coupling

SQUID Superconducting Quantum Interference Device

SrM Strontium Ferrite

TEY Total Electron Yield

TR-MOKE Time Resolved Magneto Optical Kerr Effect

UHV Ultra High Vacuum

VSM Vibrating Sample Magnetometer

XAS X-ray Absorption Spectroscopy

XMCD X-ray Magnetic Circular Dichroism

XRD X-ray Diffraction

XRR X-ray Reflectometry

ZFC Zero Field Cooled

Bibliography

[1] Biljana D Stojanovic. *Magnetic, ferroelectric, and multiferroic metal oxides*. Elsevier, 2018.

[2] Manfred Fiebig. Revival of the magnetoelectric effect. *Journal of physics D: applied physics*, 38(8):R123, 2005.

[3] K Siratori, K Kohn, and E Kita. Magnetoelectric effect in magnetic materials. *Acta Physica Polonica A*, 81(4-5):431–466, 1992.

[4] N Ortega, Ashok Kumar, JF Scott, and Ram S Katiyar. Multifunctional magnetoelectric materials for device applications. *Journal of Physics: Condensed Matter*, 27(50):504002, 2015.

[5] Igor Kornev, Mirza Bichurin, J-P Rivera, Sandrine Gentil, Hans Schmid, AGM Jansen, and P Wyder. Magnetoelectric properties of $LiCoPO_4$ and $LiNiPO_4$. *Physical Review B*, 62(18):12247, 2000.

[6] TSUYOSHI Watanabe and K Kohn. Magnetoelectric effect and low temperature transition of $PbFe_{0.5}Nb_{0.5}O_3$ single crystal. *Phase Transitions*, 15(1):57–68, 1989.

[7] Yutaro Kitagawa, Yuji Hiraoka, Takashi Honda, Taishi Ishikura, Hiroyuki Nakamura, and Tsuyoshi Kimura. Low-field magnetoelectric effect at room temperature. *Nature materials*, 9(10):797–802, 2010.

[8] Robert C Pullar. Hexagonal ferrites: a review of the synthesis, properties and applications of hexaferrite ceramics. *Progress in Materials Science*, 57(7):1191–1334, 2012.

[9] JE Beevers, CJ Love, VK Lazarov, SA Cavill, H Izadkhah, C Vittoria, R Fan, G Van Der Laan, and SS Dhesi. Enhanced magnetoelectric effect in M−type hexaferrites by co substitution into trigonal bi-pyramidal sites. *Applied Physics Letters*, 112(8):082401, 2018.

[10] Hessam Izadkhah, Saba Zare, Sivasubramanian Somu, Fabrizio Lombardi, and Carmine Vittoria. Utilizing alternate target deposition to increase the magnetoelectric effect at room temperature in a single phase M−type hexaferrite. *MRS Communications*, 7(2):97–101, 2017.

[11] Liaoyu Wang, Dunhui Wang, Qingqi Cao, Yuanxia Zheng, Haicheng Xuan, Jinlong Gao, and Youwei Du. Electric control of magnetism at room temperature. *Scientific reports*, 2(1):1–5, 2012.

[12] Marjan Mohebbi, Khabat Ebnabbasi, and Carmine Vittoria. First observation of magnetoelectric effect in M−type hexaferrite thin films. *Journal of Applied Physics*, 113(17):17C710, 2013.

[13] Khabat Ebnabbasi. *Microwave devices utilizing magnetoelectric hexaferrite materials for emerging communication systems*. PhD thesis, Northeastern University, 2012.

[14] Y Tokunaga, Y Kaneko, D Okuyama, S Ishiwata, T Arima, S Wakimoto, K Kakurai, Y Taguchi, and Y Tokura. Multiferroic M−type hexaferrites with a room-temperature conical state and magnetically controllable spin helicity. *Physical review letters*, 105(25):257201, 2010.

[15] AM Balbashov, V Yu Ivanov, Aleksandr Alekseevich Mukhin, Lyudmila Dmitrievna Iskhakova, Yu F Popov, Gennadii Petrovich Vorobev, and ME Voronchikhina. Magnetic and magnetoelectric properties of M−type substitution hexaferrites $TSc_xFe_{12-x}O_{19}$ (T= Ba, Sr). *JETP letters*, 101(7):489–496, 2015.

[16] Robert C Pullar. Multiferroic and magnetoelectric hexagonal ferrites. In *Mesoscopic Phenomena in Multifunctional Materials*, pages 159–200. Springer, 2014.

[17] Daniel I Khomskii. Multiferroics: Different ways to combine magnetism and ferroelectricity. *Journal of Magnetism and Magnetic Materials*, 306(1):1–8, 2006.

[18] Shanta Mullick, Garima Rana, Amit Kumar, Gaurav Sharma, and Mu Naushad. "ferrites": Synthesis, structure, properties and applications. *Ferrite: Nanostructures with Tunable Properties and Diverse Applications*, 112:1–61, 2021.

[19] Sami H Mahmood and Ibrahim Abu-Aljarayesh. Hexaferrite permanent magnetic materials. Materials Research Forum LLC, 2016.

[20] Gagan Kumar Bhargava, Sumit Bhardwaj, Mahavir Singh, and Khalid Mujasam Batoo. *Ferrites and Multiferroics: Fundamentals to Applications*. Springer, 2021.

[21] Robert Carlyle Pullar. *The synthesis and characterisation of hexagonal ferrite fibres*. PhD thesis, University of Warwick, 1999.

[22] Stephen Blundell. Magnetism in condensed matter, 2003.

[23] Bernard Dennis Cullity and Chad D Graham. *Introduction to magnetic materials*. John Wiley & Sons, 2011.

[24] John MD Coey. *Magnetism and magnetic materials*. Cambridge university press, 2010.

[25] CP Bean and undJ D Livingston. Superparamagnetism. *Journal of Applied Physics*, 30(4):S120–S129, 1959.

[26] Gerald F Dionne. *Magnetic oxides*, volume 14. Springer, 2009.

[27] S.R. Stock B.D. Cullity. *Elements of X-ray Diffraction*. Pearson Education, 2014.

[28] Tsuyoshi Kimura. Magnetoelectric hexaferrites. *Annu. Rev. Condens. Matter Phys.*, 3(1):93–110, 2012.

[29] Soshin Chikazumi, Sushin Chikazumi, and Chad D Graham. *Physics of ferromagnetism*. Number 94. Oxford University Press, 1997.

[30] Nicola A Spaldin. *Magnetic materials: fundamentals and applications*. Cambridge university press, 2010.

[31] James E Beevers. *Magnetic X-ray Spectroscopy Studies of PLD grown Magnetoelectric Hexaferrites*. PhD thesis, University of York, 2018.

[32] Christopher Love. *Correlating Magnetic Damping and Microstructure in" Half Metal" Thin Films*. PhD thesis, University of York, 2018.

[33] Pankaj Thakuria, Uwe Klemradt, and Manuel Angst. Magnetic structure in relation to the magnetic field induced ferroelectricity in Y−type hexaferrite $Ba_{2-x}Sr_xZn_2Fe_{12}O_{22}$, 2017.

[34] Marjan Mohebbi. *Magnetoelectric hexaferrite thin films growth for next generation device applications*. PhD thesis, Northeastern University, 2013.

[35] Wenjie Zhang, Yang Bai, Xi Han, Liang , Xuefei Lu, and Lijie Qiao. Magnetic properties of Co−Ti substituted barium hexaferrite. *Journal of Alloys and Compounds*, 546:234–238, 2013.

[36] OP Aleshko-Ozhevskii, RA Sizov, VP Cheparin, and II Yazmin. Helicoidal antiphase spin ordering in hexagonal ferrites with magnetoplumbite structure. *ZhETF Pisma Redaktsiiu*, 7:207, 1968.

[37] Keshav Kumar, Shrawan Kumar Mishra, Sanjay Singh, Ivan Baev, Michael Martins, Fabio Orlandi, Pascal Manuel, and Dhananjai Pandey. Evidence for conical magnetic structure in M−Type $BaFe_{12}O_{19}$ hexaferrite: A combined single-crystal x-ray magnetic circular dichroism and neutron diffraction study. *physica status solidi (RRL)–Rapid Research Letters*, 15(6):2000506, 2021.

[38] Anthony R West. *Solid state chemistry and its applications*. John Wiley & Sons, 2014.

[39] Roger H Mitchell. *Perovskites: modern and ancient*, volume 7. Almaz Press Thunder Bay, 2002.

[40] Nicola Spaldin. Multiferroics-review of classification. http://www.esmf.ethz.ch/speakers/spaldin2.pdf, 2012. Accessed:2018–02-04.

[41] T Kimura. Spiral magnets as magnetoelectrics. *Annu. Rev. Mater. Res.*, 37:387–413, 2007.

[42] Yoshinori Tokura, Shinichiro Seki, and Naoto Nagaosa. Multiferroics of spin origin. *Reports on Progress in Physics*, 77(7):076501, 2014.

[43] HB Cao, ZY Zhao, M Lee, ES Choi, MA McGuire, BC Sales, HD Zhou, J-Q Yan, and DG Mandrus. High pressure floating zone growth and structural properties of ferrimagnetic quantum paraelectric $BaFe_{12}O_{19}$. *Apl Materials*, 3(6):062512, 2015.

[44] Shi-Peng Shen, Yi-Sheng Chai, Jun-Zhuang Cong, Pei-Jie Sun, Jun Lu, Li-Qin Yan, Shou-Guo Wang, and Young Sun. Magnetic-ion-induced displacive electric polarization in FeO_5 bipyramidal units of $(\mathrm{Ba},\mathrm{Sr})\,Fe_{12}O_{19}$ hexaferrites. *Physical Review B*, 90(18):180404, 2014.

[45] PS Wang and HJ Xiang. Room-temperature ferrimagnet with frustrated antiferroelectricity: promising candidate toward multiple-state memory. *Physical Review X*, 4(1):011035, 2014.

[46] WD Townes, JH Fang, and AJ Perrotta. The crystal structure and refinement of ferrimagnetic barium ferrite, $BaFe_{12}O_{19}$. *Zeitschrift für Kristallographie-Crystalline Materials*, 125(1-6):437–449, 1967.

[47] JG Rensen and JS Van Wieringen. Anisotropic mössbauer fraction and crystal structure of $BaFe_{12}O_{19}$. *Solid State Communications*, 7(16):1139–1141, 1969.

[48] Guolong Tan and Xiuna Chen. Synthesis, structures, and multiferroic properties of strontium hexaferrite ceramics. *Journal of electronic materials*, 42(5):906–911, 2013.

[49] Guolong Tan, Yao Huang, and Haohao Sheng. Magnetoelectric response in multiferroic $SrFe_{12}O_{19}$ ceramics. *PloS one*, 11(12), 2016.

[50] Donna Arnold. Ps701 topics in functional materials. 2016.

[51] Gopalan Srinivasan. Magnetoelectric composites. *Annual Review of Materials Research*, 40:153–178, 2010.

[52] J-P Rivera. On definitions, units, measurements, tensor forms of the linear magnetoelectric effect and on a new dynamic method applied to Cr−Cl boracite. *Ferroelectrics*, 161(1):165–180, 1994.

[53] AM Balbashov, ME Voronchikhina, LD Iskhakova, V Yu Ivanov, and AA Mukhin. Single crystals growth of hexaferrits M−type $MTi_xCo_xFe_{12-2x}O_{19}$ (M= Ba, Sr) by floating zone and investigation of their magnetic and magnetoelectric properties. *Low Temperature Physics*, 43(8):971–976, 2017.

[54] VG Kostishyn, LV Panina, LV Kozhitov, AV Timofeev, and AN Kovalev. Synthesis and multiferroic properties of M−type $SrFe_{12}O_{19}$ hexaferrite ceramics. *Journal of Alloys and Compounds*, 645:297–300, 2015.

[55] N Langhof and M Göbbels. Hexaferrites and phase relations in the iron-rich part of the system Sr−La−Co−Fe−O. *Journal of Solid State Chemistry*, 182(10):2725–2732, 2009.

[56] SM Koohpayeh, David Fort, and JS Abell. The optical floating zone technique: A review of experimental procedures with special reference to oxides. *Progress in Crystal Growth and Characterization of Materials*, 54(3-4):121–137, 2008.

[57] Hans-Ulrich Krebs, Martin Weisheit, Jörg Faupel, Erik Süske, Thorsten Scharf, Christian Fuhse, Michael Störmer, Kai Sturm, Michael Seibt, Harald Kijewski, et al. Pulsed laser deposition (PLD)-a versatile thin film technique. In *Advances in Solid State Physics*, pages 505–518. Springer, 2003.

[58] Mahesh Kishanrao Babrekar. Synthesis characterization and properties of ferrite thin film.

[59] PR Willmott and JR Huber. Pulsed laser vaporization and deposition. *Reviews of Modern Physics*, 72(1):315, 2000.

[60] Jens Als-Nielsen and Des McMorrow. *Elements of modern X-ray physics*. John Wiley & Sons, 2011.

[61] Charles Kittel. Introduction to solid state physics eighth edition. 2004.

[62] Lecture (1) symmetry in the solid state, part i: Simple patterns and groups. https://www2.physics.ox.ac.uk/sites/default/files/CrystalStructure-Handout1-1.pdf.

[63] M Grant Norton and C Suryanarayana. *X-Ray diffraction: a practical approach*. Plenum Press, 1998.

[64] R.B. Roof. A computer program to aid in the indexing of x- ray powder patterns of crystal structures of unknown symmetry, 1968.

[65] IV In. X-ray thin film measurement techniques.

[66] Rigaku Corporation. X-ray diffraction software smartlab studio ii. *Rigaku J.*

[67] Chair of Experimental Semiconductor Physics. High resolution x-ray diffraction, 2020.

[68] Katsuhiko Inaba and Shintaro Kobayashi. Various pole figure measurement techniques with smartlab, assisting thin film characterization. *The Rigaku Journal*, 34(2):10–16, 2018.

[69] SP Thompson, JE Parker, J Potter, TP Hill, A Birt, TM Cobb, F Yuan, and CC Tang. Beamline-i11 at diamond: A new instrument for high resolution powder diffraction. *Review of scientific instruments*, 80(7):075107, 2009.

[70] Cl Murray, SP Thompson, JE Parker, J Potter, F Yuan, and CC Tang. Beamline-i11user manual. *Review of scientific instruments*, page 61, 2017.

[71] Robert E Dinnebier and Simon JL Billinge. *Powder diffraction: theory and practice*. Royal society of chemistry, 2008.

[72] Tomče Runčevski. Rietveld refinement practical powder diffraction pattern analysis using TOPAS. by robert e. dinnebier, andreas leineweber and john so evans. de gruyter, 2019. pp. 331. price (paperback) eur 69.95, usd 80.99, gbp 63.50. isbn 978-3-11-045621-9, e-isbn (pdf) 978-3-11-046138-1. *Journal of Applied Crystallography*, 52(5):1238–1239, 2019.

[73] Vitalij Pecharsky and Peter Zavalij. *Fundamentals of powder diffraction and structural characterization of materials*. Springer Science & Business Media, 2008.

[74] Advanced certificate in powder diffraction on the web course material master index. http://pd.chem.ucl.ac.uk/pdnn/peaks/others.htm, note= Accessed:2018–02-04, 2012.

[75] University of Oklahoma Department of Chemistry Biochemistry, Chemical Crystallography Laboratory. Steps in structure refinement. http://xrayweb.chem.ou.edu/notes/refine.htmlrefine, 2020.

[76] LB McCusker, RB Von Dreele, DE Cox, D Louër, and P Scardi. Rietveld refinement guidelines. *Journal of Applied Crystallography*, 32(1):36–50, 1999.

[77] Brian H Toby and Robert B Von Dreele. GSAS–II: the genesis of a modern open-source all purpose crystallography software package. *Journal of Applied Crystallography*, 46(2):544–549, 2013.

[78] BH Toby. Multiphase and multiple data set fitting. 2019.

[79] Grant Wiggins. How good is good enough. *Educational Leadership*, 71(4):10–16, 2014.

[80] Irene Azaceta. *Correlating magnetic and structural properties of full Heusler Co_2FeSi films*. PhD thesis, University of York, 2021.

[81] Anwar Ul-Hamid. *A beginners' guide to scanning electron microscopy*, volume 1. Springer, 2018.

[82] Leonard Frederic Henrichs. *Magnetoelectric Coupling in Single-Phase Multiferroics at Room Temperature via Scanning Probe Microscopy*. PhD thesis, University of Leeds, 2015.

[83] CA Quantum Design San Diego. Magnetic property measurement system. https://mmrc.caltech.edu/MPMS/Manuals/QD/20HWD/20Ref.pdf, 1996.

[84] David Jiles. *Introduction to magnetism and magnetic materials*. CRC press, 2015.

[85] Xavier Batlle, M Garcia del Muro, Javier Tejada, H Pfeiffer, Peter Görnert, and Ekkehard Sinn. Magnetic study of M–type doped barium ferrite nanocrystalline powders. *Journal of applied physics*, 74(5):3333–3340, 1993.

[86] X Batlle, X Obradors, J Rodriguez-Carvajal, M Pernet, MV Cabanas, and M Vallet. Cation distribution and intrinsic magnetic properties of Co–Ti–doped M–type barium ferrite. *Journal of applied physics*, 70(3):1614–1623, 1991.

[87] Alex Hubert and Rudolf Schäfer. *Magnetic domains: the analysis of magnetic microstructures*. Springer Science & Business Media, 2008.

[88] Frank De Groot and Akio Kotani. *Core level spectroscopy of solids*. CRC press, 2008.

[89] X-ray Data Booklet. Centre for x-ray optics and advanced light source. *Berkley: Lawrence Berkeley National Laboratory*, 2001.

[90] Surface science and Anders Nilsson x-ray spectroscopy group. Spectroscopic techniques. https://www-ssrl.slac.stanford.edu/nilssongroup/pages/core-spec-xps.html.

[91] Gerrit van der Laan and Adriana I Figueroa. X-ray magnetic circular dichroism a versatile tool to study magnetism, 2014.

[92] Andreas Scherz. *Spin dependent x-ray absorption spectroscopy of 3d transition metals: systematics and applications*. dissertation.de, 2004.

[93] Diamond Light Source. https://www.diamond.ac.uk/Home.

[94] Gerrit van der Laan and Adriana I Figueroa. X-ray magnetic circular dichroism—a versatile tool to study magnetism. *Coordination Chemistry Reviews*, 277:95–129, 2014.

[95] Eli Stavitski and Frank MF De Groot. The CTM_4XAS program for EELS and XAS spectral shape analysis of transition metal L edges. *Micron*, 41(7):687–694, 2010.

[96] FMF De Groot. CTM_4XAS charge transfer multiplet course manual: The simulation of the transition metal 2p and 3p XAS, XPS, and XMCD spectra, 2008.

[97] Piter Sybren Miedema. *X-ray spectroscopy of inorganic materials*. Utrecht University, 2012.

[98] Dr. H. Putz Dr. K. Brandenburg GbR. MatchMatch - phase analysis using powder diffraction, version 3.x, crystal impact.

[99] Shereen Selvaraj, Uma Gandhi, L John Berchmans, and Umapathy Mangalanathan. Effect of magnetic ion substitution on the structure and temperature-dependent magnetic properties of strontium hexaferrite. *Materials Technology*, 36(1):36–45, 2021.

[100] K Kimura, M Ohgaki, K Tanaka, H Morikawa, and F Marumo. Study of the bipyramidal site in magnetoplumbite-like compounds, $SrM_{12}O_{19}$ (M= Al, Fe, Ga). *Journal of Solid State Chemistry*, 87(1):186–194, 1990.

[101] K Krezhov, Z Somogyvári, Gy Mészáros, E Sváb, I Nedkov, and F Bourée. Neutron powder diffraction study of (Co, Ti)-substituted fine-particle ba-hexaferrite. *Applied Physics A*, 74(1):s1086–s1088, 2002.

[102] Chan-Uk Kim and Nam-Ung Jo. Microwave dielectric properties of $BaCo_xTi_xFe_{12-x}O_{19}$, 1<x<5 materials. *Korean Journal of Materials Research*, 8(8):775–779, 1998.

[103] RL Blake. Hessevic., re; zoltai, t.; finger, lw. *Am. Mineral*, 51:123, 1966.

[104] K-B Kim, Y-H Lee, Huh YH, and Y-I Kim. Structural refinement of highly textured hexagonal ferrite using x-ray powder diffraction data. *Journal of the Japan Society of Powder and Powder Metallurgy*, 61(S1):S85–S89, 2014.

[105] C Gökhan Ünlü, M Burak Kaynar, Telem Şimşek, Atakan Tekgül, Bora Kalkan, and Şadan Özcan. Structure and magnetic properties of $La_{1-x}Fe_xO_3$ (x= 0, 0.25, 0.50) perovskite. *Journal of Alloys and Compounds*, 784:1198–1204, 2019.

[106] Min Zhang, Qiangchun Liu, Guangping Zhu, and Shitao Xu. Magnetic properties of Co and Ti co-doped strontium hexaferrite prepared by sol–gel method. *Applied Physics A*, 125(3):1–6, 2019.

[107] SV Trukhanov, AnV Trukhanov, VA Turchenko, An V Trukhanov, DI Tishkevich, EL Trukhanova, TI Zubar, DV Karpinsky, VG Kostishyn, LV Panina, et al. Magnetic and dipole moments in indium doped barium hexaferrites. *Journal of Magnetism and Magnetic Materials*, 457:83–96, 2018.

[108] Sami H Mahmood, Ahmad M Awadallah, Ibrahim Bsoul, and Yazan Maswadeh. Structural and magnetic properties of lightly doped M−type hexaferrites. *arXiv preprint arXiv:1707.04709*, 2017.

[109] D Seifert, J Töpfer, F Langenhorst, J-M Le Breton, H Chiron, and L Lechevallier. Synthesis and magnetic properties of La−substituted M−type Sr hexaferrites. *Journal of Magnetism and Magnetic Materials*, 321(24):4045–4051, 2009.

[110] Sami Mahmood, Ibrahim Bsoul, et al. Tuning the magnetic properties of M−type hexaferrites. *arXiv preprint arXiv:1707.07243*, 2017.

[111] Gang Qiang, Yuan Jin, Xiaowen Lu, Xiaopeng Cui, Dongmei Deng, Baojuan Kang, Wuguo Yang, Shixun Cao, and Jincang Zhang. Temperature effect on the magnetic property and ferroelectricity in hexaferrite $SrFe_{12}O_{19}$. *Applied Physics A*, 122(7):1–6, 2016.

[112] Andrew P Roberts, Yulong Cui, and Kenneth L Verosub. Wasp-waisted hysteresis loops: Mineral magnetic characteristics and discrimination of components in mixed magnetic systems. *Journal of Geophysical Research: Solid Earth*, 100(B9):17909–17924, 1995.

[113] PG Bercoff and HR Bertorello. Magnetic properties of hematite with large coercivity. *Applied Physics A*, 100(4):1019–1027, 2010.

[114] Marin Tadić, Nada Čitaković, Matjaž Panjan, Zoran Stojanović, Dragana Marković, and Vojislav Spasojević. Synthesis, morphology, microstructure and magnetic properties of hematite submicron particles. *Journal of alloys and compounds*, 509(28):7639–7644, 2011.

[115] MV Cabanas, JM Gonzlez-Calbet, J Rodrıguez-Carvajal, and M Vallet-Regi. The solid solution $BaFe_{12-2x}Co_xTi_xO_{19}$ (0 x 6): cationic distribution by neutron diffraction. *Journal of Solid State Chemistry*, 111(2):229–237, 1994.

[116] JJ Went, GW Rathenau, EW Gorter, and GW Van Oosterhout. Hexagonal iron-oxide compounds as permanent-magnet materials. *Physical Review*, 86(3):424, 1952.

[117] GA Alna'washi, AM Alsmadi, I Bsoul, Gassem M Alzoubi, B Salameh, M Shatnawi, FM Al-Dweri, and SH Mahmood. Magnetic study of M−type Co−Ti doped strontium hexaferrite nanocrystalline particles. *Journal of Superconductivity and Novel Magnetism*, 33(5):1423–1432, 2020.

[118] Joachim Stöhr and Hans Christoph Siegmann. Magnetism. *Solid-State Sciences. Springer, Berlin, Heidelberg*, 5:236, 2006.

[119] Joseph Gompertz. *Magnetic Interface Structures in Exchange Bias Systems*. PhD thesis, University of York, 2019.

[120] AM Alsmadi, I Bsoul, SH Mahmood, G Alnawashi, K Prokeš, K Siemensmeyer, B Klemke, and H Nakotte. Magnetic study of M−type doped barium hexaferrite nanocrystalline particles. *Journal of Applied Physics*, 114(24):243910, 2013.

[121] P Gaunt. Domain wall pinning at random inhomogeneities. *IEEE Transactions on Magnetics*, 19(5):2030–2032, 1983.

[122] H Morishita, A Amano, H Ueda, C Michioka, and K Yoshimura. Single crystal growth of strontium ferrite with magnetoplumbite structure using the traveling solvent floating zone method. *Journal of the Japan Society of Powder and Powder Metallurgy*, 61(S1):S64–S66, 2014.

[123] GNU General Public Schumann, O. J. Cologne Laue Indexation Program v4.0 RC1. Interactive program for evaluation of laue diffraction patterns. http://clip4.sourceforge.net, 2008.

[124] A Shimoda, K Takao, K Uji, T Waki, Y Tabata, and H Nakamura. Flux growth of magnetoplumbite M-type strontium ferrite single crystals with La−Co substitution. *Journal of Solid State Chemistry*, 239:153–158, 2016.

[125] Kurt Heinz Jürgen Buschow, Frank R Boer, et al. *Physics of magnetism and magnetic materials*, volume 7. Springer, 2003.

[126] Ajit Kumar Patra. *Crystal Structure, anisotropy and spin reorientation transition of highly coercive, epitaxialPr−Cofilms*. Cuvillier Verlag, 2008.

[127] Kun Zhai, Yan Wu, Shipeng Shen, Wei Tian, Huibo Cao, Yisheng Chai, Bryan C Chakoumakos, Dashan Shang, Liqin Yan, Fangwei Wang, et al. Giant magnetoelectric effects achieved by tuning spin cone symmetry in Y−type hexaferrites. *Nature communications*, 8(1):1–8, 2017.

[128] JM Lommel. Hard magnetic materials. *J. Appl. Phys.*, 40(3):1294–1296, 1969.

[129] Willie Sucksmith and Jo E Thompson. The magnetic anisotropy of cobalt. *Proceedings of the Royal Society of London. Series A. Mathematical and Physical Sciences*, 225(1162):362–375, 1954.

[130] Felip Sandiumenge, Benjamín Martínez, Xavier Batlle, Salvador Galí, and Xavier Obradors. Cation distribution and magnetization of $BaSn_xCo_xFe_{12-2x})O_{19}$ (x= 0.9, 1.28) single crystals. *Journal of applied physics*, 72(10):4608–4614, 1992.

[131] BT Shirk and WR Buessem. Temperature dependence of M_s and K_1 of $BaFe_{12}O_{19}$ and $SrFe_{12}O_{19}$ single crystals. *Journal of Applied Physics*, 40(3):1294–1296, 1969.

[132] J Kreisel, H Vincent, F Tasset, M Pate, and JP Ganne. An investigation of the magnetic anisotropy change in $BaCo_2Ti_2Fe_8O_{19}$ single crystals. *Journal of Magnetism and Magnetic Materials*, 224(1):17–29, 2001.

[133] Marek W Gutowski. Where is magnetic anisotropy field pointing to? *arXiv preprint arXiv:1312.7130*, 2013.

[134] Min Feng, Bin Shao, Jian Wu, and Xu Zuo. Ab initio study on magnetic anisotropy change of $SrCo_xTi_xFe_{12-2x}O_{19}$. *Journal of Applied Physics*, 113(17):17D909, 2013.

[135] FK Lotgering. Influence of Co (II) ions on the magnetic anisotropy of ferrimagnetic oxides having hexagonal crystal structures. *Philips Res. Rep.*, 16:441–454, 1961.

[136] SN Zinenko, AA Murakhovski, LP Ol'khovik, ZI Sizova, EV Shurinova, and AS Kamzin. Theoretical prediction of a surface-induced spin-reorientation phase transition in $BaFe_{12}O_{19}$ nanocrystals. *Journal of Experimental and Theoretical Physics*, 96(5):945–952, 2003.

[137] G Bottoni. Magnetic anisotropy of Baferrite particles at low temperature. *Le Journal de Physique IV*, 7(C1):C1–739, 1997.

[138] John Michael David Coey. *Rare-earth iron permanent magnets*. Number 54. Oxford University Press, 1996.

[139] D Samaras, A Collomb, S Hadjivasiliou, C Achilleos, J Tsoukalas, J Pannetier, and J Rodriguez. The rotation of the magnetization in the $BaCo_2Fe_{16}O_{27}$ W-type hexagonal ferrite. *Journal of magnetism and magnetic materials*, 79(2):193–201, 1989.

[140] M Zentkova, M Mihalik, M Mihalik Jr, V Sirenko, VV Eremenko, AM Balbashov, L Kvetkova, V Koval, A Vỳrostková, J Briančin, et al. Preparation and physical properties of M−type hexaferrite $SrCo_2Ti_2Fe_8O_{19}$. *Ferroelectrics*, 499(1):1–8, 2016.

[141] Weihu Zhang, Qishan Zhu, Rujun Tang, Hao Zhou, Jianmin Zhang, Jiaxing Jiang, Hao Yang, and Xiaodong Su. Temperature dependent magnetic properties of conical magnetic structure M−type hexaferrites $BaSc_{1.8}Fe_{10.2}O_{19}$ and $SrSc_{1.8}Fe_{10.2}O_{19}$. *Journal of Alloys and Compounds*, 750:368–374, 2018.

[142] CA Carosella, DB Chrisey, P Lubitz, JS Horwitz, P Dorsey, R Seed, and C Vittoria. Pulsed laser deposition of epitaxial $BaFe_{12}O_{19}$ thin films. *Journal of applied physics*, 71(10):5107–5110, 1992.

[143] PC Dorsey, DB Chrisey, JS Horwitz, P Lubitz, and RCY Auyeung. Oriented barium hexaferrite thick films grown on c-plane and m-plane sapphire substrates. *IEEE Transactions on magnetics*, 30(6):4512–4517, 1994.

[144] P Borisov, J Alaria, T Yang, SRC McMitchell, and MJ Rosseinsky. Growth of M−type hexaferrite thin films with conical magnetic structure. *Applied Physics Letters*, 102(3):032902, 2013.

[145] Miho Yasaka et al. X-ray thin-film measurement techniques. *The Rigaku Journal*, 26(2):1–9, 2010.

[146] Woo-Suk Noh, Kyung-Tae Ko, Sae Hwan Chun, Kee Hoon Kim, Byeong-Gyu Park, Jae-Young Kim, and Jae-Hoon Park. Magnetic origin of giant magnetoelectricity in doped Y-type hexaferrite $Ba_{0.5}Sr_{1.5}Zn_2Al_x(Fe_{1-x})12O_{22}$. *Physical Review Letters*, 114(11):117603, 2015.

[147] G Delgado Soria, P Jenus, JF Marco, A Mandziak, M Sanchez-Arenillas, F Moutinho, JE Prieto, P Prieto, J Cerdá, C Tejera-Centeno, et al. Strontium hexaferrite platelets: a comprehensive soft x-ray absorption and mössbauer spectroscopy study. *Scientific reports*, 9(1):1–13, 2019.

[148] Victoria S Coker, Neil D Telling, Gerrit Van Der Laan, Richard AD Pattrick, Carolyn I Pearce, Elke Arenholz, Floriana Tuna, Richard EP Winpenny, and Jonathan R Lloyd. Harnessing the extracellular bacterial production of nanoscale cobalt ferrite with exploitable magnetic properties. *Acs Nano*, 3(7):1922–1928, 2009.

[149] Martin Welke, Joachim Gräfe, Remya Kunjuveettil Govind, Vasili Hari Babu, Martin Trautmann, Karl-Michael Schindler, and Reinhard Denecke. XMCD studies of thin Co films on $BaTiO_3$. *Journal of Physics: Condensed Matter*, 27(32):326001, 2015.

[150] Siobhan Grayson. Theoretical simulation of resonant inelastic x-ray scattering in transition metal oxides. *Project Report*, 2012.

[151] Ernst Meyer, Hans Josef Hug, Roland Bennewitz, et al. *Scanning probe microscopy*, volume 4. Springer, 2003.

[152] XZ Zhou, AH Morrish, ZW Li, and YK Hong. Site preference for Co^{2+} and Ti^{4+} in Co−Ti substituted barium ferrite. *IEEE transactions on magnetics*, 27(6):4654–4656, 1991.